รายงานวิจัยฉบับสมบูรณ์

โครงการ การเพิ่มประสิทธิภาพการกำจัดสารหนูที่ปนเปื้อนในน้ำใต้ดินโดยใช้ K-OMS2 และ MOFs บนวัสดุรองรับ ศึกษาการทดลองแบบแบทช์และแบบคอลัมน์

(Enhancement of removal efficiency of arsenic contaminated in groundwater using manganese oxide coupled with metal organic frameworks coating on support materials: batch and column studies)

โดย ผศ. ดร. วิษณุ แทนบุญช่วย และคณะ

สาขาวิศวกรรมสิ่งแวดล้อม คณะวิศวกรรมศาสตร์

มหาวิทยาลัยขอนแก่น

30 เมษายน 2563

สัญญาเลขที่ MRG6180196

รายงานวิจัยฉบับสมบูรณ์

โครงการ การเพิ่มประสิทธิภาพการกำจัดสารหนูที่ปนเปื้อนในน้ำใต้ดินโดยใช้ K-OMS2 และ MOFs บนวัสดุรองรับ ศึกษาการทดลองแบบแบทช์และแบบคอลัมน์

(Enhancement of removal efficiency of arsenic contaminated in groundwater using manganese oxide coupled with metal organic frameworks coating on support materials: batch and column studies)

คณะผู้วิจัย

1. ผศ. ดร. วิษณุ แทนบุญช่วย สังกัด คณะวิศวกรรมศาสตร์ มหาวิทยาลัยขอนแก่น
2. รศ. ดร. นุรักษ์ กฤษดานุรักษ์ สังกัด คณะวิศวกรรมศาสตร์ มหาวิทยาลัยธรรมศาสตร์

สนับสนุนโดยสำนักงานคณะกรรมการอุดมศึกษา และสำนักงานกองทุนสนับสนุนการวิจัย

(ความเห็นในรายงานนี้เป็นของผู้วิจัย สกอ. และ สกว. ไม่จำเป็นต้องเห็นด้วยเสมอไป)

Abstract

This study aimed to remove arsenite As(III) via co-processes of oxidation and adsorption in a continuous flow system using fixed-bed columns. Manganese oxide octahedral molecular sieve (K-OMS2) and iron-based metal-organic framework (Fe-BTC) were applied as an oxidizer and an adsorbent, respectively. Before use in the column, K-OMS2 and Fe-BTC powders were coated on the ceramic ball through the mechanical orbital shaking technique with each of K-OMS2 and Fe-BTC to ceramic ball ratios of 1 to 50. Then, they were characterized by X-ray diffraction (XRD) and X-ray absorption near-edge structure (XANES) techniques. Finally, the As(III) and arsenate As(V) removal efficiency in every single fixed-bed column of K-OMS2 (coated) and Fe-BTC (coated), respectively, and the two columns combined were conducted. From the results, in the single-column test, K-OMS2 (coated) maintained good efficiency to oxidize As(III) for a 3-round reuse cycle with lower than groundwater standard of Mn and K leaching. In the Fe-BTC (coated) column test, adsorption kinetics fit well with the Yoon-Nelson model having the highest q_0 of 52.60 mg/g and Fe leaching of 0.23 mg/L. With two columns combined, the system enabled to remove total As for 60% within 2,200 min. In part of Cerium Oxide (CeO_2) application, batch experiments indicated that the arsenic removal process was accurately described by a pseudo-second-order kinetic model with maximum removal capacities of 21.27 mg/g. As results of effect of ions species, Phosphate (PO_4^{3-}), Bicarbonate (HCO_3^-), Sulfate (SO_4^{2-}) and Selenium (Se) play the role of inhibiting arsenic removal. Hence, it was suggested that the arsenic removal by the nanoiron process can be improved through pretreatment of these ions, especially Se. In this study proposed the technic for Se removal by NZVI supported by zeolite (Z-NZVI). The results showed that Se could be effectively removed by Z-NZVI.

Keywords: adsorption; arsenic; arsenite; fixed-bed column; oxidation

บทคัดย่อ

งานที่วิจัยนี้มีวัตถุประสงค์เพื่อสร้างระบบกำจัดสารหนู โดยผ่านกระบวนการร่วมกันระหว่างกระบวนการออกซิเดชัน (Oxidation) และกระบวนการดูดซับ (Adsorption) ในระบบการไหลแบบต่อเนื่อง วัสดุ Manganese oxide octahedral molecular sieve (K-OMS2) และ Iron-based metal-organic framework (Fe-BTC) ถูกนำมาเป็นตัวออกซิไดซ์และตัวดูดซับตามลำดับ โดยวัสดุทั้งสองจะถูกเคลือบบนเม็ดเซรามิกด้วยกระบวนการเชิงกล จากนั้นนำวัสดุที่เคลือบแล้วไปทำการวิเคราะห์คุณลักษณะด้วยเทคนิค X-ray diffraction (XRD) และ X-ray absorption near-edge structure (XANES) สารหนูในรูปของ As(III) และ As(V) จะถูกทดสอบการกำจัดโดยไหลผ่านคอลัมน์ที่บรรจุ K-OMS2 และ Fe-BTC โดยผลการทดสอบพบว่าคอลัมน์ K-OMS2 สามารถออกซิไดซ์ As(III) ไปเป็น As(V) ได้อย่างมีประสิทธิภาพ และตัววัสดุ K-OMS2 ยังสามารถใช้ซ้ำได้อีก 3 ครั้ง ในขณะที่คอลัมน์ที่บรรจุ Fe-BTC สามารถดูดซับ As(V) ได้ โดยมีจลนพลศาสตร์การดูดซับเป็นไปตามแบบจำลองของ Yoon-Nelson ที่มีความสามารถในการดูดซับเท่ากับ 52.60 มิลลิกรัมของสารหนูต่อกรัมของ Fe-BTC และระบบมีสาร Fe ละลายหลุดออกมาเพียงเล็กน้อย (0.23 มิลลิกรัมต่อลิตร) และเมื่อนำคอลัมน์ที่บรรจุ K-OMS2 และ Fe-BTC มาต่อร่วมกัน พบว่ามีความสามารถในการกำจัดสารหนูได้ 60% ในเวลา 2,200 นาที สำหรับในส่วนของการทดสอบใช้ ซีเลียมออกไซด์ (CeO_2) ในการกำจัดสารหนู เพื่อเปรียบเทียบกับระบบแรก พบว่า CeO_2 สามารถกำจัดสารหนูได้ โดยมีพฤติกรรมเป็นไปตามปฏิกิริยาทางจลนพลศาสตร์อันดับ 2 เทียม (Psudo 2^{nd} order) โดยมีความสามารถในการกำจัดเท่ากับ 21.27 มิลลิกรัมของสารหนูต่อกรัมของ CeO_2 และในส่วนการทดสอบอิทธิพลของไอออนพบว่า ถ้าน้ำมีสาร PO_4^{3-}, HCO_3^-, SO_4^{2-} และ Se ปนเปื้อน จะส่งผลให้ประสิทธิภาพการกำจัดสารหนูลดลง ดังนั้นงานวิจัยนี้จึงเสนอว่าหากต้องการเพิ่มประสิทธิภาพการกำจัดสารหนูจะต้องมีระบบเพื่อทำการกำจัดสารเหล่านี้ออกไปก่อนโดยเฉพาะสาร PO_4^{3-} และ Se และงานวิจัยนี้ได้เสนอวิธีการกำจัดสาร Se โดยวัสดุ NZVI บนตัวรองรับซีโอไลต์ ซึ่งพบว่า Se สามารถถูกำจัดได้ดีโดยใช้วัสดุ NZVI บนตัวรองรับซีโอไลต์.

คำสำคัญ: adsorption; arsenic; arsenite; fixed-bed column; oxidation

Executive Summary

Introduction: The contamination of arsenic in groundwater is a worldwide problem. Long-term consumption of high arsenic-contaminated water may lead to cancer of the skin, lungs, liver, and black foot disease. Arsenite (As(III)) and arsenate (As(V)) are the two major arsenic species in aqueous systems. To achieve greater arsenic removal, As(III) pre-oxidation followed by co-precipitation/adsorption of the As(V) is usually employed. This two-step process complicated operation, high cost, and low arsenic removal efficiency.

Objective: A novel process for arsenic removal, which combined the advantages of K-OMS2 and Fe-BTC for simultaneously oxidation and adsorption, was developed. Also, another material, Cerium(VI) oxide (CeO_2), was tested to removal arsenic contamination and compared with K-OMS2 and Fe-BTC. In addition, the influence of several common ions such as phosphate (PO_4^{3-}), bicarbonate (HCO_3^-), sulfate (SO_4^{2-}), chloride (Cl^-), and Selenium (Se) were selected to evaluate their effects on arsenic removal.

Results and Discussion:

Arsenic contamination in wastewater was sucessfully removed by K-OMS2 coupled with Fe-BTC. Before use in the column, K-OMS2 and Fe-BTC powders were coated on the ceramic ball. From the results, in the single-column test, K-OMS2 (coated) maintained good efficiency to oxidize As(III) for a 3-round reuse cycle with lower than groundwater standard of Mn and K leaching. In the Fe-BTC (coated) column test, adsorption kinetics fit well with the Yoon-Nelson model having the maximum adsorption capacity of 52.60 mg/g and Fe leaching of 0.23 mg/L. With two columns combined, the system enabled to remove total As for 60% within 2,200 min.

In part of CeO_2, the results revealed that Ceria calcined at 250 °C showed maximum adsorption capacities of As(III) reaching 21.27 mg/g. The adsorption behavior of As(III) was well fitted to the Freundlich isotherm and a pseudo-second-order model. The As(III) adsorption

mechanisms as complexation were conducted between hydroxyl groups and redox transformation between As(III) and CeO_2.

As results of effect of ions species, PO_4^{3-}, HCO_3^-, SO_4^{2-} and Se play the role of inhibiting arsenic removal. Hence, it was suggested that the arsenic removal by the nanoiron process can be improved through pretreatment of PO_4^{3-} and Se. For pre-treatment of Se, this study demonstrated that Se^{6+} could be effectively removed by Nano zerovalent Iron supported on Zeolite (Z-NZVI). The batch experiments indicated that Z-NZVI had more active sites available for Se^{6+} rapid reduction and sorption, resulting in higher removal kinetic rate.

Acknowledgements

This work was financially supported by the Thailand Research Fund (MRG6180196), Office of the Higher Education Commission, the Research and Technology transfer affairs of Khon Kaen University, and Center of Excellence on Hazardous Substance Management (HSM), Chulalongkorn University. I would like to express my greatest gratitude appreciation to my mentor Assoc. Prof. Dr. Nurak Grisdanurak for his mentorship and guidance.

Visanu Tanboonchuy

TABLE OF CONTENTS

Chapter 1

Introduction to the research problem and its significance

Contamination of arsenic (As) in the environment is a serious concern due to it is a human carcinogen that attacks multiple sites in the human body (Figure 1.1). It can enter the human body either from respiration or through the mouth. Consuming water with high level of arsenic will cause Blackfoot disease and cancers of skin, lung, bladder, kidney, liver and colon (Mohan & Pittman, 2007). There are reports that As may affect the quality of paddy rice and its products, which are the important food in Thailand. According to previous study, it confirmed that rice is more efficient in As uptake and accumulation (Mukherjee et al., 2017).

Figure 1.1 Blackfoot disease and cancers of skin (Rice RH, Mauro TM., 2017).

There are studies about the arsenic contamination in water and soil from agricultural areas in Nakorn Si Thammarat, Nakhon Pathomm, and Loie. The results revealed that the arsenic content of water exceeds by 40–500 times the 10 μ/L concentration, which is the accepted safety

level set down by U.S. EPA. (Williams et al., 1996; Patarasiriwong et al, 2004; Smedley & Kinniburgh, 2001).

Common forms of As in natural water are arsenite (As(III)), mainly found in reducing condition, and arsenate (As(V)), a stable form in oxidizing state. As(III) is much more toxic and more transportable compared to As(V) (Smedley & Kinniburgh, 2001). Currently, the traditional treatment processes for arsenic removal are effective primarily for As(V) removal, while As(III) requires a pre-oxidation step which makes it more difficult to remove. To achieve greater As removal, As(III) pre-oxidation followed by co-precipitation/adsorption of the As(V) is usually employed. **This two-step process complicated operation, high cost, and low As removal efficiency. To economically and effectively remove As from groundwater, new innovative technologies must be employed. More specifically, treatment technology that can remove both As(III) and As(V) simultaneously is desired.**

Numerous oxidants or oxidant-generating systems have been tested for As(III) oxidation. For example, O_2 and/or ozone, hydrogen peroxide, and TiO_2/UV systems (Bissen, Vieillard-Baron, Schindelin, & Frimmel, 2001; M.-J. Kim & Nriagu, 2000a; Pettine, Campanella, & Millero, 1999a). Manganese dioxide (MnO_2) or manganese octahedral molecular sieve (K-OMS2) has been proven effective in oxidizing of pollutants (Yodsa-nga, Millanar, Neramittagapong, Khemthong, & Wantala, 2015). MnO_2 has relatively low oxidation potential and thus fit for specific oxidation of As(III), but its low adsorption capacity limits its application as adsorbent for As(V) removal (AlOmar, Alsaadi, Hayyan, Akib, & Hashim, 2016; Millanar, Yodsa-nga, Khemthong, & Daniel, 2013)

While various common porous nanoparticle adsorbents, such as activated carbon, porous alumina, zeolite, and diatomite, can be used for As(V) removal (Atribak et al., 2010; Dhakshinamoorthy et al., 2012; Langmuir, 1916; Shahid & Nijmeijer, 2014). Metal organic frameworks (MOFs) are recently developed engineered, porous materials with extremely high porosity, high surface area, and controlled crystallinity. With their unique properties, MOFs are considered a promising candidates for various applications including adsorption (El-Sawy et al., 2014). The role of Iron (III) trimesic (Fe-BTC), one kind of MOFs, as arsenic adsorbent was investigated previously, and the exceptionally strong and irreversible interaction between arsenic and iron oxide was reported (Duan et al., 2015). The coordination polymers of Fe-BTC also possess high thermal and mechanical stability, which avoid the aggregation problem that nanoparticle materials generally suffer. These advantages make Fe-BTC becomes a more

promising candidate in heavy metal removal by adsorption process compared to other nanoparticle adsorbents (Hall, Eagleton, Acrivos, & Vermeulen, 1966).

The objective of this study is to develop a novel materials (manganese oxide coupled with metal organic frameworks coating on support materials) for As removal, which combined the oxidation and adsorption. Moreover, it was compared with another material such as Cerium(VI) Oxide (CeO_2). The K-OMS2 and Fe-BTC coated support materials was then developed to remove As(III) from the aqueous solution. K-OMS2 and Fe-BTC coated on support materials are synthesized and then characterized using X-ray diffraction (XRD), High-resolution transmission electron microscopy (HR-TEM), and X-ray photoelectron spectroscopy (XPS). The mechanism of arsenic removal using K-OMS2 coupled with Fe-BTC was also proposed. Accordingly, the expected mechanism of As(III) removal using K-OMS2 coupled with Fe-BTC is shown in Figure 1.2. In this scheme, As(III) is first oxidized by K-OMS2 and As(V) is formed as a result. Then As(V) is readily adsorbed on Fe-BTC.

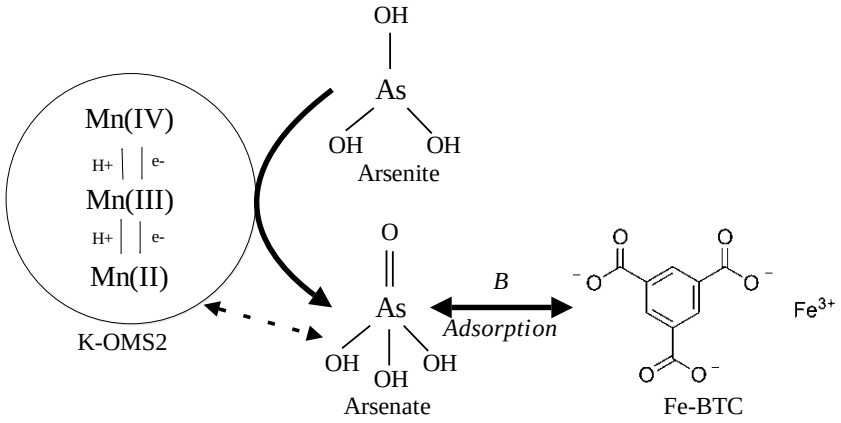

Figure 1.2 Expected mechanism of arsenic oxidation and adsorption by K-OMS2 and Fe-BTC.

In addition, the cation/anion species dissolving in water such as Phosphate (PO_4^{3-}), Bicarbonate (HCO_3^-), Sulfate (SO_4^{2-}), and Chloride (Cl^-), have been reported to affect in arsenic removal (Jegadeesan et al., 2005; Sun et al., 2006; Biterna et al., 2007). Currently, there still remains lack of information regarding the influence of mixture of background species and

competitive species such as Selenium (Se) on the arsenic removal. Thus, combined influences of background species and Se on arsenic removal are observed. Finally, the field groundwater spiked with arsenic is used to test the potential of the novel treatment process. In addition, fixed-bed column experiments were performed to evaluate the effectiveness of synthesized material as a reactive medium in column.

Main objective

To develop a novel process for arsenic removal, which combined the advantages of K-OMS2 and Fe-BTC coating on support materials for simultaneous oxidation and adsorption

Specific objectives

1. To investigate the methods for synthesis of novel materials, K-OMS2 and Fe-BTC, to enhance performance of arsenic removal
2. To investigate the another material, CeO_2, to compare with K-OMS2 and Fe-BTC for arsenic removal
3. To investigate the effects of conditions on arsenic removal. The reaction kinetics and mechanism of arsenic removal were elucidated: Batch and column studies
4. To study an effects of water quality on arsenic removal. Deionized water and simulated water with multi-ion species was induced in the water quality parameter
5. To study an effect of competitive material such as Selenium (Se) for arsenic removal, also the process for Se removal was proposed

Scope of research

1. K-OMS2 and Fe-BTC coating on support materials wwere synthesized by solvothermal method.
2. The another material tested to compare with K-OMS2 and Fe-BTC is CeO_2
3. In part of effect of ions on arsenic removal, four species selected and investigated are SO_4^{2-}, PO_4^{3-}, HCO_3^-, and Cl^-.
4. Competitive material used in this study is Selenium (Se)
5. The groundwater was collected from groundwater site in Khon Kaen Province. The groundwater was spiked with arsenic to obtain an arsenic concentration studied.
6. Kinetic models used in part of column study are Thomas model and Yoon-Nelson model.

Chapter 2

Literature review

2.1 Arsenic

Arsenic is classified as a group A carcinogen, meaning agents with adequate human data to demonstrate the causal association of the agent with human cancer, by the United State Environmental Protection Agency (U.S. EPA). Consuming water or foods with high level of arsenic will cause Blackfoot disease and cancers of skin, lung, bladder, kidney, liver and colon (Mohan & Pittman, 2007). Arsenic may affect the quality of paddy rice (Oryza sativa L.) and its products, which are the staple food in Southeast and South Asia (Ma et al., 2016).

Arsenic is stable in several oxidation states, such as the arsenite (As(III)) and arsenate (As(V)), mainly found in reducing and oxidizing conditions, respectively, which the toxicity of As(III) is 25-60 higher than that of As(V) (Smedley & Kinniburgh, 2001). Both are the most common forms in natural water. The dominant species of arsenic depend greatly on conditions of environment (Figures 2.1 and 2.2). As is mainly found as arsenite [As(III)] and arsenate [As(V)] in paddy soil (Zheng et al., 2012). It can reach high concentrations in plants. Several studies have demonstrated that oxic conditions in soils play an important role in As uptake and speciation in rice plants (Wu et al., 2017; Xu et al., 2008).

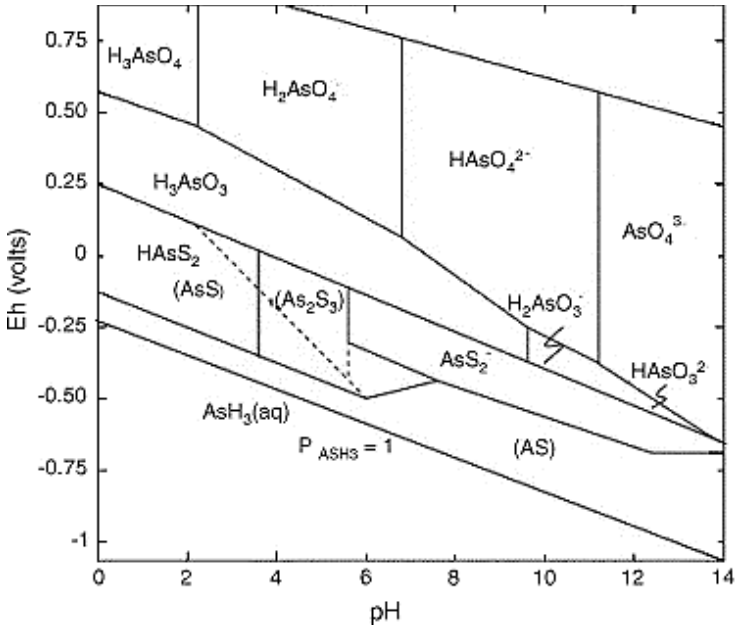

Figure 2.1 Eh-pH diagram of arsenic (Mohan & Pittman, 2007)

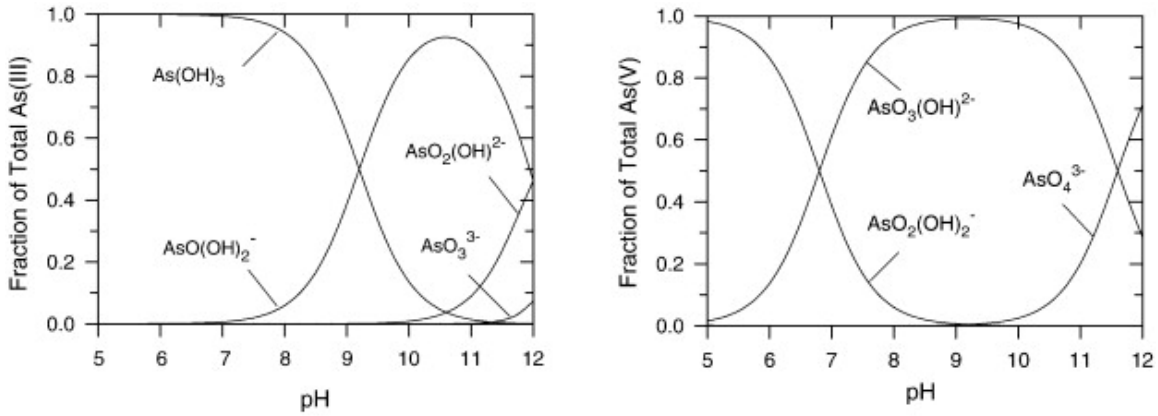

Figure 2.2 As(III) and As(V) species in water at various pH (Sharma et al. 2009)

There are researches that study the arsenic contamination in water and soil from agricultural areas. The first case of arsenic contamination in Thailand was reported in 1987 in Ron Pibul District of Nakorn Si Thammarat Province, in the southern peninsula (Williams et al., 1996). At many sites, the arsenic content of water exceeds by 40–500 times the 10 μ/L concentration. Arsenic there may be from both point sources and diffuse sources (underground placer deposits) (Fordyce et al., 1995). Patarasiriwong et al. (2004) had been studied the arsenic contamination in

water and soil from agricultural areas in Ron Pibul District of Nakorn Si Thammarat Province. The 41 sampling sites were selected in 4 Tambols (sub-districts). Total arsenic concentration in water samples from Tambol Ron Phibul, Kuan Pang, Kuan Chum and Hin Tok were in the range of 0.26–663, 0.26–9.9, 4.9–326 and 0.26–13.5 µg/L, respectively. in Whereas, total arsenic concentration surface soil (0–15 cm) of Tambol Ron Phibul, Kuan Pang, Kuan Chum and Hin Tok were in the range of 4.9–1385, 0.11–18.2, 3–283 and 2.3–37.2 mg/kg dry wt., respectively. And in sub-surface soil (15-30 cm) were in the range of 9.6–1549, 3.34–16.7, 3.1–163 and 2.5–40.7 mg/kg dry wt., respectively. Another researcher had speculated the Buddhamonthon Subdistrict of Nakhon Chaisi District, Nakhon Pathom Province because it contains relatively young sediments that could develop a combination of geochemical conditions, such as reducing conditions, or oxidizing, high pH that allow the release of arsenic. The result reported that 5 mg/L of arsenic or less were detected (Smedley et al., 2001).

2.2 Arsenic treatment techniques

As a common practice, the process for arsenic removal begins with pre-oxidation step to transform As(III) to As(V) (Lackovic et al., 2000). Following this, the As(V) is then removed by coagulation and filtration, lime softening, ion exchange, and reverse osmosis (Triszcz et al., 2009). Coagulation process is difficult to achieve on low concentration levels of arsenic treatment. It requires a pretreatment step such as lime softening, hardness reduction. These are expensive processes and is not recommended. Ion exchange processes combined with an oxidation pretreatment step has been shown to reduce total arsenic in finished drinking water to low levels but it is restricted for water supplies with low concentrations of total dissolved solids and sulphate (Clifford et al., 1999). Reverse osmosis systems generally require large quantities of influent water to overcome the operating cost (U.S. EPA, 2000). To comply with low cost operation, adsorption is a promising alternative technique for arsenic removal (Sun et al., 2006).

To achieve greater arsenic removal, As(III) pre-oxidation followed by co-precipitation/adsorption of the As(V) is usually employed. This two-step process complicated operation, high cost, and low arsenic removal efficiency (Qi, Zhang, & Li, 2015). Combination of oxidation and adsorption process, which oxidizes As(III) to As(V) and adsorb the As(V), has advantages in arsenic removal. Numerous oxidants or oxidant-generating systems have been tested for As(III) oxidation. For example, O_2 and/or ozone, hydrogen peroxide, and TiO_2/UV

systems (Bissen et al., 2001; M.-J. Kim & Nriagu, 2000b; Pettine, Campanella, & Millero, 1999b). Manganese dioxide (MnO_2) or manganese octahedral molecular sieve (K-OMS2) has been proven effective in oxidizing of As(III) and other pollutants (Yodsa-nga et al., 2015). MnO_2 has relatively low oxidation potential and thus fit for specific oxidation of As(III), but its low adsorption capacity limits its application as adsorbent for As(V) removal (AlOmar et al., 2016; Millanar et al., 2013)

While various common porous nanoparticle adsorbents, such as activated carbon, porous alumina, zeolite, and diatomite, can be used for As(V) removal (Atribak et al., 2010; Dhakshinamoorthy et al., 2012; Langmuir, 1916; Shahid & Nijmeijer, 2014), the adsorption capacity of conventional adsorbents were generally limited by their chemical properties and irregular pore structures (Veličković et al., 2012). Metal organic frameworks (MOFs) are recently developed engineered, porous materials with extremely high porosity, high surface area, and controlled crystallinity. With their unique properties, MOFs are considered a promising candidates for various applications including adsorption (Nandasiri, Jambovane, McGrail, Schaef, & Nune, 2016).

2.3 K-OMS2

Manganese oxides such as MnO_2, Mn_2O_3, Mn_3O_4 and MnO are well-known catalysts for the oxidation of numerous volatile organic compounds (S. C. Kim & Shim, 2010; Tian et al., 2012). These manganese structures have been studied for CO oxidation at low temperature and the order of oxidation efficiency is Mn_2O_3 N MnO_2 ≥ MnO (Ramesh et al., 2008). The efficiency of manganese oxide for catalytic oxidation is affected by three factors including the presence of Mn^{3+}/Mn^{4+} redox couple ratio, high surface area, and ability of the lattice oxygen on their surfaces (Gandhe, Rebello, Figueiredo, & Fernandes, 2007).

Nowadays, octahedral molecular sieve K-OMS2 (Figure 2.3) plays an important role in the field of catalytic oxidation. It is a type of manganese oxide with 2 × 2 tunnels and MnO6 octahedral chains in one dimensional 4.6 Å × 4.6 Å structure (Santos et al., 2014; Schurz et al., 2009). K-OMS2 has mixed oxidation states of Mn ion species with Mn^{2+}, Mn^{3+} and Mn^{4+} (Hou et al., 2013). An increase in aging temperature during hydrothermal process can induce the transformation of K-OMS2 to K-OMS 7 (Qiu et al., 2011). Normally, K-OMS 7 is less active than K-OMS2 due to its lower ratio of Mn^{3+}/Mn^{4+}. This ratio strongly affects the lattice oxygen on the surface of K-OMS2 (Wang et al., 2012). Higher ratio ofMn3+/Mn4+ increases the amount of lattice oxygen and improves the performance of the catalyst. Yamashita reported that Mn_2O_3 provided

large amount of lattice oxygen on the surface and also showed exceptional oxygen desorption (Yamashita & Vannice, 1997). Yodsa-nga (2015) also reported that the nanowire K-OMS2 can be prepared by hydrothermal technique without calcination step. The results presented that he lowest aging temperature and the highest aging time (75 °C and 21 h) resulted to the lowest Mn3 +/Mn4 + ratio which possessed the highest specific area and the highest benzene degradation.

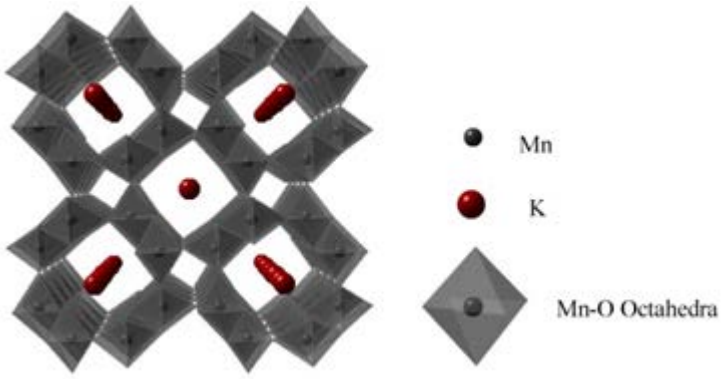

Figure 2.3 K-OMS2 structure (Dharmarathna et al., 2014)

2.4 Metal-organic frameworks (MOFs) / Iron (III) trimesic (Fe-BTC)

Metal-organic frameworks (MOFs) are composed of metal ions/clusters and organic ligands, which are one of the hybrid materials. Because of their high chemical, thermal stability, and changeability of their physicochemical properties, MOFs have been used in many applications such as gas storage, adsorption, drug delivery, separation, sensors, catalysis, etc. Over the last decade, MOFs have become one of the most extreme interesting research topic to develop and enhance structure, synthesis method, and function properties. The method of MOFs synthesis has been commonly prepared via liquid-phase syntheses by solvents (ethanol, methanol, water, dietylformamine, etc.). The method and solvent used affect the properties of the synthesized materials (hydrophobic-hydrophilic, reactivity, solubility, redox potential, etc. (Dey, Kundu, Biswal, Mallick, & Banerjee, 2014; Li, Sculley, & Zhou, 2012; Van de Voorde, Bueken, Denayer, & De Vos, 2014). In addition, MOFs can be regenerated by solvent solution (Chen, Zhang, Guan, & Li, 2012; García et al., 2014) that would be advantageous for chemical and toxicity reduction in wastewater treatment.

The use of MOFs in removing heavy metals from water is a growing area such as Wang et al. (2015) studied the $Cu_3(BTC)_2$-SO_3H framework as an effective cadmium(II) adsorbent. The results showed that the optimal pH value for Cd(II) adsorbed was found to be 6. Below that value active sites were increasingly occupied by protons, limiting adsorption, while at pH greater than 6, Cd ions precipitated in the form of hydroxide salts. Saleem et al. reported in 2015 on the ability to use the zirconium-based MOF, UiO-66-NHC(S)NHMe, as an adsorbent for lead(II) removal. The maximum adsorption capacity was reported at 232 mg/g for lead(II)

Iron (III) trimesic (Fe-BTC) is the one of a crystalline porous material namely metal-organic frameworks (MOFs) that have been interested and investigated in structural, synthesis, and application for several decade. This material consist of benzene-1,3,5-tricarboxylate (BTC) and iron trimeric clusters, which achieved the 1300 – 1600 m^2/g range of surface area, high stability, strong Lewis acid site (Autie-Castro, Autie, Rodríguez-Castellón, Aguirre, & Reguera, 2015; Sciortino, Alessi, Messina, Buscarino, & Gelardi, 2015)

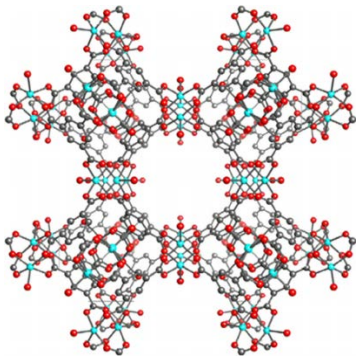

Figure 2.4 Representation of Fe-BTC structure; carbon atoms grey, oxygen atoms red, and iron atoms light-blue (Salman Shahid, 2014)

The synthesis of MOFs typically by solvothemal (also hydrothermal method when water is the solvent) due to simple. In a previous researcher reported, the metal-organic frameworks (MOFs) synthesis have interested because the difference of methods can bring about the variance of MOFs and apposite for the large-scale process operation (Y. Lee, Kim, & Ahn, 2013; Topologies, Stock, & Biswas, 2012). Fe-BTC have been applied catalytic, adsorption, separation, and so on.

Salman Shahid, (2014) applied Fe-BTC in mixed-matrix polymer membranes (MMMs) for high pressure gas separation (Figure 2.5).

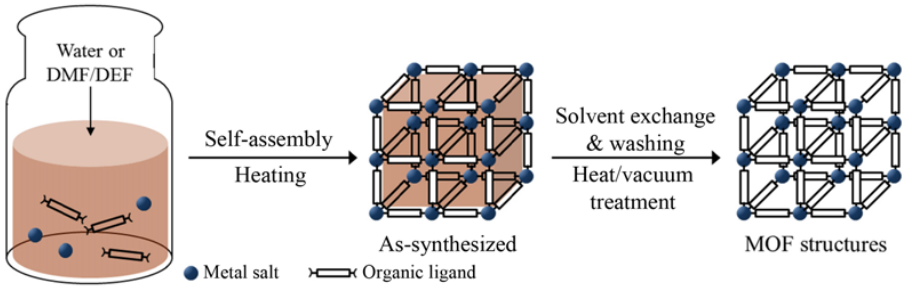

Figure 2.5 Synthesis of MOFs typically by solvothemal (Y. R. Lee, Kim, & Ahn, 2013)

The result shows a CO_2/CH_4 selectivity and permeability increase of 62% and 30% respectively (mix gas feed of 40 bar) by MMMs with 30% Fe-BTC. In heavy metal removal, Fe-BTC was used to adsorb an arsenic (As) from liquid phase compare with Fe_2O_3 nanoparticle. It shows the great capacity than Fe_2O_3 nanoparticle 6.5 times (Zhu et al., 2012). Nevertheless, the performance application of Fe-BTC have been a few reported.

2.5 Arsenic removal by Cerium(IV) oxide (CeO_2)

Ceria (CeO_2), showed efficient arsenic removal over a pH range from 3 to 11 (Li et al., 2012), particularly toward As(III) with high content of hydroxyl groups suggested as responsible for its excellent performance. Moreover, despite the rare earth terminology, ceria and other cerium salts are cheap and show potential as cost-competitive materials. Ceria has a fluorite structure and is an important material with good mechanical, chemical, and thermal stabilies (Arii et al., 2002). Ceria synthesized through a combined oxidation and adsorption process was successfully used to remove As(III) (Yu et al., 2016); however, high calcination temperature was required which increased synthesis cost and impacted CeO_2 crystal characteristics such as pore size and surface hydroxy groups. Ceria synthesis at low calcination temperature for uptake of As(III), adsorption performance during high concentration As(III) uptake, and the mechanism of adsorption have yet to be studied and reported using advanced analytical tools.

2.6 Removal of Selenium (Se) as competitive species

Selenium is an essential nutrient element for life in trace amounts, but it is extremely toxic at higher concentrations. Selenium concentrations in water environments have increased, not only in natural resources, but also from anthropogenic practices such as coal-fired power plants, agricultural irrigation drainage, the combustion of fossil fuels, and mining operations (Gonzalez et al., 2010).

Selenium exists in water in several forms depending on its oxidation states, such as selenate (SeO_4^{2-} or Se^{6+}), selenite (SeO_3^{2-} or Se^{4+}), selenium (Se^0), selenide (Se^{2-}), and organic selenium. Se^{6+} and Se^{4+} are found in most aqueous media and comprise the predominant chemical forms (Jegadeesan et al. 2015). Generally, Se^{6+} is considered the most toxic species and oxidized form with high solubility in water. Se^{4+} is less available to organisms as a consequence of its affinity to adsorption sites of sediment and soil constituents (Yamani et al. 2014). Normally, Se^{6+} can be adsorbed in an outer-sphere adsorption manner weaker than inner-sphere adsorption, which could be the reason for less effective Se^{6+} removal using conventional adsorbents (Fu et al., 2014). During the infiltration of surface water, mobile Se^{6+} is weakly adsorbed by minerals, thus becoming the main species in groundwater (Gibson et al., 2012). Hence, Se^{6+} is more mobile in groundwater and most Se^{6+} from polluted water ends up in groundwater. Therefore, it is very important to identify and evaluate additional potential methods for the removal of selenium from wastewater before it is discharged into the natural environment. Strategies for the removal of soluble selenium in water will most likely involve the reduction of Se^{6+} into selenium species with lower valence (Se^{6+}, Se^0, and/or Se^{2-}). Selenium is competitive spices for arsenic treatment. The pretreatment process for Selenium removal is necessary to increase the performance of arsenic removal.

Chapter 3

Methodology

3.1 Chemicals

Chemicals were used in this study included manganese acetate tetrahydrate ($(MnCH_3COO)_2 \cdot 4H_2O$, ACROS Organics), potassium permanganate ($KMnO_4$, CARLO ERBA), glacial acetic acid (CH_3COOH, Merck), Iron (III) chloride hexahydrate ($FeCl_3 \cdot 6H_2O$, QRëC), 1,3,5-benzenetricarboxylic acid (trimesic, H_3BTC, Sigma-Aldrich), Sodium (meta) arsenite, ($NaAsO_2$, Ajax Finechem), and Sodium arsenate dibasic heptahydrate ($Na_2HAsO_4 \cdot 7H_2O$, Sigma- Aldrich), $Ce(NO_3)_3 \cdot 6H_2O$ (99%) (Merck, sodium selenate decahydrate ($Na_2SeO_4 \cdot 10H_2O$, Sigma-Aldrich), sodium selenite (Na_2SeO_3, Sigma-Aldrich), sodium hydroxide (NaOH, RCI Labscan), iron (II) sulfate heptahydrate ($FeSO_4 \cdot 7H_2O$, QRëC), and sodium borohydride ($NaBH_4$, Loba Chemie Pvt. Ltd.)All chemicals are analytical grade (99% purity).

3.2 K-OMS2 and Fe-BTC synthesis and Characterization (Part 1)

For K-OMS2 synthesis, a fixed mole ratio of 0.75 $KMnO_4/Mn(CH_3COO)_2$ is selected to prepare K-OMS and synthesis procedure is performed based on a previous study. $KMnO_4$ solution is added dropwise to $Mn(CH_3COO)_2$ solution under vigorous mixing. pH of the solution is adjusted to an acidic condition (pH ≥ 3.5) and transferred to an autoclave for hydrothermal process. In the final step, the obtained black slurry is washed with reversed osmosis (RO) water and dried at 373 K for 4 hour and then 473 K for another 2 hour.

Fe- BTC was synthesized by hydrothermal method. 1 mmol Iron (III) chloride hexahydrate ($FeCl_3 \cdot 6H_2O$) is mixed with 1 mmol 1,3,5-benzenetricarboxylic acid (trimesic, H_3BTC) for 30 minutes. The mixed solution is heated at 373 K for 24 hour in a Teflon-lined stainless steel autoclave in an oven. Then the material is centrifuged and dried at 393 K for 5 hour in a furnace oven and at 373 K for 3 hour in an oven.

The K-OMS2 and Fe-BTC coating on support material will be prepared as follows. Activated alumina ball was soaked with DI water. Then K-OMS2 and Fe-BTC were mixed with activated alumina and drying overnight at 100°C.

Crystallinity of K-OMS2 and Fe-BTC are determined using X-ray diffractometer (XRD) (D8 Discover, Bruker AXS). Particle shapes are observed using High resolution transmission electron microscopy (HR-TEM) (JEM-2100Plus, JEOL) and X-ray photoelectron spectroscopy (XPS) (AXIS Ultra DLD, Kratos Analytical Ltd.).

3.3 Batch experiments (Part 2)

3.3.1 As(III) oxidation by K-OMS2. (Part 2.1)

Batch oxidation experiments are conducted by combining initial 5 mg/L As(III) with 0.5 g K-OMS2. Contact time of all experiments is in the range of 0-90 min with varied temperatures of 303-333 K. Total concentration of arsenic (As(III) and As(V)) are determined by graphite furnace atomic absorption spectroscopy (GF-AAS) (Analyst 800, Perkin Elmer). Determination of individual arsenic species is conducted using an anion-exchange cartridge (A502P, Purolite). As(V) is retained in the cartridge while As(III) is allowed to pass through, rendering the separation of As(III) and As(V) from each other. The eluent is then analyzed for As(III) concentration by GF-AAS. As(V) concentration is obtained by subtracting the measured As(III) concentration from total arsenic concentration.

3.3.2. Arsenic adsorption by Fe-BTC (Part 2.2)

Batch adsorption experiments are conducted by combining initial 5 mg/L As(V) with 0.5 g Fe-BTC and then mixing for 0-90 min. The sampling is then analyzed for arsenic concentration by GF-AAS. The equilibrium data is fitted to the Langmuir and Freundlich isotherm models, and their equations are shown as the following equations (3.1) and (3.2).

Langmuir model: $$\frac{1}{q_e} = \frac{1}{q_m K_L C_e} + \frac{1}{q_m} \quad (3.1)$$

Freundlich model: $$\ln q_e = \ln K_F + \left(\frac{1}{n}\right) \ln C_e \quad (3.2)$$

Where Ce is the concentration of As(V) solution at equilibrium (mg/L); qe is the corresponding adsorption capacity (mg/g); qm (mg/g) and KF (mgg-1)(Lmg-1)1/n are the constants related to adsorption capacity in Langmuir and Freundlich isotherm models, respectively.

3.3.3 Combination of oxidation and adsorption processes (Part 2.3)

In order to conducted the oxidation and adsorption processes simultaneously, 5 mg/L of As(III) is mixed with 0.5 g K-OMS2 and Fe-BTC for 0-90 min. The sampling is then analyzed for arsenic concentration by GF-AAS. Effect of mass ratio of K-OMS2:Fe-BTC on As(III) removal is studied by varying the ratios of K-OMS2:Fe-BTC by 1:0.5, 0.5:0.5, and 0.25:0.5 gram.

3.3.4 Effect of background species on arsenic removal (Part 2.4)

Multiple species system, the initial arsenic concentration is prepared at a level as high as 1000 µg/L. Two levels of low and high concentrations for each selected species are listed as follows: SO_4^{2-}: 10, 100 mg/L; HCO_3^-: 50, 500 mg/L; PO_4^{3-}: 1, 5 mg/L; Cl^-: 50, 500 mg/L. The solution pH is adjusted at the beginning of the experiment to 7.90 + 0.1.

3.4 Arsenite (As(III)) removal by CeO_2 (Part 3)

Experiments were conducted to examine the kinetics and isotherms. Experiments to determine kinetics of the As(III) removal reaction with CeO_2 at room temperature were carried out by batch method. Here, 500 mL of As(III) solution of C_0 from 50 mg/L was mixed with 0.5 g of CeO_2 into a 600 mL beaker and agitated at 200 rpm using a speed adjustable agitator, with monitoring of pH and oxidation-reduction potential (ORP). The CeO_2 particles were separated by a syringe filter 0.45 µm and analyzed for residual arsenic concentration. To investigate isotherms, 50 mL of As(III) solution of C_0 (mg/L) ranging from 1.0 to 80.0 was mixed with 0.05 g of CeO_2 in a centrifugal tube, and then subjected to 50 rpm for 30 min before separating the CeO_2 particles using a syringe filter 0.45 µm.

3.5 Selenium removal by nanomaterials (Part 4)

As previous part, Selenium is competitive spices for arsenic treatment. The pretreatment process for Selenium removal is necessary to increase the performance of arsenic removal. Thus, Batch experiments were conducted by combining 500 mL initial 15 mg/L of Se^{6+} with 0.75 g of Zeolite (Z), 0.15 g of Nano zero valent iron (NZVI), and 0.90 g of Z-NZVI deriving from 0.75 g of Z and 0.15 f of NZVI synthesis. Contact time for all experiments was in the range of 0–30 min. The eluent was then analyzed for selenium concentration by inductively coupled plasma-optical

emission spectrometry (ICP-OES). The previous publication has suggested that the reaction rate could be estimated with conventional pseudo-first-order kinetics:

$$\frac{d[Se(VI)]}{dt} = -k_{obs}[Se(VI)] \qquad (3.3)$$

The concentration of selenium in the aqueous phase (mg/L), k_{obs} is the observed rate constant (min^{-1}), and t is the reaction time (min).

3.6 Column Study (Part 5)

Part 5 emphasizes on the laboratory column experiment. For K-OMS2 powder synthesis, a potassium permanganate solution (0.25M, 40 mL) was mixed with manganese acetate tetrahydrate solution (0.33M, 40 mL). The pH of the solution was adjusted to an acidic condition (pH ≥ 3.5) by using acetic acid and stirred well for 1 h. The mixture was transferred to an autoclave for hydrothermal processing at 100°C for 3 h. Then, a black slurry was obtained and washed with deionized (DI) water to retain pH = 7. The black precursor was dried at 100°C for 3 h. Finally, the black powder of K-OMS2 was obtained. For Fe-BTC powder synthesis, iron(III) chloride hexahydrate solution (1 M, 75 mL) mixed with a 1,3,5-benzene tricarboxylic acid solution (1M in ethanol, 75 mL). The mixture was transferred to an autoclave for hydrothermal processing at 100°C for 24 h. Then, an orange jelly-like substance was obtained and washed with DI water to retain pH = 7. The orange precursor was dried at 120°C for 4 h. Finally, the orange powder of Fe-BTC was obtained.

To prepare the K-OMS2 and Fe-BTC coated on ceramic balls, so-called K-OMS2 (coated) and Fe-BTC (coated), respectively, the preparation procedure was restricted by optimal conditions of coating from our previous work (Supannafai et al. 2018a; Supannafai et al. 2018b; Supannafai et al. 2018c). Firstly, the starting materials in the weight ratio of the K-OMS2 powder or the Fe-BTC powders to the ceramic balls of 1 to 50 were introduced to a 2,000-mL-beaker. It was then transferred and set on an orbital shaker to perform the coating via the mechanical orbital shaking technique at 160 rpm for 24 h. Then, the coated materials were dried at 120°C for 24 h. Finally, the K-OMS2 (coated) and Fe-BTC (coated) were ready for characterization and packing in the continuous fixed-bed columns.

The K-OMS2 powder, Fe-BTC powder, K-OMS2 (coated), and Fe-BTC (coated) were characterized to determine crystallinity using an X-ray Diffractometer (XRD) (D8 Discover, Bruker AXS) with a Cu Kα radiation (= 0.1514 nm) at 40 mA, an increment of 0.02°/step, a scan speed of 0.1 s/step, and 40 kV. The scan range was 10–80° for K-OMS2 and 1–40° for Fe-BTC at 25°C. Besides, the x-ray absorption near edge structure (XANES) spectroscopy technique was conducted over the spent K-OMS2 powder, and the standards of As(III) from sodium arsenite, and As(V) from disodium hydrogen arsenate heptahydrate. The XANES was performed at Beamline 1.1: Multiple X-ray techniques, the Synchrotron Light Research Institute (public organization) located in Nakhon Ratchasima, Thailand. The Athena software was used to analyze the XANES spectra of the spent K-OMS2 powder and the standards.

The continuous fixed-bed column experiment was divided into three parts including 1) arsenite oxidation over K-OMS2 (coated) in a single continuous fixed-bed column, 2) arsenate adsorption over Fe-BTC (coated) in a single continuous fixed-bed column, and 3) total arsenic removal over K-OMS2 (coated) and Fe-BTC (coated) in combined continuous fixed-bed columns. The inlet at the bottom of the column was driven by a peristaltic pump to control flowrate at 5 and 10 mL/min, and the outlet was the top of the column. Their configurations were supposed to retain water leveling neatly contacted with the cross-section's material in the column and avoid the flowrate with gravity force. Then, the K-OMS2 (coated) and Fe-BTC (coated) were separately loaded into the individual columns at a bed-length of 10, 15, and 20 cm by closing the top and bottom os the packed ones with 2-cm-bed-lengths of cotton wool and glass beads as shown in Figure 3.1(a) and 3.2(b).

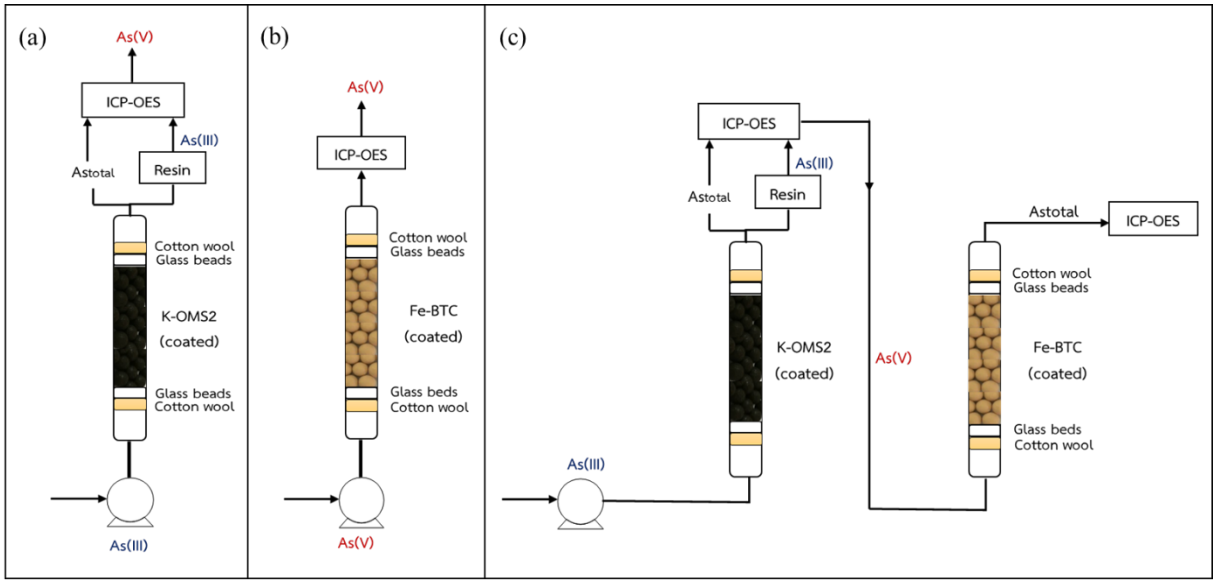

Figure 3.1 Continuous fixed-bed columns configuration: (a) K-OMS2 (coated) packed in a single column for As(III) oxidation, (b) Fe-BTC (coated) packed in a single column for As(V) adsorption, and (c) combined columns of K-OMS2 (coated) and Fe-BTC (coated).

In order to apply our adsorption results to the practical use, the adsorption kinetics were evaluated for the reaction pathways and mechanism of adsorption phenomena. The obtained parameters could be used to process upscaling. In general, two kinetic models,

Thomas model and Yoon-Nelson model, are used to investigate.

Thomas model can be described by equation (3.4) and is linearized for the analysis as shown in equation (3.5).

$$\frac{C}{C_0} = \frac{1}{1+\exp\left[\frac{K_T(q_0M-C_0V)}{Q}\right]} \quad (3.4)$$

$$\ln\left(\frac{C_0}{C}-1\right) = \frac{K_T q_0 M}{Q} - \frac{K_T C_0 V}{Q} \quad (3.5)$$

Where C and C_0 are the effluent and inlet gas concentration (mg/L), K_T is the Tomas rate constant (mL/min/mg), Q is volumetric flow rate (mL/min), q_0 is the maximum adsorption capacity (mg/g), M is adsorbent weight (g), and V is the throughput volume (mL).

Yoon-Nelson model can be written as the following form (Equation (3.6)):

$$\frac{C}{C_0} = \frac{1}{1+\exp\left[K_{YN}(\tau-t)\right]} \quad (3.6)$$

Where K_{YN} = Yoon-Nelson rate constant (L/min), t = sampling time (min), and $\boldsymbol{\tau}$ = the time required for 50% adsorbate breakthrough (min). The linearized form of the Yoon-Nelson model is as follows (Equation (3.7));

$$ln\left(\frac{C}{C_0-C}\right) = K_{YN}t - \tau K_{YN} \quad (3.7)$$

Where K_{YN} is Yoon-Nelson rate constant (L/min), t is sampling time (min), and $\boldsymbol{\tau}$ is the time required for 50% adsorbate breakthrough (min).

Chapter 4

Results and Discussion

4.1 K-OMS2 and Fe-BTC characterizations (Part 1)

In the coating process, PVA is used as a polymer binder to improve the surface of alumina ball. Comparison of PVA concentration is appropriated between 5% PVA and 10% PVA by the weighing method of K-OMS2/Al_2O_3-PVA after it is dried. The results showed that K-OMS2 can be coated on alumina ball with 10% PVA binder better than 5% PVA, determine from the weight of alumina ball after the coating process, which can be 86.40%, while 5% PVA can be coated at 80.26%. Therefore, 10%PVA was used for K-OMS2 coating in this study.

The suggested structures of K-OMS2 and K-OMS2/Al_2O_3-PVA were confirmed from XRD, as shown in Figure 4.1. The crystallinity of K-OMS2/Al_2O_3-PVA is decreased when compared to K-OMS2 powder because the coating process by mechanical orbital shaking technique affects the crystallinity of K-OMS2.

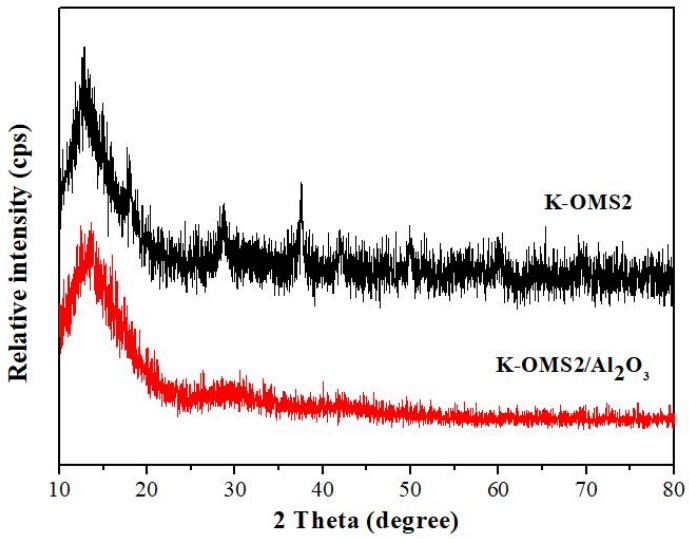

Figure 4.1 XRD pattern of K-OMS2 and K-OMS2/Al_2O_3-PVA

The surface morphology of K-OMS2/Al_2O_3-PVA was described by SEM, as seen in Figure 4.2, which found that the K-OMS2 particles have broken and combined agglomeration due to shaking from the coating process.

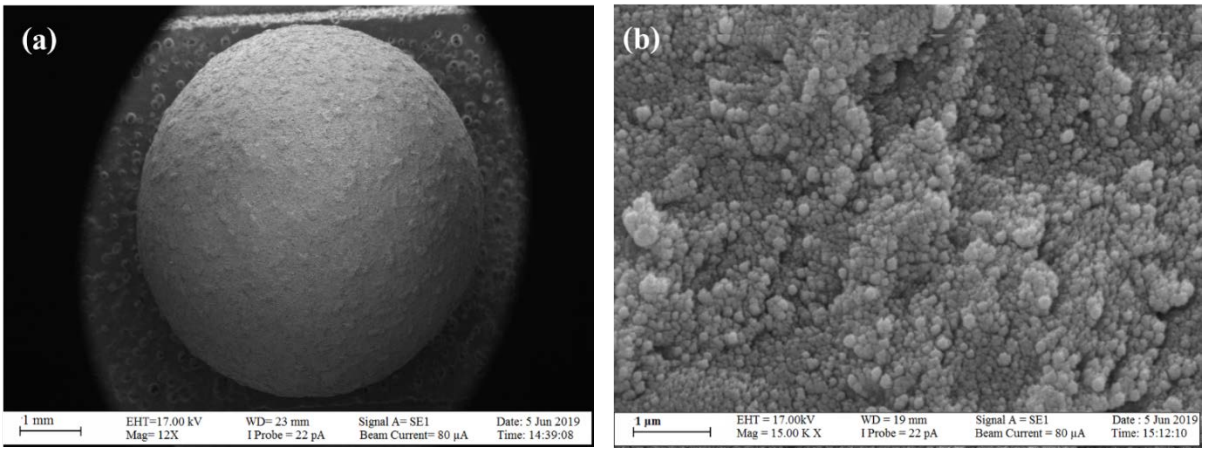

Figure 4.2 SEM image of K-OMS2/Al_2O_3-PVA (a) 12x and (b) 15,000x

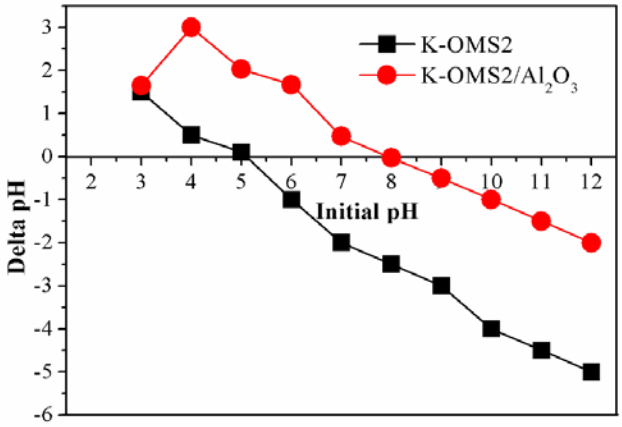

Figure 4.3 Point of zero charge of K-OMS2 powder and K-OMS2/Al_2O_3-PVA

For defining the surface charge of K-OMS2/Al_2O_3-PVA, as shown in Figure 4.3, the point zero of charge is 8. The pH is greater than 8, so the surface has negative charges. While pH was lower than 8, it will have a positive charge at the surface of K-OMS2/Al_2O_3-PVA. The pH_{pzc} of K-OMS2/Al_2O_3-PVA was different from K-OMS2 powder (pHzpc = 5) because Al_2O_3 have other elementals contents and functional groups of PVA induce to different functional groups thus a greater mass portion, which effect to active sites that will protonate excess H^+.

In addition to the above properties, this study also analyzed the specific surface area, pore-volume, and pore size. The BET surface area and pore volume of adsorbent are 212.65 m^2/g and0.45 cm^3/g, respectively by BJH method. The diameters of the size of K-OMS2/Al_2O_3-PVA pore

size distribution are the range of 2–50 nm and consisted of one sharp peak centered at 4.19 nm, with its mesopore following the IUPAC definition (2- 50 nm. Figure 4. 4 represents the N_2 adsorption/ desorption isotherm for K-OMS2/Al_2O_3-PVA. According to the IUPAC classification of adsorption, the isotherm is a type IV isotherm, which is a hysteresis loop. This is associated with capillary condensation taking place in the mesopores. The hysteresis loops are used to indicate pore shape, with the results showing the hysteresis loop is type H3, which is slit-shaped pores.

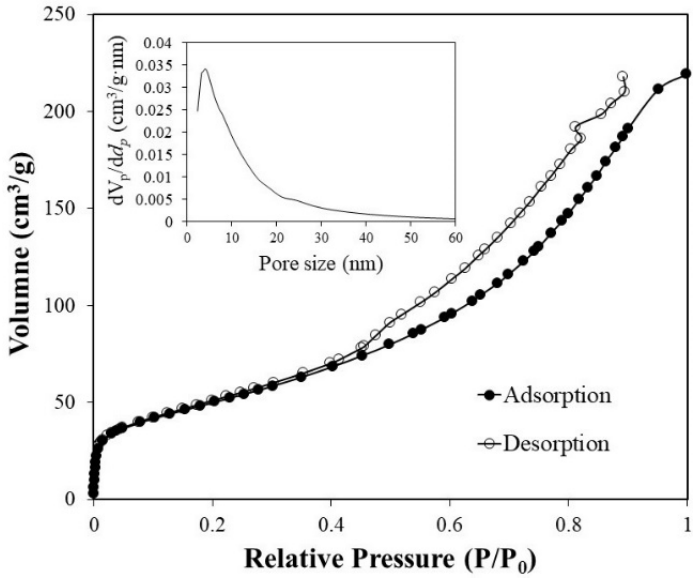

Figure 4.4 N_2 adsorption/desorption isotherm of K-OMS2/Al_2O_3-PVA, the insert shows the pore size distribution.

The XANES spectra of the spent K-OMS2 powder, and the standards of As(III), and As(V) are presented in Figure 4.5. This investigation was aimed at the mechanisms related to As(III) removal over the K-OMS2 (coated). Noted that the spent K-OMS2 powder was used instead of the spent K-OMS2 (coated) since the limitation of sample preparation for the XANES measurement. The edge shape varied between both the spent K-OMS2 powder, as an experimental sample, and As(III), and As(V), as reference compounds showing various oxidation states of As. The XANES spectrum of As(III) had an absorption edge at 11,869.0 eV while that of As(V) was at 11,872.8 eV which was similar to the absorption edge of the spent K-OMS powder. It, therefore, suggested that partial As(V) was possibly adsorbed on the spent K-OMS2 surface after As(III) oxidation leading to a loss in some active sites of K-OMS2 surface, consequently, the decrease of oxidation efficiency in the working column and the reuse cycle number.

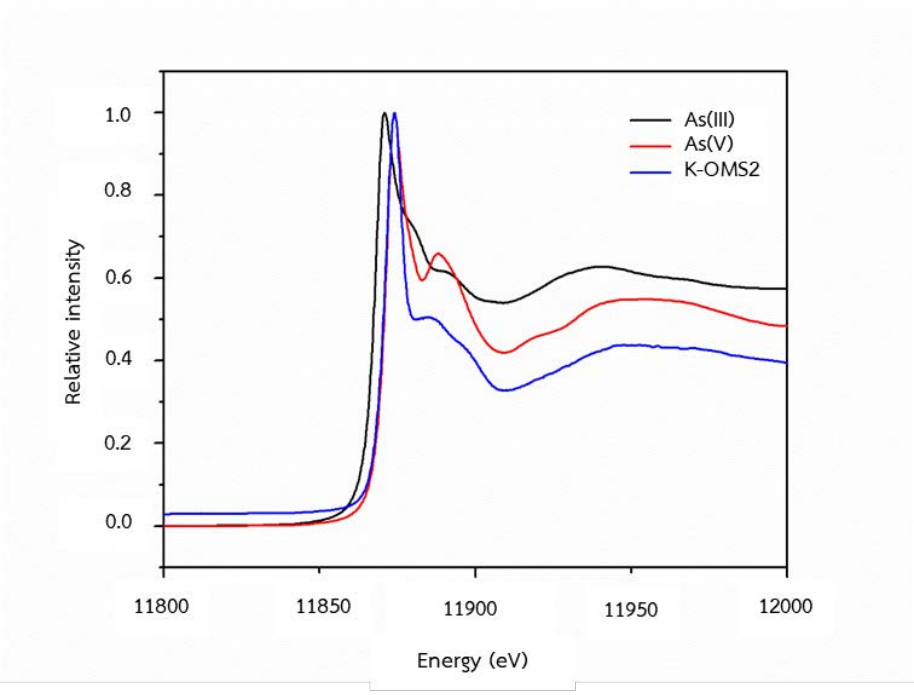

Figure 4.5 K-edge XANES spectra of spent K-OMS2 compare to As(III) and As(V) standards

4.2 Batch experiments

4.2.1 As(III) oxidation by K-OMS2 (Part 2.1)

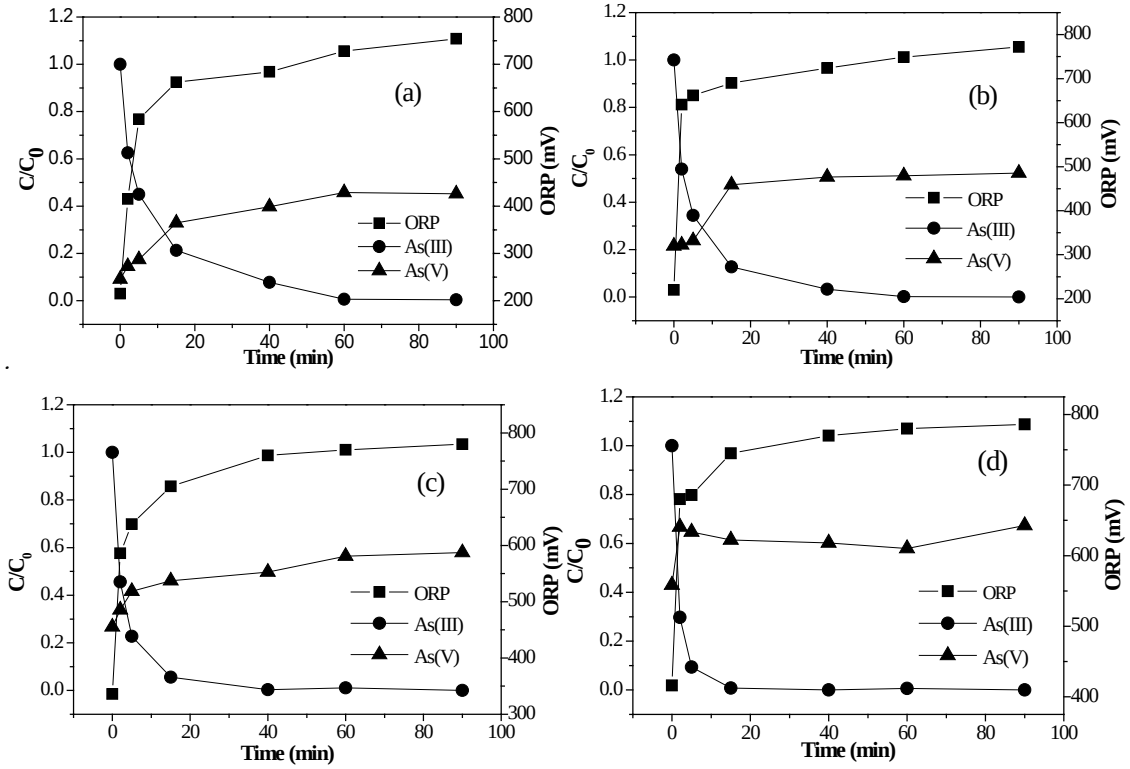

Figure 4.6 Relationships between contact time and residual arsenic at: (a) 303 K; (b) 313 K; (c) 323 K; and (d) 333 K.

Figure 4.6(a)-(d) present the relationship between the percentage of residues of arsenic and the Oxidation Reduction Potential (ORP) at different temperatures as a function of time. It can be observed that oxidation capacity increased as contact time and temperature increased. The results showed that percentage of As(III) decreased while percentage of As(V) and ORP values increased. This behavior was as expected as K-OMS2 was an electron acceptor (oxidized), thus As(III) lost electrons and changed to As(V), resulting in increase of ORP.

4.2.2 Arsenite and Asenate adsorption by Fe-BTC (Part 2.2)

Batch adsorption experiments were performed to determine adsorption capacities of As(III) and As(V) by Fe-BTC. In each experiment, 0.5 g of Fe-BTC was added to 5 mg/L As(III) and the As(V) working solutions separately. Water samples were collected over the time span of 0 - 90 minute.

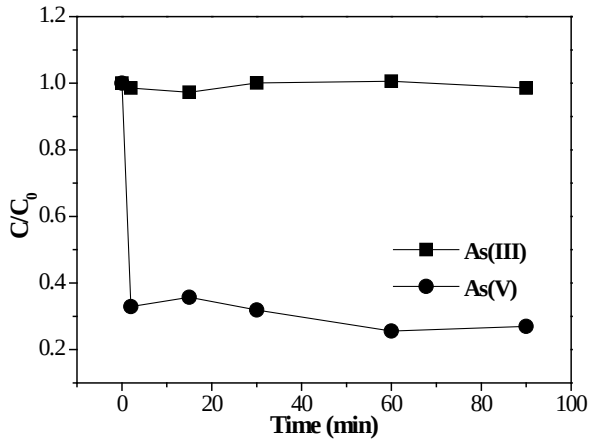

Figure 4.7 As(III) and As(V) removal by adsorption onto Fe-BTC.

Figure 4.7 presents As(III) and As(V) removal by Fe-BTC as a function of time. The results indicate that As(V) was adsorbed by Fe-BTC but not As(III). To evaluate the maximum adsorption capacity of Fe-BTC as an adsorbent to remove As(V), adsorption isotherms were compared to Langmuir and Freundlich isotherm models. Initial concentrations of As(V) was varied from 0.5 - 10 mg/L. 0.025 gram of Fe-BTC was added to 50 mL of As(V) solutions and 15 min-mixing was provide by a rotating mixer.

Table 4.1 presents Langmuir and Freundlich isotherms fitting with the experimental data. It was clear that the Langmuir model (R^2 = 0.95) provided a better fit to the adsorption data than Freundlich isotherm (R^2= 0.68). Thus, suggests the monolayer coverage of As(V) on the surface of Fe-BTC. Maximum adsorption capacity calculated from Langmuir model was 76.34 mg As(V) per g of Fe-BTC. Equilibrium parameter (R_L), calculated as $1/(1+K_LC_0)$, where C_0 is initial As(V) concentration 0.5-10 (mg/L) and K_L is the Langmuir's adsorption constant (L/mg), was used to determine whether the isotherm is unfavorable ($R_L > 1$), linear ($R_L = 1$), favorable ($0 < R_L < 1$) or irreversible ($R_L = 0$. The R_L values for As(V) adsorption by Fe-BTC were greater than zero and less than one (0.48-0.95), showing a favorable adsorption in the range of C_0 = 0.5-10 mgL^{-1} (Table 4.1).

These results illustrated the greater efficiency of Fe-BTC over other adsorbents in As(V) removal from aqueous solution.

Table 4.1 Langmuir and Freundlich isotherm constants for adsorption of As(V) by Fe-BTC.

Isotherms	Values
Langmuir	
q_{max} (mgg^{-1})	76.34
K_L (Lmg^{-1})	0.11
R_L (C_0= 0.5-10 mgL^{-1})	0.48-0.95
R^2	0.95
Freundlich	
K_F $(mgg^{-1})(Lmg^{-1})^{1/n}$	5.70
N	1.75
R^2	0.68

4.2.3 As(III) removal by combination of K-OMS2 and Fe-BTC (Part 2.3)

Based on the results from 4.2.1 – 4.2.2, processes using combination of K-OMS2 and Fe-BTC were designed in different scenarios to achieve higher performance of As(III) removal.

In Scenario 1 (Fe-BTC), As(III) was not adsorbed by Fe-BTC because of As(III) occurs predominantly as an uncharged ion (H_3AsO_3) in pH < 9 (Yazdi et al., 2007). Comparing Scenario 1 and Scenario 2 and 3 could illustrate that As(III) removal only occurred by K-OMS2.

In Scenario 2 (K-OMS2 → Fe-BTC), Fe-BTC was added to the system after reaction between As(III) and K-OMS2 reached equilibrium. 0.5 g K-OMS2 was first added to 5 mg/L of As(III) solution and the mixer was reacted with until equilibrium was reached. Then, 0.5 g of Fe-BTC was added to the solution to adsorb As(V) oxidized by K-OMS2. As shown by the results in Figure 6, the reaction reached equilibrium at 90 min in which approximately 60% of As(III) was removed. After Fe-BTC addition, the As(III) concentration decreased gradually. The total arsenite removal of Scenario 2 was 95%.

In Scenario 3 (K-OMS2 + Fe-BTC), K-OMS2 and Fe-BTC were simultaneously introduced to 5 mg/L As(III) solution. As presented in Figure 4.8, the reaction reached equilibrium after 40 min and 100% As(III) removal could be achieved.

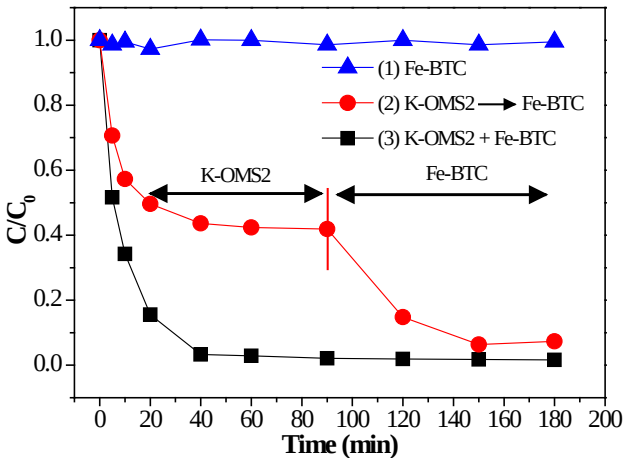

Figure 4.8 As(III) removal profile by K-OMS2 and Fe-BTC.

4.2.4 Effect of Ion species on arsenic removal (Part 2.4)

The effect of PO_4^{3-} on arsenic removal was presented in Figure 4.9. The resence of PO_4^{3-} inhibited the removal performance of arsenic significantly. Such information indicates that the

dominant dissociation species of phosphate and arsenic have similar chemistry, especially those of the phosphate and As(V). In other words, competition between arsenic species and phosphate for the same adsorption sites exists on the surface of adsorbent.

The removal of arsenic was retarded slightly in the presence of SO_4^{2-} presented in Figure 4.9. Such phenomenon was reported due to the electrical repulsion between SO_4^{2-} and arsenic species. Another reason is that the SO_4^{2-}can replace sorption side, which were adsorbed on the surface, leading to the decrease of adsorption sites available to arsenic.

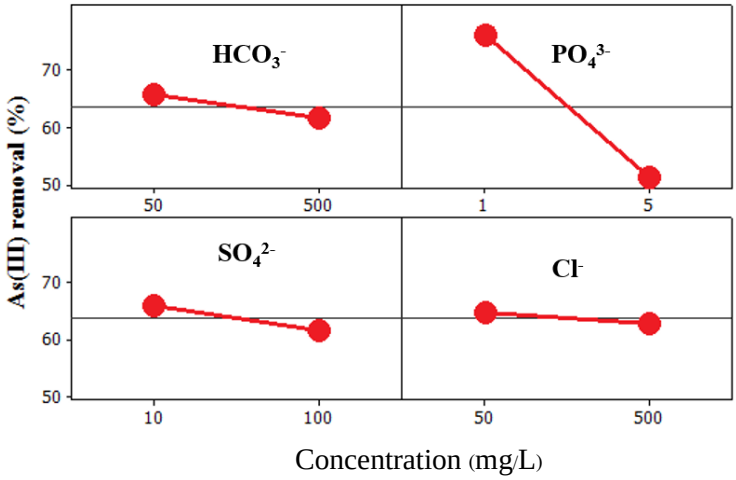

Figure 4.9 Effect of ion species on arenic removal

The effect of HCO_3^- on arsenic removal was shown in Figure 4.9. The arsenic removal was inhibited dramatically in the presence of HCO_3^-. The possible reasons may be due to competition for adsorptive sites between HCO_3^- and arsenic species since the HCO_3^- can form inner-sphere surface complexes with adsorbent surface.

In summary, among the selected species, the estimates of the inhibiting effects on the removal of arsenic are in the order as follows: $PO_4^{3-} > HCO_3^- > SO_4^{2-}$. As for the Cl^-, it plays no significant role.

4.3 Arsenic removal by CeO_2 (Part 3)

The effect of initial calcination temperature for CeO_2 synthesis on the rate of As(III) removal is shown in Figure 4.10 as a plot of dimensionless concentration versus time for calcination temperature ranging from 105 to 550 °C. Removal capacity between different calcined

products varied from 8.75, 8.94, 7.88, 8.38, and 7.59 mg/g for 105, 250, 350, 450, and 550 °C, respectively.

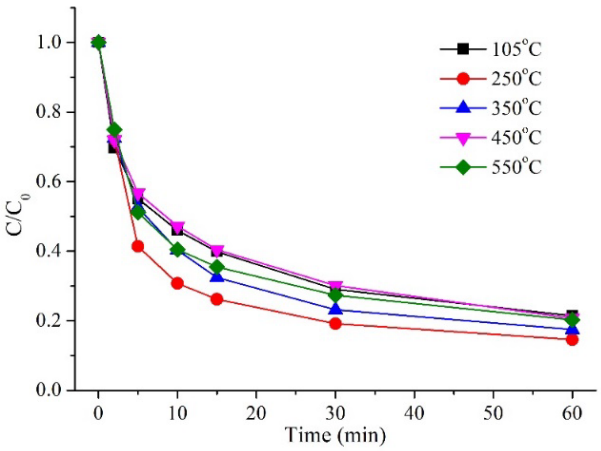

Figure 4.10 Adsorption of As(III) onto various calcined CeO_2 samples as a function of calcination temperature (°C) (experiment conditions: CeO_2 = 0.1g and As(III) = 50 mg/L).

The CeO_2 material calcined at 250 °C showed maximum removal capacity, confirming that release of residual chemisorbed water and organic residues as NO_3 (Ketzial et al., 2011) inhibited arsenic removal. Reaction by-products occurring during the CeO_2 synthesis process are shown as Eqs. (4.1)-(4.5).

$$4NaOH_{(s)} \longrightarrow 4Na^{+}_{(aq)} + 4OH^{-}_{(aq)} \quad (4.1)$$

$$Ce(NO_3)_3 \cdot 6H_2O_{(s)} \longrightarrow Ce^{3+}_{(aq)} + 3NO_3^{-}{}_{(aq)} + 6H_2O_{(aq)} \quad (4.2)$$

$$Ce^{3+}_{(aq)} + 4OH^{-}_{(aq)} + xH_2O_{(aq)} \longrightarrow Ce(OH)_4 \cdot xH_2O_{(s)} \quad (4.3)$$

$$Ce(OH)_4 \cdot xH_2O_{(s)} \longrightarrow Ce(OH)_{4(s)} + xH_2O_{(g)} \quad (4.4)$$

$$Ce(OH)_{4(g)} \xrightarrow{\text{Heating}} CeO_{2(s)} + 2H_2O_{(g)} \quad (4.5)$$

These reactions are consistent with the crystal size and surface area of CeO_2. Removal capacity of CeO_2 depends on various factors such as surface area, porosity, and surface morphology. However, the chemical characteristics of CeO_2 change on heating. The O/Ce ratio

decreased with increasing calcination temperature, while abundance of O-Ce^{3+} and hydroxyl groups also decreased at higher calcination temperature (Janos et al., 2014).

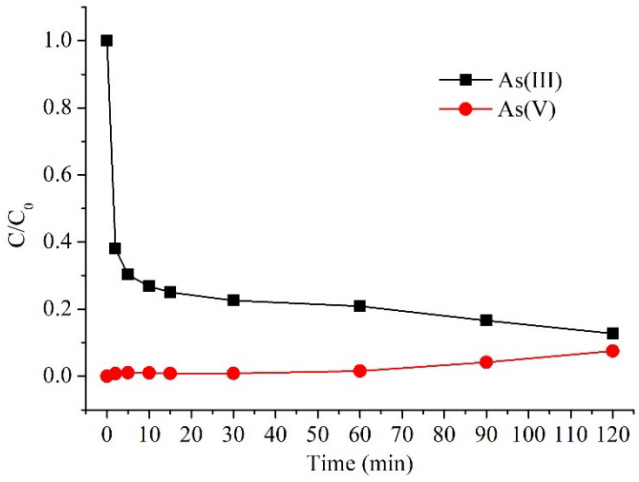

Figure 411 Relationship between contact time and residual arsenic under CeO_2 at room temperature (experimental conditions: CeO_2 = 0.5 g, As(III) = 50 mg/L, and pH = 6.14).

Calcination temperature of CeO_2 at 250 °C gave the highest removal capacity. As(III) uptake capacities were determined as a function of time to deduce an optimal contact time for adsorption of As(III) on CeO_2. Amount of As(III) on each CeO_2 sample was calculated by the difference between As(III) content in influent solution and effluent solution expressed as a percentage (C/C_0).

Variation of C/C_0 as a function of time is shown in Figure 4.10. Significantly higher arsenic removal efficiency was obtained in the first 10 min. Concentration of As(III) in aqueous solution reduced from 42.29 mg/L to 14.68 mg/L in 10 min, revealing that As(III) was quickly removed by CeO_2, and then decreased steadily with increasing reaction time. Optimal time required for CeO_2 to achieve the maximum removal efficiency (77%) was 30 min. However, As(III) began to change to As(V) at about 60 min, and this continuously increased to 120 min, indicating that CeO_2 oxidized As(III) to As(V). Additionally, As(III) in aqueous solution was partially oxidized because As(V) was detected in the As(III)-CeO_2 system as shown in Figure 4.11.

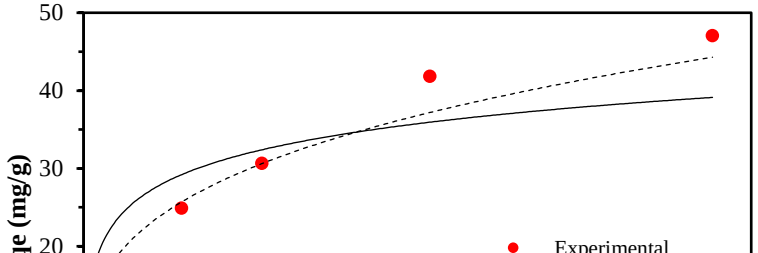

Figure 4.12 Adsorption kinetic (a), and equilibrium adsorption isotherm of As(III) (b) on CeO_2 with high equilibrium concentration (experimental conditions: CeO_2 = 0.5 g, As(III) = 50 mg/L, and pH = 6.46).

Compared to the Langmuir isotherm, the Freundlich isotherm plot resulted in a good fit with experimental data as evidenced in Figure 4.12. The Freundlich isotherm constants are shown in Table 4.3, The Freundlich isotherm fitted well for adsorption of As(III) on CeO_2. The 'n' values of As(III) were observed to be more than the value 1, indicating that adsorption was favorable for As(III) . However, the main assumption of the Freundlich model describes sorption on heterogeneous surfaces with sorption sites and heterogeneous energy distribution (Chem et al., 2018). It also describes reversible adsorption which is not restricted to the formation of a monolayer (Attari et al., 2017).

Table 4.3 Kinetics and equilibrium adsorption isotherm fitting parameters for As(III) onto CeO_2.

Adsorption kinetic (Pseudo-second-order rate kinetic)			
Initial time (min)	15	30	60
q_e (mg/g)	0.086	0.081	0.079
k_2 (g/(mg.min))	41.152	42.373	42.918
$h = k_2 q_e^2$ (mg/(g.min)	0.304	0.278	0.267
R^2	0.9989	0.9994	0.9998
Equilibrium adsorption isotherm			
Freundlich	K_F (mg/g)(L/mg)$^{1/n}$	15.909	

	n	3.414
	R^2	0.9856
	q_{max} (mg/g)	21.277
Langmuir	K_L (L/mg)	21.364
	R^2	0.8424

4.4 Remediation of Selenium (Se) contamination by nanomaterials (Part 4)

Se is competitive species for As removal. Thus, it was pre-treated to increases performance of arsenic treatment. It this study, nanoscale zero-valent iron (NZVI) was applied to treatment of Se. NZVI used for the removal of pollutants from wastewater the consequence of its well-known high specific surface area, low cost, high reactively strong reduction capacity, and fewer pollutants (Dong et al., 2016). The aggregation of NZVI affected large particle size and decreasing surface area of NZVI, resulting in decreased mobility and reactivity (Fu et al., 2015; Xi et al., 2014). The NZVI is consists of a metallic iron (Fe^0) core encapsulated by a thin oxide shell, which is related to its core-shell structure. The Fe^0 core in the NZVI oxidizes upon reaction with water and oxygen, and ultimately, the metallic iron is exhausted to form iron oxides and hydroxides cause the surface corrosion or aging properties of NZVI (Liu et al. 2015). The immobilization of NZVI on several kinds of supports has shown the capacity to inhibit further surface oxidation and improve the colloidal stability of iron nanoparticles. This research, Zeolite (Z) was used as supporter for NZVI.

Batch experiments were carried out by initially combining 15 mg/L Se^{6+} with 0.75 g Z, 0.15 g NZVI, and 0.9 g Z-NZVI. Contact time for all experiments was also observed, in which the evaluation of the initial reaction rate from 0–30 min was most effective in explaining the data. Figure 4.13 shows the applied NZVI dosage on Z. More available active sites were available for Se^{6+} rapid adsorption and reduction, resulting in a higher removal rate. Z shows that it can't remove selenium because of the electrostatic repulsion of the surface between the Z and selenium, which suggests no selenium reacted with the surface Si-O and Al-O group on Z.

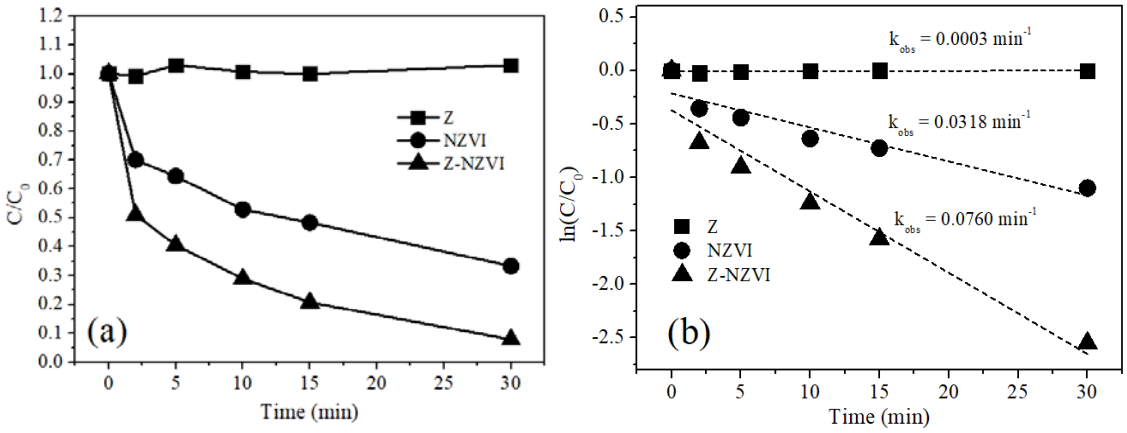

Figure 4.13 Se^{6+} removal by Z, NZVI and Z-NZVI (a) and their linearized data (b).

However, the NZVI and Z-NZVI have high removal efficiencies for selenium. There are sharply steep declines at 0–5 min with a gradual downward trend between 5–30 min. Furthermore, the lines in Figure 4.13(b) comprise the back-calculated results derived from the linearized data in Figure 4.14(a). The time-dependent removal of dissolved Se^{6+} shows a considerably higher rate of Se^{6+} removal from the aqueous solution by Z, NZVI, and Z-NZVI. The slopes of the fit linear equations yielded k_{obs} values of 0.0003, 0.0318, and 0.0760 min^{-1} for Z, NZVI, and Z-NZVI, respectively. The results showed an obvious dependence on the initial concentration of Se^{6+}.

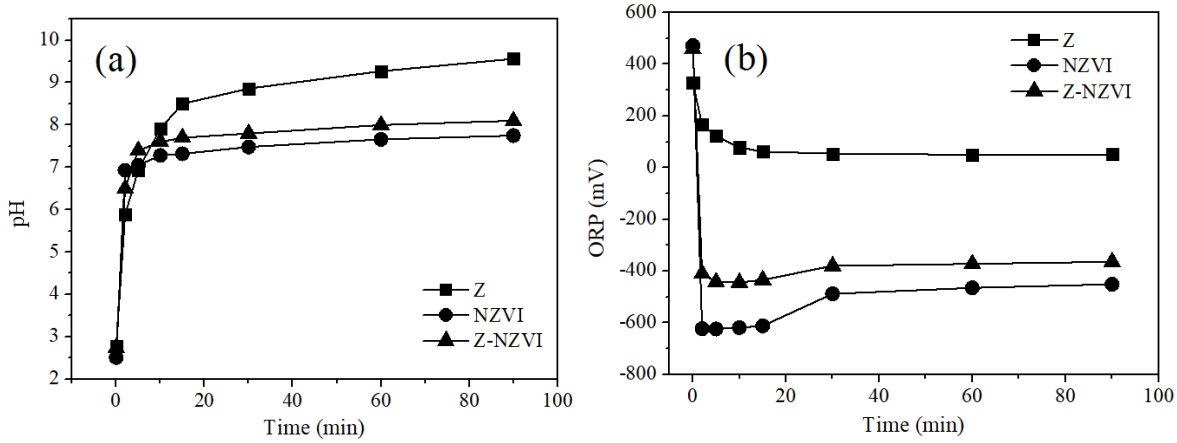

Figure 4.14 pH (a) and ORP (b) during the reaction of Se^{6+} removal by Z, NZVI, and Z-NZVI.

For the solution pH of Se^{6+} removal by Z, NZVI, and Z-NZVI, as shown in Figure 4.14(a), the solution pH increased. Decreasing concentrations of selenium would appear due to the precipitation of iron (hydr)oxides that could shield the active sites on NZVI and Z-NZVI surface and the attenuation of selenium adsorption (Liang et al, 2013). The relationship between the reaction time and ORP is shown in Figure 4.14(b). It can be concluded that the drop in ORP is necessary for Se^{6+} removal by NZVI and Z-NZVI and that the variation in ORP values is indicative of the progress of the reaction between Se^{6+} and NZVI and Z-NZVI.

4.5 Column study (Part 5)

According to previous part in a batch system, As(III) was successfully treated by using the manganese oxide octahedral molecular sieve (K-OMS2) and iron-based metal-organic framework (Fe-BTC) in powder. Although the K-OMS2 and Fe-BTC powders showed the desirable performance, they were practically inconvenient in a continuous flow system for water treatment.

4.5.1 Arsenite Oxidation over K-OMS2 (coated) in Single Continuous Fixed-Bed Column

Breakthrough curves of As(III) oxidation by K-OMS2 (coated) in single continuous fixed-bed column under different experimental conditions: I (bed length = 10 cm, flow rate = 10 mL/min), II (bed length = 15 cm, flow rate = 5 mL/min), and III (bed length = 20 cm, flow rate = 5 mL/min) are shown in Figure 4.15. They also present the breakthrough curves of total As and calculated As(V) using the equation $[As_{total}]$ = [As(III)] + [As(V)]. It was found that As(III) concentration in the effluent for all three experimental conditions had slightly released during the first 120 min with fluctuation, and then been quite stable until 600 min. Moreover, the As(III) concentration of the experimental condition I was higher than that of the experimental conditions II and III. The almost similar breakthrough of As(III) in the experimental conditions II and III meant to the undifferentiated oxidizing ability to transform As(III) to As(V) for 600 min. However, the calculated highest oxidation percentage of the experimental conditions I, II, and III were 88.51, 130.40, and 114.91% at 60, 120, and 200 min, respectively. The percentages of more than 100% may be caused by adsorption of the oxidized As(III) on the K-OMS2 (coated) as described in the former report (Phanthasri et al. 2018) and found in the XANES results in this study. After that, the oxidized As(III) was released during 120 and 200 min of experimental conditions II and III, respectively. Therefore, the mechanism that happens on the K-OMS2 (coated) surface would be oxidation-adsorption. The experimental condition II was also chosen as the most optimal condition for further study as it required the shorter bed-length concerning the amount of the K-OMS2.

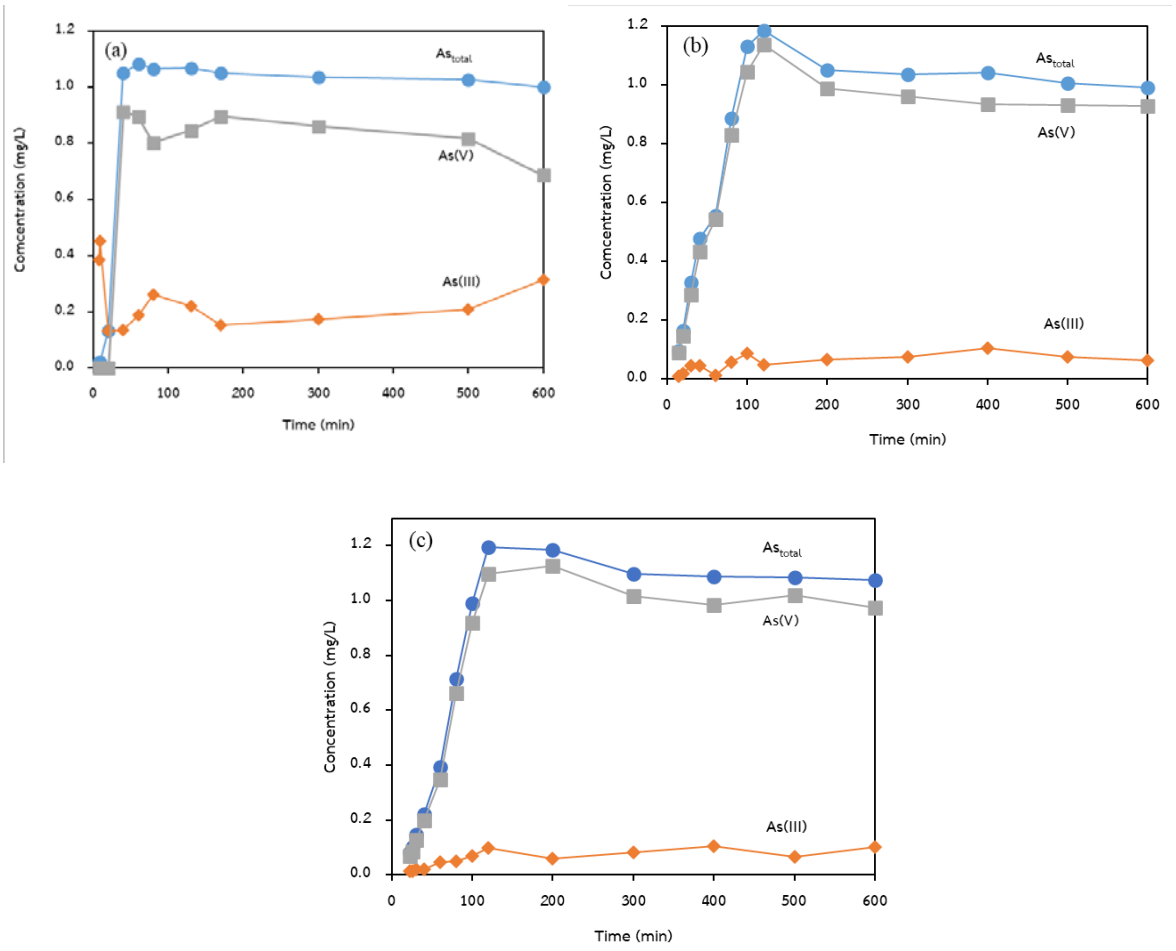

Figure 4.15 Breakthrough curve of As(III) oxidation by K-OMS2 (coated) in different experimental conditions: (a) I (bed length = 10 cm, flow rate = 10 mL/min), (b) II (bed length = 15 cm, flow rate = 5 mL/min), and (c) III (bed length = 20 cm, flow rate = 5 mL/min)

Although the oxidation-adsorption process was occurring in the K-OMS2 (coated) surface, the oxidation route was still the major mechanism of K-OMS2. Thus, the K-OMS2 (coated) was mainly considered as the oxidizing agent which be able to reuse several times. As(III) oxidation by three-round-reuse K-OMS2 (coated) in the continuous fixed-bed column under experimental condition II is presented in Figure 4.16. The appearance of the fresh and spent columns is shown in Figure 4.16(a) along with their C/C_0 versus time plots Figure 4.16(b). After three-round-reuse, the partial surface of the K-OMS2 (coated) in the column was uncovered the white surface of the

ceramic balls due to the peel-off K-OMS2, but the three-round As(III) oxidation efficiency slightly decreased according to the number of cycles but could be much undifferentiated. Therefore, it leads to conclude that the K-OMS2 (coated) column can be used repeatedly while maintaining the good and stable oxidizing efficiency of As (III) throughout the test runs in the system.

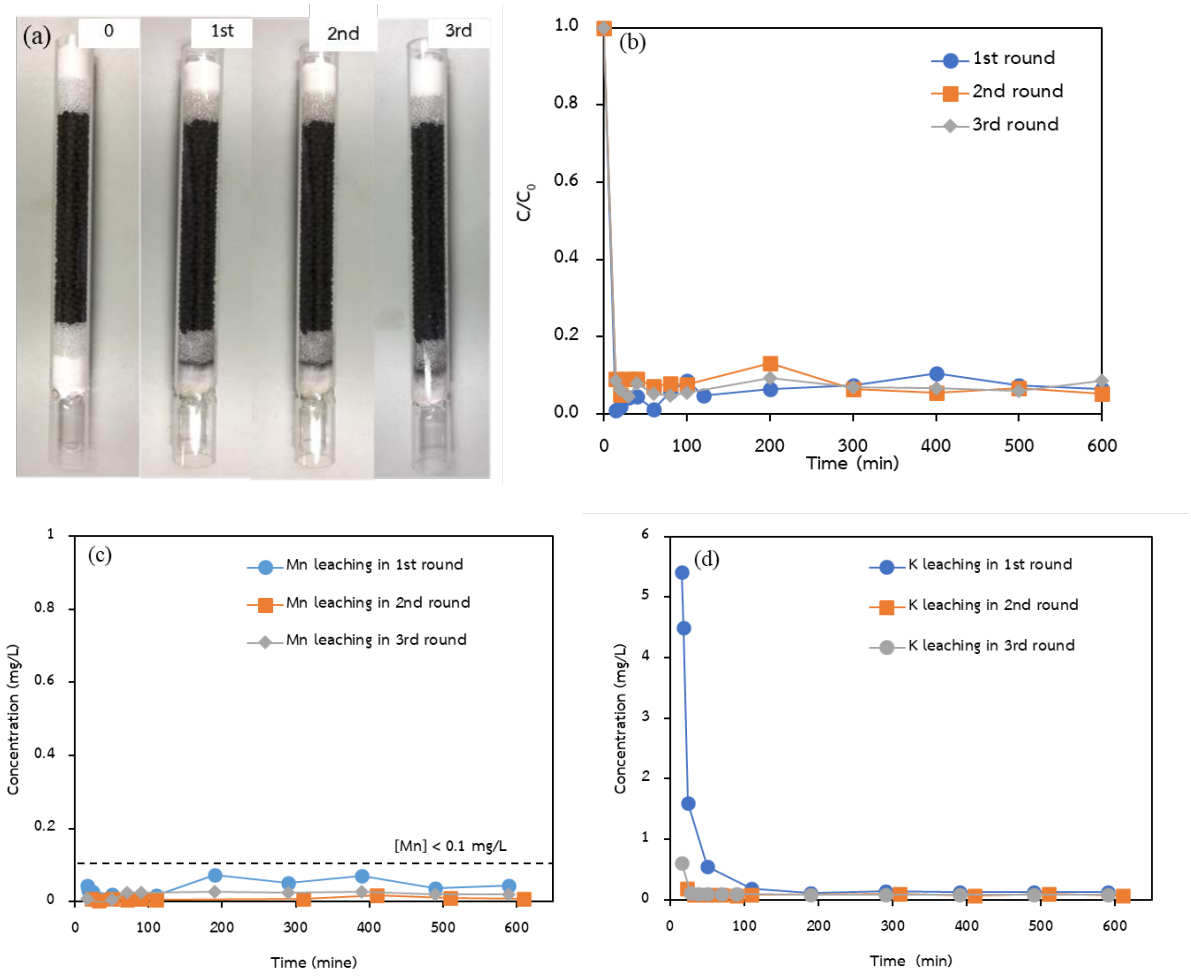

Figure 4.16 As(III) oxidation by 3-round-reuse K-OMS2 (coated) in the continuous fixed-bed column under experimental condition II: (a) appearance of the fresh and spent columns, (b) their C/C_0 curves, (c) Mn leaching, and (d) K leaching

The Mn and K leaching during the three-round As(III) oxidation over K-OMS2 (coated) in the continuous fixed-bed column under experimental condition II were also investigated. The results are presented in Figure 4.16(c)-(d). The Mn concentrations were in a range of 0.01-0.07 mg/L for the 1st round, 0.00-0.02 mg/L for the 2nd round, and 0.00-0.03 mg/L for the 3rd round. The Mn leaching concentration from the 2nd and the 3rd round was likely consistent and lower

than the one from the 1st round. The Mn leaching concentration was also lower than the WHO drinking water standard which is set at below 0.1 mg/L (World Health Organization 2017). For the K leaching, its concentration was quite high for the 1st round especially during the first 110 min with a range of 0.55-5.42 mg/L. The K leaching concentration was then low and stable even if in the 2nd and the 3rd round of reuse the K-OMS2 (coated) column. However, The high concentration of K leaching was probably due to the position of K in the K-OMS2 chemical structure. K is in the cavity with a weak bond compared to the Mn exists by the covalent bond between Mn and O which is stronger (Sriskandakumar et al. 2009; Wang et al. 2015).

4.5.2 Arsenate Adsorption over Fe-BTC (coated) in Single Continuous Fixed-Bed Column

As(V) adsorption by Fe-BTC (coated) in the continuous fixed-bed column (a) breakthrough curve under experimental conditions: I (bed length = 10 cm, flow rate = 10 mL/min), II (bed length = 15 cm, flow rate = 5 mL/min), and III (bed length = 20 cm, flow rate = 5 mL/min) is shown in Figure 6. The experimental condition I gave the breakthrough curve with a steeper slope than the experimental conditions II and III. In Figure 6(b)-(d), the Fe-BTC (coated) column was able to adsorb As(V) and control the effluent concentration lower than 0.01 mg/L which is the As in drinking water standards by WHO (Mar Wai et al. 2019). The breakthrough capacity was found at 1.16, 0.31, and 0.28 mg/g within the first 40, 30, and 40 min for the experimental conditions I, II, and III, respectively.

Thomas model and Yoon-Nelson model were used to explicate the kinetic adsorption and estimate breakthrough curves in the column. The obtained equation from the suitable model can be used further for illustrating the fixed-bed column behavior and scaling up the treatment system for industrial applications. The calculation results obtained from applying the linear equation of the Thomas model and the Yoon-Nelson model present in Table 4.4. It was found that the standard deviation (S.D.) obtained from the Yoon-Nelson model was lower than the ones from the Thomas model for all experimental conditions. The Yoon-Nelson model was thus appropriately used for adsorption behavior explanation as well as a simulation in the case of the Fe-BTC (coated) column in this study, which meant that the rate of adsorption decreases relies on the proportional of adsorbate breakthrough on the adsorbents (Luekittisup et al. 2015; Yagub et al. 2015). Moreover, for both models, the experimental condition I gave the highest square of

the correlation (R^2) of 0.9206, but the highest maximum adsorption capacity (q_0) was under the experimental condition II. Therefore, the As(V) adsorption over the Fe-BTC (coated) under experimental condition II relying on the Yoon-Nelson model was used further for Fe leaching from one-round-use of Fe-BTC (coated) column, as shown in Figure 4.17, being in the range of 0.0.7—0.20 mg/L and the combined continuous fixed-bed columns study.

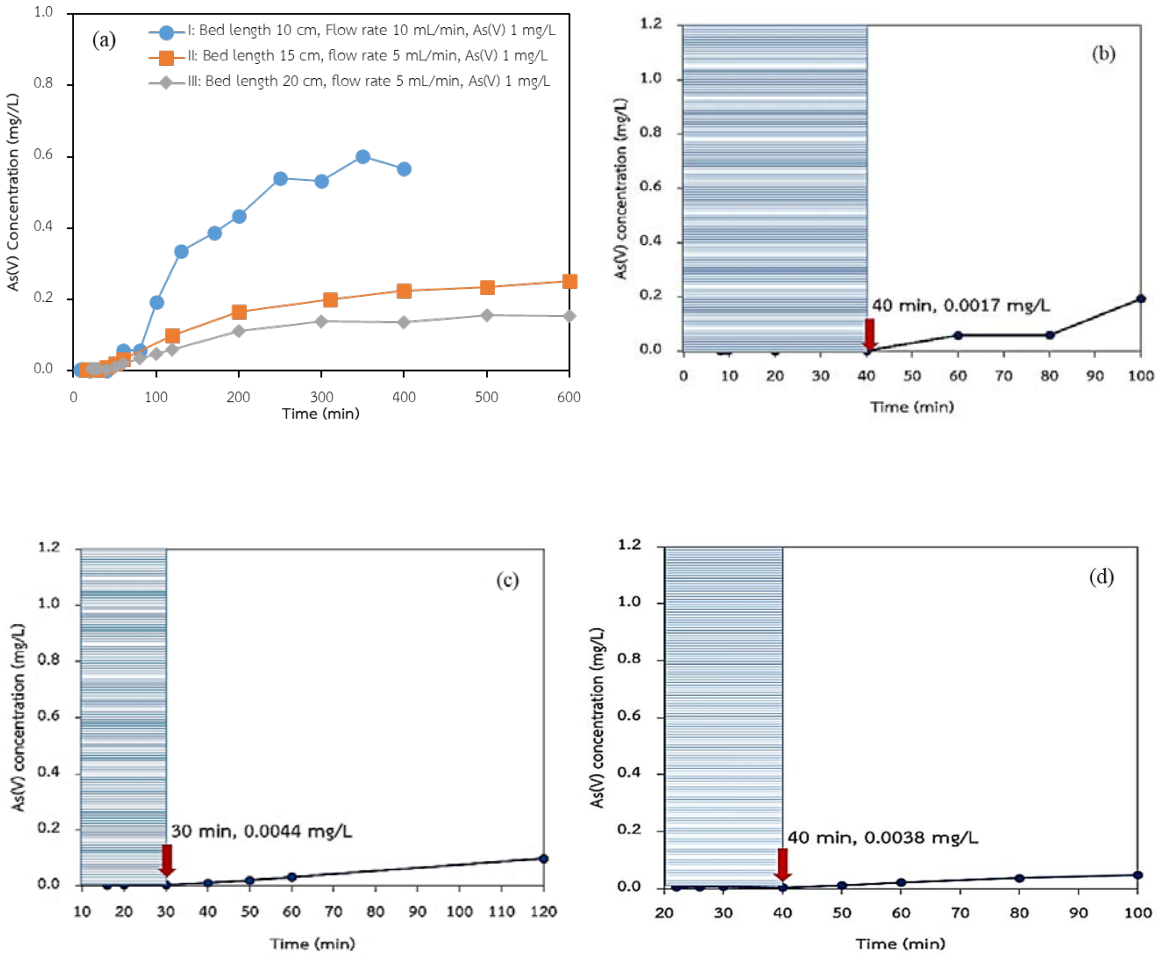

Figure 4.17. As(V) adsorption by Fe-BTC (coated) in the continuous fixed-bed column (a) breakthrough curve, and breakthrough capacity under experimental conditions: (b) I (bed length = 10 cm, flow rate = 10 mL/min), (c) II (bed length = 15 cm, flow rate = 5 mL/min), and (d) III (bed length = 20 cm, flow rate = 5 mL/min)

Table 4.4 Rate constants and As(V) adsorbed by Fe-BTC (coated) obtained from Thomas model and Yoon-Nelson model

Experimental condition	Thomas model				Yoon-Nelson model				
	K_T (mL/min/mg)	q_0 (mg/g)	S.D. (%)	R^2	K_{YN} (1/min)	τ (min)	q_0 (mg/g)	S.D. (%)	R^2
I	0.0051	11.97	13.66	0.9206	0.0063	393.46	11.40	1.61	0. 920 6
II	0.0003	60.12	30.67	0.8704	0.0004	5,081.25	52.60	6.22	0. 870 4
III	0.0003	49.01	13.66	0.7990	0.0004	6,185.75	42.89	1.60	0. 799 0

Chapter 5

Conclusion

To enhance the performance of total arsenic removal, a combination of oxidation and adsorption processes were proposed. The K-OMS2 (coated) was used for oxidation of As(III) to As(V), while the transformed As(V) was adsorbed on the Fe-BTC (coated). In the part of the continuous fixed-bed column study, the K-OMS2 (coated) column showed that the operating maintained stable after 120 min and highly oxidize As(III) to As(V) during 600 min of the test run. Moreover, the XANES results revealed that the partial As(V) can be adsorbed on the K-OMS2 surface which may cause the loss of its active sites. Also, the K-OMS2 (coated) column can be reused at least for three cycles, in which oxidizing capacity is slightly decreased according to the number of cycles with very low Mn and K leaching. In the instance of the Fe-BTC column, As(V) was highly adsorbed by Fe-BTC (coated), and Fe leaching was quite low. The experimental data fitted well with Yoon-Nelson Model with a maximum adsorption capacity of 52.60 mg/g (R^2 = 0.8704 and S.D. = 6.22). With the K-OMS2 (coated) and Fe-BTC (coated) continuous fixed-bed columns combined under the optimal experimental conditions, the total As(III) was removed for

more than 60% throughout 2,200 min of the test run. The coating technique of K-OMS2 and Fe-BTC in this study was concluded to have the potential to practically apply in an upscaled As treatment approach.

In part of arsenic removal by CeO_2, the results revealed that Ceria calcined at 250 °C showed maximum adsorption capacities of As(III) reaching 21.27 mg/g. The adsorption behavior of As(III) was well fitted to the Freundlich isotherm and a pseudo-second-order model. The As(III) adsorption mechanisms as complexation were conducted between hydroxyl groups and redox transformation between As(III) and CeO_2. For pre-treatment of Se, this study demonstrated that Se^{6+} could be effectively removed by Z-NZVI. The batch experiments indicated that Z-NZVI had more active sites available for Se^{6+} rapid reduction and sorption, resulting in higher removal kinetic rate. The results of this study suggest that enhanced Se^{6+} removal by Z-NZVI is highly effective as a perceived mechanism.

References

Alomar, M. K., Alsaadi, M. A., Hayyan, M., Akib, S., & Hashim, M. A. (2016). Functionalization of CNTs surface with phosphonuim based deep eutectic solvents for arsenic removal from water. Applied Surface Science, 389, 216–226.

Arkabanee Mukherjee, M. Kundu, B. Basu, B. Sinha, M. Chatterjee, M. Das Bairagya, U.K. Singh, S. Sarkar. (2017). Arsenic load in rice ecosystem and its mitigation through deficit irrigation. Journal of Environmental Management 197, 89-95.

Arii, T., Taguchi, T.,Kishi, A., Ogawa, M., Sawada, Y. (2002). Thermal decomposition of cerium (III) acetate studied with sample-controlled thermogravimetric-mass spectrometry (SCTG-MS), J. Eur. Ceram. Soc., 22, 2283-2289.

Atribak, I., Bueno-López, A., García-García, A., Navarro, P., Frías, D., & Montes, M. (2010). Catalytic activity for soot combustion of birnessite and cryptomelane. Applied Catalysis B: Environmental, 93(3), 267–273.

Attari, M., Bukhari, S.S., Kazemian, H., Rohani, S. (2017). A low-cost adsorbent from coal fly ash for mercury removal from industrial wastewater, J. Environ. Chem. Eng., 5, 391–399.

Autie-Castro, G., Autie, M. A., Rodríguez-Castellón, E., Aguirre, C., & Reguera, E. (2015). Cu-BTC and Fe- BTC metal- organic frameworks: Role of the materials structural features on their performance for volatile hydrocarbons separation. Colloids and Surfaces A: Physicochemical and Engineering Aspects, 481, 351–357.

Bissen, M., Vieillard-Baron, M.-M., Schindelin, A. J., & Frimmel, F. H. (2001). TiO_2-catalyzed photooxidation of arsenite to arsenate in aqueous samples. Chemosphere, 44(4), 751–757.

Chen, C., Zhang, M., Guan, Q., & Li, W. (2012). Kinetic and thermodynamic studies on the adsorption of xylenol orange onto MIL-101(Cr). Chemical Engineering Journal, 183, 60–67.

Chen, J., Wang, J., Zhang, G., Wu, Q., Wang, D. (2018). Facile fabrication of nanostructured cerium-manganese binary oxide for enhanced arsenite removal from water, Chem. Eng. J., 334,1518-1526.

Clifford, D. A., Ghurye, G., & Tripp, A. R. (1999). Development of anion exchange process for arsenic removal from drinking water. In: Arsenic exposure and health effects. Elsevier, New York, 379–388.

Dey, C., Kundu, T., Biswal, B. P., Mallick, A., & Banerjee, R. (2014). Crystalline metal-Organic frameworks (MOFs): Synthesis, structure and function. Acta Crystallographica Section B: Structural Science, Crystal Engineering and Materials, 70(1), 3–10.

Dhakshinamoorthy, A., Alvaro, M., Chevreau, H., Horcajada, P., Devic, T., Serre, C., ... Férey, G. (2012). Iron(iii) metal–organic frameworks as solid Lewis acids for the isomerization of α-pinene oxide. Catal. Sci. Technol., 2(2), 324–330.

Dharmarathna, S., King'ondu, C. K., Pahalagedara, L., Kuo, C.-H., Zhang, Y., & Suib, S. L. (2014). Manganese octahedral molecular sieve (OMS-2) catalysts for selective aerobic oxidation of thiols to disulfides. Applied Catalysis B: Environmental, 147, 124–131.

Dong, H., Chen, Y., Sheng, G., Li, J., Cao, J., Li, Z., Li, Y. (2016). The roles of a pillared bentonite on enhancing Se(VI) removal by ZVI and the influence of co-existing solutes in groundwater. *Journal of Hazardous Materials*, 304, 306–312.

Duan, L., Sun, B., Wei, M., Luo, S., Pan, F., Xu, A., & Li, X. (2015). Catalytic degradation of Acid Orange 7 by manganese oxide octahedral molecular sieves with peroxymonosulfate under visible light irradiation. Journal of Hazardous Materials, 285, 356–365.

El-Sawy, A. M., King'ondu, C. K., Kuo, C.-H., Kriz, D. A., Guild, C. J., Meng, Y., ... Suib, S. L. (2014). X-ray Absorption Spectroscopic Study of a Highly Thermally Stable Manganese Oxide Octahedral Molecular Sieve (OMS- 2) with High Oxygen Reduction Reaction Activity. Chemistry of Materials, 26(19), 5752–5760.

Fordyce, F. M. (1995). Hydrogeochemistry of arsenic in an area of chronic mining-related arsenism, Ron Phibun District, Nakhon Si Thammarat Province, Thailand: preliminary results. BGS Technical Report WC/94/79R.

Fu, Y., Wang, J., Liu, Q., Zeng, H. (2014). Water-dispersible magnetic nanoparticle-graphene oxide composites for selenium removal. *Carbon*, 77, 710–721.

Gandhe, A. R., Rebello, J. S., Figueiredo, J. L., & Fernandes, J. B. (2007). Manganese oxide OMS-2 as an effective catalyst for total oxidation of ethyl acetate. Applied Catalysis B: Environmental, 72(1–2), 129–135.

García, E., Medina, R., Lozano, M., Hernández Pérez, I., Valero, M., & Franco, A. (2014). Adsorption of Azo-Dye Orange II from Aqueous Solutions Using a Metal-Organic Framework Material: Iron- Benzenetricarboxylate. Materials, 7(12), 8037–8057.

Gibson, B. D., Blowes, D. W., Lindsay, M. B. J., Ptacek, C. J. (2012). Mechanistic investigations of Se(VI) treatment in anoxic groundwater using granular iron and organic carbon: An EXAFS study. *Journal of Hazardous Materials*, 241–242, 92–100.

Gonzalez, C. M., Hernandez, J., Parsons, J. G., Gardea-Torresdey, J. L. (2010). A study of the removal of selenite and selenate from aqueous solutions using a magnetic iron/manganese oxide nanomaterial and ICP-MS. *Microchemical Journal*, 96(2), 324–329.

Hall, K. R., Eagleton, L. C., Acrivos, A., & Vermeulen, T. (1966). Pore- and Solid-Diffusion Kinetics in Fixed-Bed Adsorption under Constant-Pattern Conditions. Industrial & Engineering Chemistry Fundamentals, 5(2), 212–223.

Hou, J., Liu, L., Li, Y., Mao, M., Lv, H., & Zhao, X. (2013). Tuning the K + Concentration in the Tunnel of OMS - 2 Nanorods Leads to a Signi fi cant Enhancement of the Catalytic Activity for Benzene Oxidation.

Janos, P., Kuran, P., Kormunda, M., Stengl, V., Grygar, T.M., Dosek, M., Stastny, M., Ederer, J.,. Pilarova, V., Vrtoch, L. (2014). Cerium dioxide as a new reactive sorbent for fast degradation of parathion methyl and some other organophosphates, J. Rare Earths., 32, 360-370.

Jegadeesan, G. B., Mondal, K., Lalvani, S. B. (2015). Adsorption of Se (IV) and Se (VI) Using Copper-Impregnated Activated Carbon and Fly Ash-Extracted Char Carbon. *Water, Air, and Soil Pollution*, 226(8).

Ketzial J., Nesaraj A. (2011). Synthesis of CeO_2 nanoparticles by chemical precipitation and the effect of a surfactant on the distribution of particle sizes, J. Ceram. Process. Res., 12, 74-79.

Kim, M.-J., & Nriagu, J. (2000). Oxidation of arsenite in groundwater using ozone and oxygen. Science of The Total Environment, 247(1), 71–79.

Kim, S. C., & Shim, W. G. (2010). Catalytic combustion of VOCs over a series of manganese oxide catalysts. Applied Catalysis B: Environmental, 98(3–4), 180–185.

Lackovic, J. A., Nikolaidis, N. P., & Dobbs, G. M. (2000). Inorganic arsenic removal by zero-valent iron. E*nvironmental engineering science*, 17, 29–40.

Langmuir, I. (1916). the Constitution and Fundamental Properties of Solids and Liquids. Part I. Solids. Journal of the American Chemical Society, 252, 2221–2295.

Lee, Y., Kim, J., & Ahn, W. (2013). Synthesis of metal-organic frameworks : A mini review, 30(9), 1667–1680.

Lee, Y. R., Kim, J., & Ahn, W. S. (2013). Synthesis of metal-organic frameworks: A mini review. Korean Journal of Chemical Engineering, 30(9), 1667–1680.

Li, J., Sculley, J., & Zhou, H. (2012). Metal À Organic Frameworks for Separations, 869–932.

Li, R., Li, Q., Gao, S., Ku, J., (2012). Exceptional arsenic adsorption performance of hydrous cerium oxide nanoparticles : Part A . Adsorption capacity and mechanism, Chem. Eng. J., 186, 127–135.

Liu, A., Liu, J., Zhang, W.x. (2015). Transformation and composition evolution of nanoscale zero valent iron (nZVI) synthesized by borohydride reduction in static water. *Chemosphere*, 119, 1068–1074.

Luekittisup, P., Tanboonchauy, V., Chumee, J., Predapitakkun, S., Kiatkomol, R.W. & Grisdanurak, N. (2015). Removal of chlorinated chemicals in H_2 feedstock using modified activated carbon. *Journal of Chemistry,* 1-9.

Millanar, J. M., Yodsa-nga, A., Khemthong, P., & Daniel, M. (2013). Novel K-OMS-2 Synthesis by Uncalcined Route. 3rd TIChE Int. Conf. 2013, Khon Kaen, 169–173.

Mohan, D., & Pittman, C. U. (2007). Arsenic removal from water/wastewater using adsorbents—A critical review. Journal of Hazardous Materials, 142(1), 1–53.

Mukherjee, A., Wang, Z., Kinlough, C. L., Poland, P. A., Marciszyn, A. L., Montalbetti, N., … Hughey, R. P. (2017). Specific Palmitoyltransferases Associate with and Activate the Epithelial Sodium Channel *, 292(10), 4152–4163.

Nandasiri, M. I., Jambovane, S. R., McGrail, B. P., Schaef, H. T., & Nune, S. K. (2016). Adsorption, separation, and catalytic properties of densified metal-organic frameworks. Coordination Chemistry Reviews, 311, 38–52.

Pettine, M., Campanella, L., & Millero, F. J. (1999a). Arsenite oxidation by H_2O_2 in aqueous solutions. Geochimica et Cosmochimica Acta, 63(18), 2727–2735.

Qi, J., Zhang, G., & Li, H. (2015). Efficient removal of arsenic from water using a granular adsorbent: Fe–Mn binary oxide impregnated chitosan bead. Bioresource Technology, 193, 243–249.

Qiu, G., Huang, H., Dharmarathna, S., Benbow, E., Stafford, L., & Suib, S. L. (2011). Hydrothermal Synthesis of Manganese Oxide Nanomaterials and Their Catalytic and Electrochemical Properties. Chemistry of Materials, 23(17), 3892–3901.

Ramesh, K., Chen, L., Chen, F., Liu, Y., Wang, Z., & Han, Y. F. (2008). Re-investigating the CO oxidation mechanism over unsupported MnO, Mn_2O_3 and MnO_2 catalysts. Catalysis Today, 131(1–4), 477–482.

Rice RH, Mauro TM. Toxic Responses of the Skin. In: Klaassen CD, Watkins III JB. eds. Casarett & Doull' s Essentials of Toxicology, 3e New York, NY: McGraw- Hill; . http://accesspharmacy.mhmedical.com/Content.aspx?bookid=1540&sectionid=92527338. Accessed July 10, 2017.

Saleem H., Rafique U., Davies R.P. (2016). Investigations on post-synthetically modified UiO-66-NH2 for the adsorptive removal of heavy metal ions from aqueous solution. Microporous Mesoporous Mater, 221, 238–244.

Salman Shahid, K. N. (2014). Performance and plasticization behavior of polymer – MOF membranes for gas separation at elevated pressures. Journal of Membrane Science, 470(November), 166–177.

Santos, V. P., Carabineiro, S. A. C., Bakker, J. J. W., Soares, O. S. G. P., Chen, X., Pereira, M. F. R., … Kapteijn, F. (2014). Stabilized gold on cerium-modified cryptomelane : Highly active in low-temperature CO oxidation. Journal of Catalysis, 309, 58–65.

Schurz, F., Bauchert, J. M., Merker, T., Schleid, T., Hasse, H., & Gläser, R. (2009). Octahedral molecular sieves of the type K-OMS-2 with different particle sizes and morphologies: Impact on the catalytic properties in the aerobic partial oxidation of benzyl alcohol. Applied Catalysis A: General, 355(1–2), 42–49.

Sciortino, L., Alessi, A., Messina, F., Buscarino, G., & Gelardi, F. M. (2015). on the Local Environment Study, 1–5.

Shahid, S., & Nijmeijer, K. (2014). High pressure gas separation performance of mixed-matrix polymer membranes containing mesoporous Fe(BTC). Journal of Membrane Science, 459, 33–44.

Sharma, V. K., & Sohn, M. (2009). Aquatic arsenic: toxicity, speciation, transformations, and remediation. Environment International, 35(4), 743–59.

Sriskandakumar, T., Opembe, N., Chen, C.H., Morey, A., King'Ondu, C. & Suib, S.L. (2009). Green decomposition of organic dyes using octahedral molecular sieve manganese oxide catalysts. *The Journal of Physical Chemistry A* 113(8): 1523-1530.

Tian, H., He, J., Liu, L., Wang, D., Hao, Z., & Ma, C. (2012). Microporous and Mesoporous Materials Highly active manganese oxide catalysts for low-temperature oxidation of formaldehyde. Microporous and Mesoporous Materials, 151, 397–402.

Topologies, M. O. F., Stock, N., & Biswas, S. (2012). Synthesis of Metal-Organic Frameworks (MOFs) : Routes to Various, 933–969.

Triszcz, J. M., Porta, A., & Einschlag, F. S. G. (2009). Effect of operating conditions on iron corrosion rates in zero-valent iron systems for arsenic removal. *Chemical Engineering Journal*, 150, 431–439.

U.S. EPA. (2000). Technologies and costs for removal of arsenic from drinking water. EPA-815-R-00-028, Office of Water, U.S. Environmental Protection Agency, Washington, DC.

Van de Voorde, B., Bueken, B., Denayer, J., & De Vos, D. (2014). Adsorptive separation on metal–organic frameworks in the liquid phase. Chem. Soc. Rev., 43(16), 5766–5788.

Veličković, Z., Vuković, G. D., Marinković, A. D., Moldovan, M.-S., Perić-Grujić, A. A., Uskoković, P. S., & Ristić, M. Đ. (2012). Adsorption of arsenate on iron(III) oxide coated ethylenediamine functionalized multiwall carbon nanotubes. Chemical Engineering Journal, 181, 174–181.

Wang, F., Dai, H., Deng, J., Bai, G., Ji, K., & Liu, Y. (2012). Manganese Oxides with Rod-, Wire-, Tube-, and Flower-Like Morphologies: Highly Effective Catalysts for the Removal of Toluene.

Wang, Y., Ye, G.Q., Chen, H.H., Hu, X.Y., Niu, Z., Ma, S.Q. (2015). Functionalized metal–organic framework as a new platform for efficient and selective removal of cadmium(II) from aqueous solution. J. Mater. Chem. A 3, 15292–15298.

World Health Organization. (2017). *Guidelines for drinking-water quality: fourth edition incorporating the first addendum*

Xi, Y., Sun, Z., Hreid, T., Ayoko, G. A., Frost, R. L. (2014). Bisphenol A degradation enhanced by air bubbles via advanced oxidation using in situ generated ferrous ions from nano zero-valent iron/palygorskite composite materials. *Chemical Engineering Journal*, 247, 66–74.

Yagub, M.T., Sen, T.K., Afroze, S. & Ang, H.M. (2015). Fixed-bed dynamic column adsorption study of methylene blue (MB) onto pine cone. *Desalination and Water Treatment* 55(4): 1026-1039.

Yamani, J. S., Lounsbury, A. W., Zimmerman, J. B. (2014). Adsorption of selenite and selenate by nanocrystalline aluminum oxide, neat and impregnated in chitosan beads. *Water Research*, 50, 373–381.

Yamashita, T., & Vannice, A. (1997). Temperature-programmed desorption of NO adsorbed on Mn203 and Mn304, 13, 141–155.

Yazdi M., Darban A., (2007). Effect of Arsenic Speciation on Remediation of Arsenic-Contaminated Soils and Waters', 1–4.

Yodsa-nga, A., Millanar, J. M., Neramittagapong, A., Khemthong, P., & Wantala, K. (2015). Surface & Coatings Technology Effect of manganese oxidative species in as-synthesized K-OMS 2 on the oxidation of benzene. Surface & Coatings Technology, 271, 217–224.

Yu, Y., Zhang, C., Yang, L., Chen J.P. (2016). Cerium oxide modified activated carbon as an efficient and effective adsorbent for the rapid uptake of arsenate and arsenite: material development and study of performance and mechanisms, Chem. Eng. J., 315, 630-638.

Zhu, B.-J., Yu, X.-Y., Jia, Y., Peng, F.-M., Sun, B., Zhang, M.-Y., Huang, X.-J. (2012). Iron and 1,3,5-Benzenetricarboxylic Metal– Organic Coordination Polymers Prepared by Solvothermal Method and Their Application in Efficient As(V) Removal from Aqueous Solutions. The Journal of Physical Chemistry C, 116(15), 8601–8607.

Research Output

1. Publications

1.1. Accepted manuscript:

Phanthasri J. , Grisdanurak N. , Khamdahsag P. , Wantala K. ,Khunphonoi R. , Wannapaiboon S., **Tanboonchuy V.***. Role of Zeolite-Supported Nanoscale Zero-Valent Iron in Selenate Removal. *Water Air Soil Pollut* (2020), 231: 199.

- SCI data base, Q2, Impact factor 1.774

1.2 Revised Manuscript re-submission **(with Minor Revision, under review)**

Suwannatraia S. , Yan D. , Phanthasri J. , Khamdahsag P. , Wannapaiboon S. , **Tanboonchuy V.***. Oxidation-adsorption of arsenite contaminated water over ceria nanorods. *Desalination and water treatment* (2020).

- SCI data base Q3, impact factor 1.234

1.3 Submitted Manuscript **(Under Review)**

Poompang P., Supannafai N., Phanthasri J., Khamdahsag P., **Tanboonchuy V.*** Continuous fixed-bed column studies of arsenite removal via oxioxidation and adsorption co-processes. *Chemical Engineering Journal* (2020).

- SCI data base Q1, impact factor 8.355

2. Technology Transfer (Keynote Speaker)

Keynote Speaker: **Title** Nanomaterials: The way to save our environment.

2019 Internation Conference on Information Technology and Applied Scinces,

22 October 2018, The Chai Nan University of Pharmacy and Science.

Tainan, Taiwan.

APPENDICES

APPENDIX A Published Manuscript

APPENDIX B Re-Submitted Manuscript (Minor Revision, under review)

APPENDIX C Submitted Manuscript (under review)

APPENDIX D Invitation Letter for Keynote Speaker

APPENDIX A

Published Manuscript

- **Authors:** Phanthasri J. , Grisdanurak N. , Khamdahsag P. , Wantala K. ,Khunphonoi R. , Wannapaiboon S., **Tanboonchuy V.***
- **Title:** Role of Zeolite-Supported Nanoscale Zero-Valent Iron in Selenate Removal
- **Journal:** Water Air Soil Pollut (2020), 231: 199.
  (SCIE, Q2, Impact factor 1.774)

APPENDIX B

Re-Submitted Manuscript (Minor Revision, under review)

- **Authors:** Suwannatraia S., Yan D., Phanthasri J., Khamdahsag P., Wannapaiboon S., **Tanboonchuy V.***
- **Title:** Oxidation-adsorption of arsenite contaminated water over ceria nanorods
- **Journal:** Desalination and water treatment
  (SCIE data base Q3, impact factor 1.234)

APPENDIX C

Submitted Manuscript (Minor Revision, under review)

- **Authors:** Poompang P., Supannafai N., Phanthasri J., Khamdahsag P., **Tanboonchuy V.**
- **Title:** Continuous fixed-bed column studies of arsenite removal via oxioxidation and adsorption co-processes
- **Journal:** Chemical Engineering Journal
  (SCI data base Q1, impact factor 8.355)

APPENDIX D

Keynote Speaker

- 2019 International Conference on Information Technology and Applied Sciences
- 22 October 2018
- Title: Nanomaterials: The way to save our environment
- Venue: The Chai Nan University of Pharmacy and Science. Tainan, Taiwan

Water Air Soil Pollut (2020) 231:199
https://doi.org/10.1007/s11270-020-04587-x

Role of Zeolite-Supported Nanoscale Zero-Valent Iron in Selenate Removal

Jakkapop Phanthasri · Nurak Grisdanurak · Pummarin Khamdahsag · Kitirote Wantala · Rattabal Khunphonoi · Suttipong Wannapaiboon · Visanu Tanboonchuy

Received: 10 December 2019 / Accepted: 8 April 2020

Abstract Nanoscale zero-valent iron–supported zeolite Na-P1 (Z-NZVI) was synthesized and technologically promoted for selenate (Se^{6+}) removal from water. NZVI, Z, and Z-NZVI were characterized using XRD, FTIR, high-resolution transmission electron microscopy with energy-dispersive X-ray spectroscopy (HR-TEM-EDS), and XANES techniques. Morphology and visualizing analysis using HR-TEM-EDS demonstrated that NZVI was uniformly distributed on the surfaces of Z in the Z-NZVI sample, which apparently reduced the aggregation of NZVI and would thereby increase the reduction activity. The Z-NZVI demonstrated higher efficiency for Se^{6+} removal since the high synergistic effect of Se^{6+} reduction and sorption by Z-NZVI. XANES analysis indicated that Z-NZVI could enhance Se^{6+} reduction into and selenium (Se^{0}), while the adsorption phenomenon emerged on the Z-NZVI surface. Z performed as a supporter of the insoluble products, improving the reduction activity of NZVI. The high capacity of Z-NZVI provides promising technology for the removal of selenium from aqueous solutions.

Keywords Selenate · Selenium · Fly ash · Zeolite · Nanoscale zero-valent iron

J. Phanthasri · R. Khunphonoi · V. Tanboonchuy
Department of Environmental Engineering, Faculty of Engineering, Khon Kaen University, Khon Kaen 40002, Thailand

N. Grisdanurak
Department of Chemical Engineering, Faculty of Engineering, Thammasat University, Khlong Luang District, Pathumthani 12121, Thailand

N. Grisdanurak
Center of Excellence in Environmental Catalysis and Adsorption, Faculty of Engineering, Thammasat University, Khlong Luang District, Pathumthani 12121, Thailand

P. Khamdahsag
Environmental Research Institute, Chulalongkorn University, Bangkok 10330, Thailand

K. Wantala
Department of Chemical Engineering, Faculty of Engineering, Khon Kaen University, Khon Kaen 40002, Thailand

K. Wantala · R. Khunphonoi · V. Tanboonchuy (✉)
Research Center for Environmental and Hazardous Substance Management (EHSM), Khon Kaen University, Khon Kaen 40002, Thailand
e-mail: visanu@kku.ac.th

S. Wannapaiboon
Synchrotron Light Research Institute (Public Organization), Nakhon Ratchasima 30000, Thailand

1 Introduction

Selenium is an essential nutrient element for life in trace amounts, but it is extremely toxic at higher concentrations. Selenium concentrations in water environments have increased, not only in natural resources but also from anthropogenic practices such as coal-fired power plants, agricultural irrigation drainage, the combustion of fossil fuels, and mining operations (Gonzalez et al., 2010). Selenium has the narrowest range of dietary deficiency between below 40 μg/day of toxic levels and over 400 μg/day (Fu et al., 2014). The World Health

Published online: 21 April 2020

Organization (WHO) currently determines 40 μg/L as the maximum acceptable concentration (MAC) in drinking water, while the United States Environmental Protection Agency (US-EPA) has mandated a maximum contaminant level at 50 μg/L of selenium in drinking water (Fu et al., 2016). However, the toxic effects of high levels of selenium in wildlife have previously been reported, including tissue damage, chronic kidney disease, reproductive failure, and teratogenic effects (Bajaj et al., 2011).

Selenium exists in water in several forms depending on its oxidation states, such as selenate (SeO_4^{2-} or Se^{6+}), selenite (SeO_3^{2-} or Se^{4+}), selenium (Se^0), selenide (Se^{2-}), and organic selenium. Se^{6+} and Se^{4+} are found in most aqueous media and comprise the predominant chemical forms (Jegadeesan et al. 2015). Generally, Se^{6+} is considered the most toxic species and oxidized form with high solubility in water. Se^{4+} is less available to organisms as a consequence of its affinity to adsorption sites of sediment and soil constituents (Yamani et al. 2014). Normally, Se^{6+} can be adsorbed in an outer-sphere adsorption manner weaker than inner-sphere adsorption, which could be the reason for less effective Se^{6+} removal using conventional adsorbents (Fu et al., 2014). During the infiltration of surface water, mobile Se^{6+} is weakly adsorbed by minerals, thus becoming the main species in groundwater (Gibson et al., 2012). Hence, Se^{6+} is more mobile in groundwater and most Se^{6+} from polluted water ends up in groundwater. Therefore, it is very important to identify and evaluate additional potential methods for the removal of selenium from wastewater before it is discharged into the natural environment. Strategies for the removal of soluble selenium in water will most likely involve the reduction of Se^{6+} into selenium species with lower valence (Se^{6+}, Se^0, and/or Se^{2-}).

Recently, there has been growing interest in treatment technology that can remove both Se^{6+} and/or Se^{4+} simultaneously. On the other hand, more researches have been reported that various treatment technologies to remove selenium from aqueous environments, including reduction (Ling et al., 2015), adsorption (Tian et al., 2017), biological treatment (Tan et al., 2016), membrane separation processes (Subramani et al., 2012), ion exchange (Staicu et al., 2017), coagulation (Hu et al., 2015), and electrocoagulation (Hansen et al., 2019). Among these methods, the reduction has received a great deal of attention because of its low cost and high efficiency (Mondal, 2009).

Nanoscale zero-valent iron (NZVI) is widely used for the removal of pollutants from wastewater the consequence of its well-known high specific surface area, low cost, high reactively strong reduction capacity, and fewer pollutants (Dong et al., 2016). These properties can increase the adsorption capacity and surface activity, specifically in acidic conditions. The aggregation of NZVI affected large particle size and decreasing surface area of NZVI, resulting in decreased mobility and reactivity (Fu et al., 2015; Xi et al., 2014). The NZVI is consist of a metallic iron (Fe^0) core encapsulated by a thin oxide shell, which is related to its core-shell structure. The Fe^0 core in the NZVI oxidizes upon reaction with water and oxygen, and ultimately, the metallic iron is exhausted to form iron oxides and hydroxides cause the surface corrosion or aging properties of NZVI (Liu et al. 2015). Besides, the NZVI nanoparticles easily agglomerate on one another, which is permitted by the solutes adsorption through electrostatic interaction and surface complexation (Sheng et al., 2016). To interrupt cumulative surface oxidation and enhance NZVI dispersibility in aqueous solutions, significant advances have been achieved by the synthesis of NZVI-based composites to enhance capacity and longevity. To overcome this problem, methods, for instance, electrostatic and stabilization, have been used to improve the stability of nanomaterials (Sun et al., 2007).

The immobilization of NZVI on several kinds of supports has shown the capacity to inhibit further surface oxidation and improve the colloidal stability of iron nanoparticles such as bentonite (Li et al., 2012), zeolite (Kim et al. 2013), kaolinite (Zhang et al., 2011), titanium dioxide (Shirazi et al., 2013), chitosan (Geng et al., 2009), graphene (Liu et al. 2014b), polyacrylic acid (Jiemvarangkul et al., 2011), and carboxymethyl cellulose (Dong et al., 2011). Commonly, the most important parameters considered when selecting the type of supporting materials are as follows: low price, biocompatibility, high surface area and pore volume, mechanical resistance, and sheet-like structure (Chen et al., 2016).

Fly ash is one of the by-products emitted by coal-fired power plants. Presently, fly ash is used in the construction industry by mixing it with an alkaline solution to produce geopolymer cement, which has higher quality than conventional cement (Ma et al., 2016). Fly ash comprises significant amounts between 50 and 70% by weight of SiO_2, Al_2O_3, and Fe_2O_3 (ASTM standard) (Chansiriwat et al., 2016).

Amorphous and crystalline phases of Si and Al make it possible to apply fly ash as source material for synthesizing zeolite (Thuadaij and Nuntiya, 2012). Zeolite is a microporous material and aluminosilicate minerals are commonly used as adsorbents for removing pollutants (Yao et al., 2018). Coal fly ash was used to synthesize zeolite; especially interesting is that it allows undesirable waste to be transferred into high value-added products. Zeolite Na-P1 (Z) or $Na_6Al_6Si_{10}O_{32}{\cdot}12H_2O$ is a synthetic material with a high ion exchange capacity (0.72–3.9 meq/g) (Wdowin et al., 2012), since the substitution of Si^{4+} by Al^{3+} in its structure, which produces in the overall negative charge, inducing to the application as ion exchange or molecular sieve. Hence, zeolite offers significant potential for industrial and environmental applications (Blissett and Rowson, 2012).

Zeolite can be composited with other supporting materials so that they are tailored for special demands. For example, zeolite has been incorporated in zerovalent iron (Kong et al., 2016), chitosan (Wan Ngah et al., 2013), TiO_2 (Zhang et al., 2018), and geopolymer (Minelli et al., 2018). The porous structure of zeolite Na-P1, its available surface area which is suitably supported material by incorporated iron ions which are reduction ability of NZVI, and the composite also have synergetic effects due to the better dispersion of NZVI on zeolite (Kong et al. 2016). Zeolite-supported nanoscale zerovalent iron (Z-NZVI) may combine the adsorption ability of zeolite and the reduction ability of NZVI, while the composite also has synergetic effects due to enhanced dispersion and stabilization of NZVI on zeolite (Kim et al. 2013). The combination of a reduction and adsorption process, which reduces Se^{6+} to Se^{4+}/Se^0 followed by the adsorption of Se^{4+}/Se^0, has certain advantages in selenium removal. Consequently, Z-NZVI is required to remove heavy metal cations and anions simultaneously and efficiently. However, only limited attempts have been made to stabilize NZVI with zeolite for the removal of pollutants from water (Kim et al. 2013). Owing to the lack of effective experimental methods, previous studies have mainly focused on the single metal adsorption capacities of specific adsorbents and ignored the interactions with other heavy metals in natural water (Li et al. 2018).

In the present work, zeolite Na-P1 as support for the immobilization of NZVI is employed to remove Se^{6+} in wastewater. The composite Z-NZVI combines the advantages of simultaneous reduction and adsorption. The main objectives of this work are, firstly, to synthesize a novel composite Z-NZVI and then characterize it before and after selenium removal by using X-ray Diffraction (XRD), Fourier-transform infrared spectrometer (FT-IR), and high-resolution transmission electron microscopy with energy-dispersive X-ray spectroscopy (HR-TEM-EDS). The second objective is to estimate the optimum conditions for Se^{6+} removal and compare the performance and kinetics of Se^{6+} removal by Z, NZVI, and Z-NZVI. Thirdly, this study aims to propose a reaction mechanism for Se^{6+} removal using NZVI coupled with zeolite by X-ray absorption near-edge structure (XANES), which has been increasingly used to determine oxidation states. The final objective is to develop an efficient method for using Z-NZVI to treat Se^{6+}.

2 Experimental Methods

2.1 Materials and Chemicals

The chemicals used in this study included sodium selenate decahydrate ($Na_2SeO_4{\cdot}10H_2O$, Sigma-Aldrich), sodium selenite (Na_2SeO_3, Sigma-Aldrich), sodium hydroxide (NaOH, RCI Labscan), iron (II) sulfate heptahydrate ($FeSO_4{\cdot}7H_2O$, QRëC), and sodium borohydride ($NaBH_4$, Loba Chemie Pvt. Ltd.). All chemicals were analytical grade (99% purity).

2.2 Preparation of Z and Z-NZVI Synthesis

2.2.1 Z Synthesis

The Z synthesis was prepared using the following procedure (Chansiriwat et al., 2016). Solution A was prepared by both 10 g of NaOH and 16.86 g of fly ash mixed with deionized water at 100 °C under vigorous mixing. Then, 10 g of solution A was mixed with 5.61 g of NaOH, which is called seed gel. Solution B was prepared by both 8.27 g of NaOH and 7.98 g of fly ash mixing with deionized water at 100 °C under vigorous mixing, which is called mother gel. Afterward, both the seed gel and mother gel solutions were thoroughly mixed and continuously stirred for more than 30 min. Next, the mixed solution was transferred to a Teflon-lined, stainless steel autoclave and then aged in an oven at 100 °C for 12 h. Finally, the solid solution was obtained after aging in the oven. Following this, it was separated by centrifugal technique. The supernatant

liquid was removed and the solid was washed with distilled water until the pH was lower than 9.0, followed by drying in an oven at 100 °C for 24 h.

2.2.2 Z-NZVI Synthesis

The Z-NZVI was prepared according to Li et al. 2018. Firstly, 1 g of $FeSO_4 \cdot 7H_2O$ and 0.75 g of Z were mixed in 250 mL of deionized water. Secondly, the pH of the solution was adjusted to 4 with 1 M HNO_3. Thirdly, the mixture was treated by stirring vigorously at ambient temperature for 30 min. Fourthly, 25 mL of 1 M $NaBH_4$ solution was added at 1 mL/min while stirring to ensure the efficient reduction of Fe^{2+}. The reduction reaction Eq. (1)) is as follows:

$$Fe^{2+} + 2BH_4^- + 6H_2O \rightarrow Fe^0 + 2B(OH)_3 + 7H_2\uparrow \quad (1)$$

Fifthly, the Z-NZVI particles were then washed several times with DI water before use. Finally, the Z-NZVI particles formed were separated from the liquid solution using a magnet.

2.3 Z, NZVI, and Z-NZVI Characterizations

The crystallinity of fly ash and Z were determined using an X-ray diffractometer (XRD) (D8 Discover, Bruker AXS) with Cu K_α radiation ($\lambda = 0.1514$ nm) at 40 mA and 40 kV. The scan range was 10–50° with an increment of 0.02°/step, and a scan speed of 0.1 s/step at 298 K. The point of zero charge was determined according to the method recommended previously (Lee et al. 2013). Fourier transform infrared spectrometer (FT-IR), Spectrum One, Perkin-Elmer, USA, was used to determine the components in a mixture and interfacial bonding mechanism of aluminum, silica, and iron. With the sample mixed in KBr pellet at room temperature, spectra were gotten over the range of 400–4000 cm^{-1}. Particle shape and particle size distribution were observed using high-resolution transmission electron microscopy with energy-dispersive X-ray spectroscopy (HR-TEM-EDS) (JEM-2100 Plus, JEOL). The oxidation states of both selenium and iron in NZVI and Z-NZVI samples were collected at different intervals, washed with distilled water, freeze-dried, and put into zippered bags before subjecting to Se K-edge and Fe K-edge X-ray absorption near-edge structure (XANES) technique. XANES analysis was performed at Beamline 1.1:Multiple X-ray techniques, the Synchrotron Light Research Institute (public organization) (Nakhon Ratchasima, Thailand). The Athena software was used to normalize and analyze the XANES spectra of standards and samples. The Athena software also used linear combination fitting. The details of XANES analysis are present in previous studies (Khamdahsag et al. 2018; Ravel and Newville 2005; Sarret et al. 2005; Wang et al. 2013).

2.4 Se^{6+} Removal by NZVI and Z-NZVI

Batch experiments were conducted by combining 500-mL initial 15 mg/L of Se^{6+} with 0.75 g of Z, 0.15 g of NZVI, and 0.90 g of Z-NZVI deriving from 0.75 g of Z and 0.15 g of NZVI synthesis. Contact time for all experiments was in the range of 0–30 min. The eluent was then analyzed for selenium concentration by inductively coupled plasma-optical emission spectrometry (ICP-OES). The previous publication has suggested that the reaction rate could be estimated with conventional pseudo-first-order kinetics (Kim et al. 2010):

$$\frac{d[\mathrm{Se(VI)}]}{dt} = -k_{\mathrm{obs}}[\mathrm{Se(VI)}] \quad (2)$$

The concentration of selenium in the aqueous phase (mg/L); k_{obs} is the observed rate constant (min^{-1}), and t is the reaction time (min). Integration of Eq. (2) yields:

$$\ln\left(\frac{C}{C_0}\right) = -k_{\mathrm{obs}}t \quad (3)$$

where C_0 is the initial chromium concentration. Accordingly, a plot of $\ln(C/C_0)$ versus t gives a linear relationship, where the slope represents k_{obs} using the following Eq. (3).

3 Results and Discussion

3.1 Z, NZVI, and Z-NZVI Characteristics

3.1.1 X-Ray Diffraction Analysis and Point of Zero Charge

The XRD results for crystallite samples of fly ash and Z synthesis after the hydrothermal process are shown in Fig. 1. Mullite and Hematite peaks were observed in the XRD pattern of fly ash, consistent with the results reported by (Chansiriwat et al. 2016). After the

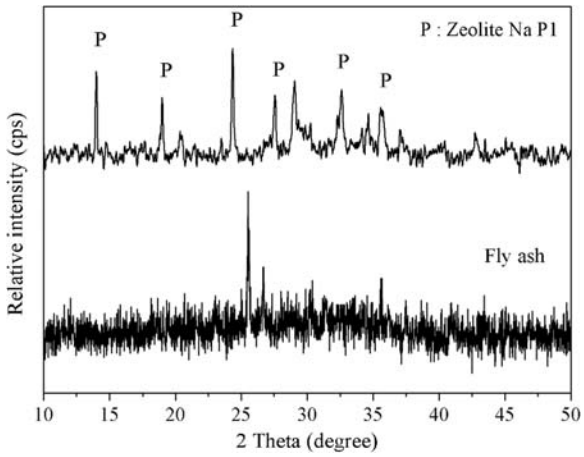

Fig. 1 XRD patterns of fly ash and synthesized zeolite Na-P1

hydrothermal process, new peaks were formed and their positions were corresponded to the zeolite peaks in Z according to JCPDS 39-0219 standard as well as previous studies (Izidoro et al. 2012). To determine the variation of the surface charge of Z, NZVI, and Z-NZVI as a function of pH, point zero of charge measurements at different pH were carried out. As shown in Fig. 2, the point zero of charge of Z, NZVI, and Z-NZVI are 10, 8.7, and 8, respectively. Thus, pH greater than the point zero of charge leads to the surface possessing negative charges, while pH lower than point zero of charge results in a positive charge at the surface of all three materials. The point zero of charge of Z-NZVI was found to be less than Z and NZVI because of substantial modification in the point zero of charge of zeolite functionalized with NZVI. This indicated a significant change in the surface charge behavior of the Z-NZVI composite (Suazo-Hernández et al. 2019).

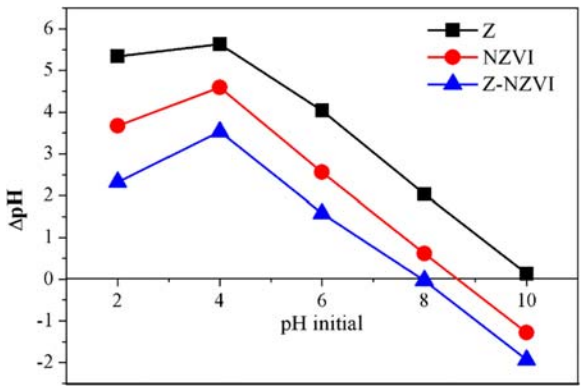

Fig. 2 Point of zero charge of Z, NZVI, and Z-NZVI

3.1.2 FT-IR Spectrum Analysis

The FT-IR spectra for Z, fresh NZVI, and spent-Z-NZVI were scanned in the range of 400–4000 cm^{-1} as shown in Fig. 3(a–c). The band at 3460 cm^{-1} and 3330 cm^{-1}, corresponding to O–H vibration of the H_2O molecule in the Z mesosphere materials and O–H vibration of the H_2O structure in Z octahedron, was related to adsorbed water, which reduces slightly after the synthesis of Z-NZVI. The presence of bands at 1034 and 910 cm^{-1} are the stretching vibrations for Si–O and Al–O, respectively. The major peak of the Z band at 1000 cm^{-1} in the composite and band shifts in this region suggest H-bond breaking due to the presence of Fe on the SiO_4 and AlO_4 surfaces of Z (Canafoglia et al., 2009). The intensity of the bands at 1433 cm^{-1} disappeared after both fresh Z-NZVI and spent-Z-NZVI corresponded to the Fe–O stretch for the existing iron oxides. Absorption bands of zeolite at ~ 1440 cm^{-1} were assigned to the amorphous material (Li et al. 2016). The presence of the amorphous content and the mixture of different aluminosilicate species were a result of the dissolution of the crystalline content of the microsphere because the zeolite was not yet formed at this stage (Kunecki et al. 2018). However, both fresh Z-NZVI and spent Z-NZVI are disappeared of the bands at 1440 cm^{-1}, which demonstrates the extensive substitution of hydroxyl protons by iron ions and the removal of part of the −OH groups during synthesis material and catalytic reaction (Oleksenko et al. 2004). Furthermore, NZVI and Z-NZVI peak at 624 cm^{-1} corresponding to Fe–O stretches of Fe_2O_3 and Fe_3O_4 were observed in

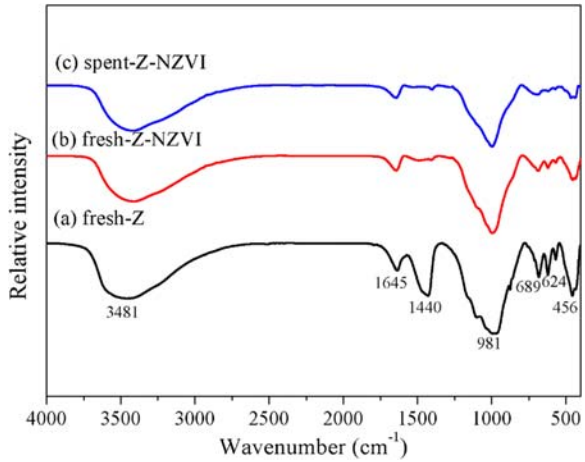

Fig. 3 FT-IR spectra of (a) fresh-Z, (b) fresh-Z-NZVI, and (c) spent-Z-NZVI

Fig. 3(b, c), consistent with the results that demonstrated NZVI had been successfully loaded onto Z, where the surface of the supported NZVI was partially oxidized (Zhang et al. 2011).

3.1.3 High-Resolution Transmission Electron Microscopy with Energy-Dispersive X-Ray Spectroscopy

Typical HR-TEM images of the NZVI and Z-NZVI are shown in Fig. 4(a–d), respectively. NZVI had spherical assemblages with strikingly uniform morphology and particle size distribution histograms with an average diameter of approximately 11.02 nm based on a count of 100 particles. Figure 4(c, d) illustrates that some NZVI particles were even embedded in a Z matrix structure. Figure 5 shows selected area electron diffraction of crystallinity for nanoparticle materials, which is evident from the well-formed lattice fringes with an interplanar *d* spacing of 0.48 nm, corresponding to the (111) iron oxide planes. Iron oxides (oxy)hydroxides are highly crystalline and the diffraction peaks can be indexed to (111), (220), (311), (400), (511), and (440) planes (Liu et al. 2014a). Compared with the right panel of EDS elemental mapping images of Fe-K signals in Fig. 5(a, b), Z-NZVI had a better dispersion of iron, which means that Z was incorporated successfully. Thus, HR-TEM-EDX results confirm the difference in particle size and the dispersion of NZVI after Z incorporation.

3.1.4 X-Ray Absorption Near-Edge Structure

The characteristics of Se and Fe species after reaction used to consider the mechanisms correlated to Z-NZVI for Se^{6+} removal were defined by the XANES spectra. The XANES spectra of our selenium and iron reference compound for different oxidation state samples of Se^{6+} with NZVI and Z-NZVI at different reaction times are displayed in Figs. 7 and 8. Relying on the oxidation state of selenium, the XANES spectra varied in terms of edge position. The XANES spectra found Se^0, Se^{4+}, and Se^{6+} show energy (E^0) at 12,658, 12,662, and 12,664.80 eV, respectively, which were following the values observed in a previous study (Akiho et al., 2012). The differences reflected variations in the structural environment of selenium. For the samples of Se^{6+} removal by NZVI and Z-NZVI at 15 and 90 min, the XANES spectra were quite like Se^0 standard, introducing that Se^{6+} was completely reduced to Se^0 under every condition of the experiment. Consequently, the XANES analysis approved that using Z as support enhanced the removal efficiency of Se^{6+} by NZVI due to accelerating the reductive translation of Se^{6+} into less soluble Se^0 with low toxicity. Moreover, the reductive transformation of Se^{6+} to Se^0 by NZVI and Z-NZVI was the driving force

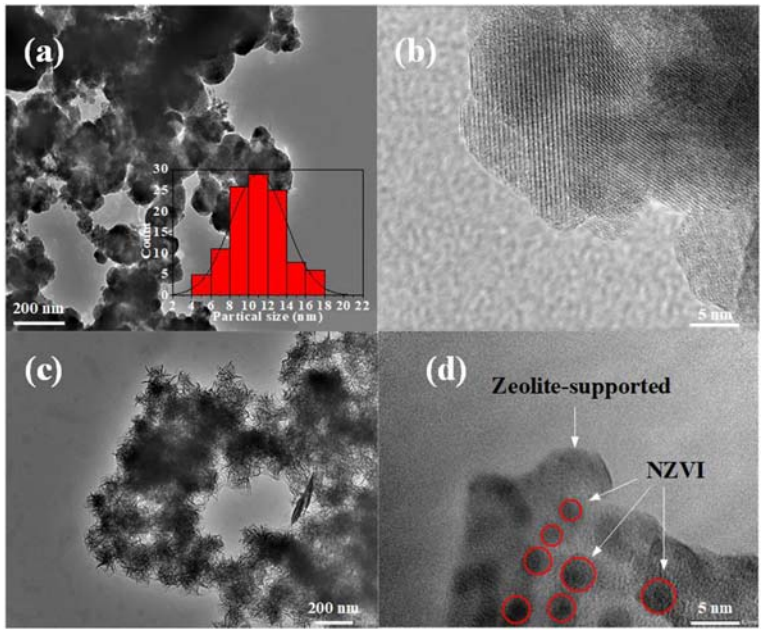

Fig. 4 TEM images of NZVI (a) ×40 k (b) ×1.5 M and Z-NZVI (c) ×30 k (d) ×800 k

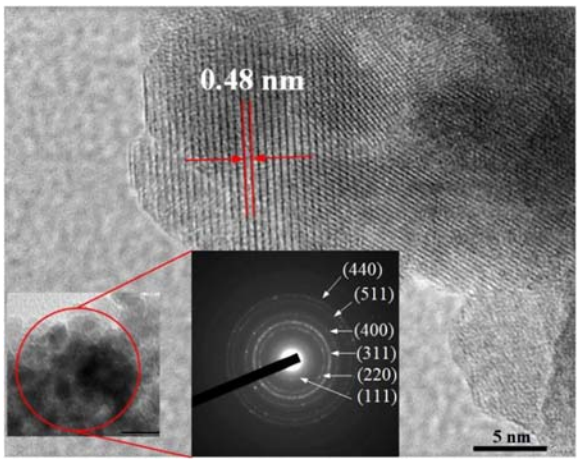

Fig. 5 TEM micrograph of NZVI selected with selected area electron diffraction patterns

for the subsequent adsorption of Se^{6+} and the remaining Se0 onto the corroded NZVI surface.

Linear combination fitting (LCF) was performed on the data using a dataset of reference spectra including selenium oxidation form. The results of the LCF procedure (Table 1) displayed that most of the selenium was present in Se^0 form in all samples. Fe form in the solid phase was present as Fe^0 in the presence of NZVI after removal at 15 min and then Fe^0 decreased rapidly from 71.9 to 18.8% within 75 min. The Fe_2O_3 and FeOOH content gradually increased after the reaction of all samples. In the conclusion of LCF results, NZVI demonstrated that Se^0 was the final reductive product Se^{6+} with relatively fast kinetics. Z-NZVI after removal for 90 min suggests that Se^0 and Se^{6+} account for 85.2% and 20.5%, respectively, with a high goodness of fit (*R*-factor 0.0055 less than 0.05), which quantitatively represents the dominant removal Se^{6+} on Z-NZVI.

The Fe K-edge XANES spectra revealed that Fe^0, FeO, Fe_3O_4, and FeOOH were the main corrosion products of NZVI and Z-NZVI after removal for 15 and 90 min in Fig. 8. The measured E^0 values for Fe^0, FeO, Fe_3O_4, and FeOOH were 7112, 7118.99, 7122.88, and 7125.09 eV, respectively. It was noteworthy that the adsorption of Se^{6+} on iron (hydr)oxides, both Fe_3O_4 and FeOOH, was weak and the adsorption capacity of iron (hydr)oxides for Se^{6+} was negligible. The result can be summarized that NZVI was sequentially changed to Fe_3O_4 and then to FeOOH in the process of Se^{6+} removal by Z-NZVI, which was identical to results reported in previous studies (Liang et al., 2013) and could be explained by Eqs. (4)–(6).

$$2Fe^0 + O_2 + 2H_2O \rightarrow 2Fe^{2+} + 4OH^- \quad (4)$$

$$6Fe^{2+} + O_2 + 6H_2O \rightarrow 2Fe_3O_4 + 12H^+ \quad (5)$$

$$4Fe^{2+} + O_2 + 6H_2O \rightarrow 4FeOOH + 12H^+ \quad (6)$$

3.2 Se^{6+} Removal by NZVI and Z-NZVI

Batch experiments were carried out by initially combining 15 mg/L Se^{6+} with 0.75 g Z, 0.15 g NZVI, and 0.9 g Z-NZVI. Contact time for all experiments was also observed, in which the evaluation of the initial reaction rate from 0 to 30 min was most effective in explaining the data. Figure 9 (a) shows the applied NZVI dosage on Z. More available active sites were available for Se^{6+} rapid adsorption and reduction, resulting in a higher removal rate. Z shows that it cannot remove selenium because of the electrostatic repulsion of the surface between the Z and selenium, which suggests no selenium reacted with the surface Si–O and Al–O group on Z. As the NZVI particles itself are normally likely to aggregate when it is in the solution, the existence of the zeolite in Z-NZVI could help to reduce the aggregation

Table 1 Linear combination fitting of the XANES data for NZVI and Z-NZVI after reaction at 15 and 90 min

Samples	Se and Fe species proportions (%)						
	Se^0	Se^{6+}	Se^{4+}	Fe^0	Fe_2O_3	FeOOH	FeO
NZVI 15 min	82.3	9.0	9.1	71.9	3.2	0	26.0
NZVI 90 min	76.9	8.9	12.6	18.8	26.8	20.5	35.0
Z-NZVI 15 min	72.2	28.5	0	0	38.1	40.1	21.8
Z-NZVI 90 min	85.2	20.5	0	8	44.5	53.2	0

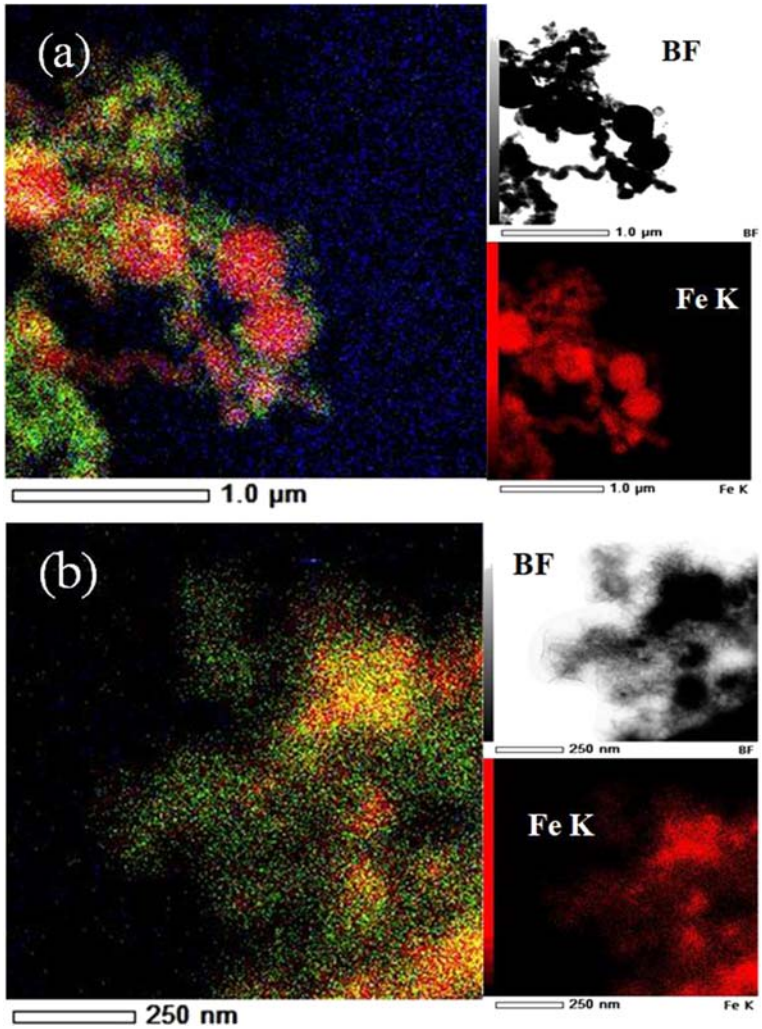

Fig. 6 TEM-EDS images of NZVI (a) and Z-NZVI (b)

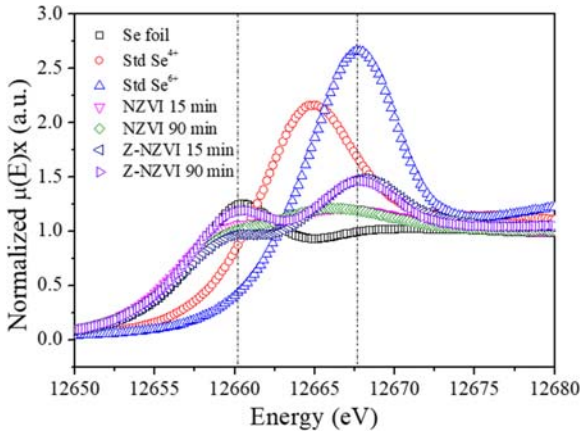

Fig. 7 Se K-edge XANES spectra of NZVI and Z-NZVI reacted with 15 mg/L Se^{6+} for 15 and 90 min

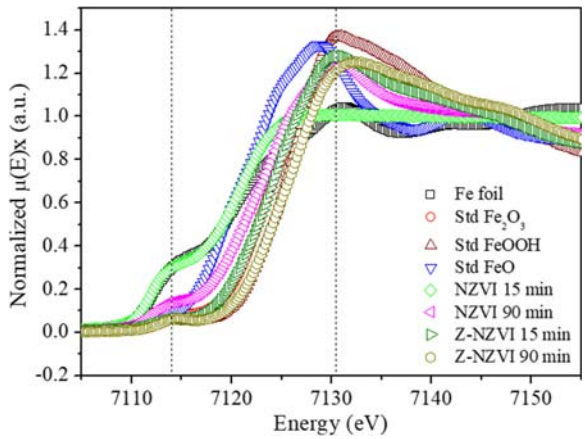

Fig. 8 Fe K-edge XANES spectra of NZVI and Z-NZVI reacted with 15 mg/L Se^{6+} for 15 and 90 min

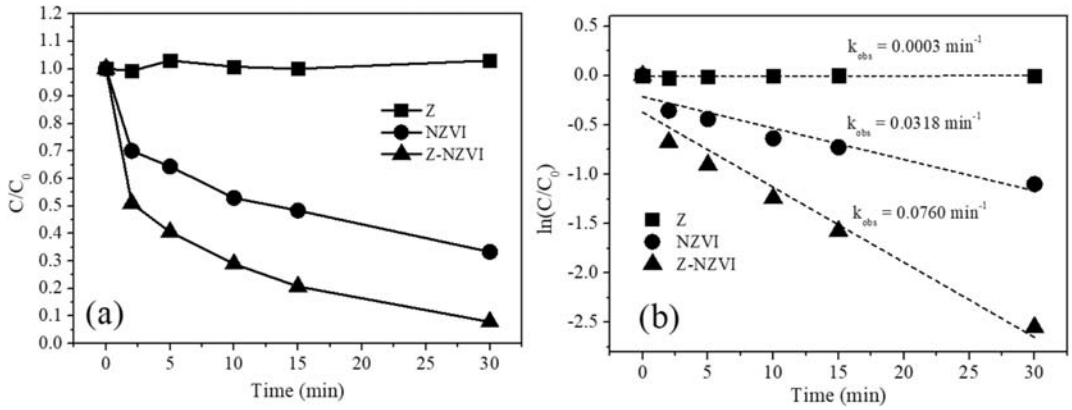

Fig. 9 Se^{6+} removal by Z, NZVI and Z-NZVI (a) and their linearized data (b)

of NZVI particles, thereby improving its dispersion and specific surface area (Li et al. 2018). This corresponded to the results of HR-TEM-EDS in Fig. 6. However, the NZVI and Z-NZVI have high removal efficiencies for selenium. There are sharply steep declines at 0–5 min with a gradual downward trend between 5 and 30 min. Furthermore, the lines in Fig. 9(b) comprise the back-calculated results derived from the linearized data in Fig. 10(a). The time-dependent removal of dissolved Se^{6+} shows a considerably higher rate of Se^{6+} removal from the aqueous solution by Z, NZVI, and Z-NZVI. The slopes of the fit linear equations yielded k_{obs} values of 0.0003, 0.0318, and 0.0760 min^{-1} for Z, NZVI, and Z-NZVI, respectively. The results showed an obvious dependence on the initial concentration of Se^{6+}.

For the solution pH of Se^{6+} removal by Z, NZVI, and Z-NZVI, as shown in Fig. 10(a), the solution pH increased. Decreasing concentrations of selenium would appear due to the precipitation of iron (hydr)oxides that could shield the active sites on NZVI and Z-NZVI surface and the attenuation of selenium adsorption (Liang et al., 2013). The relationship between the reaction time and ORP is shown in Fig. 10(b). It can be concluded that the drop in ORP is necessary for Se^{6+} removal by NZVI and Z-NZVI and that the variation in ORP values is indicative of the progress of the reaction between Se^{6+} and NZVI and Z-NZVI.

3.3 Proposed Mechanism of Se^{6+} Removal by Z-NZVI

Considering the evidence provided by XANES analysis and the removal properties of $Se^{6+}$and Se^{0}, the possible mechanisms of Se^{6+} removal by Z-NZVI (Fig. 11) are proposed in the previous study as follows (Liang et al. 2015):

$$3Fe^{0} + SeO_4^{2-} + 8H^{+} \rightarrow 3Fe^{2+} + Se^{0} + 4H_2O \text{ (selenate reduction)} \quad (7)$$

$$3Fe^{2+} + Se^{0} + 2OH^{-} \rightarrow FeOOH + Se^{0} \text{ (precipitation)} \quad (8)$$

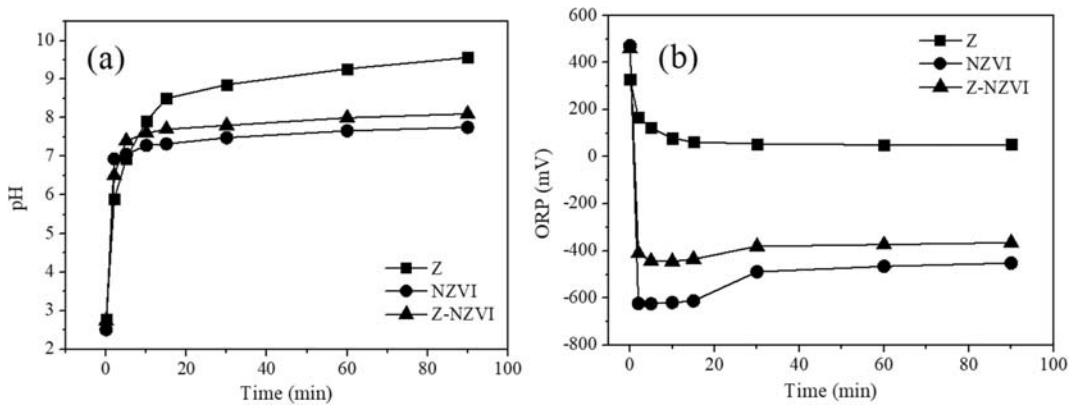

Fig. 10 pH (a) and ORP (b) during the reaction of Se^{6+} removal by Z, NZVI, and Z-NZVI

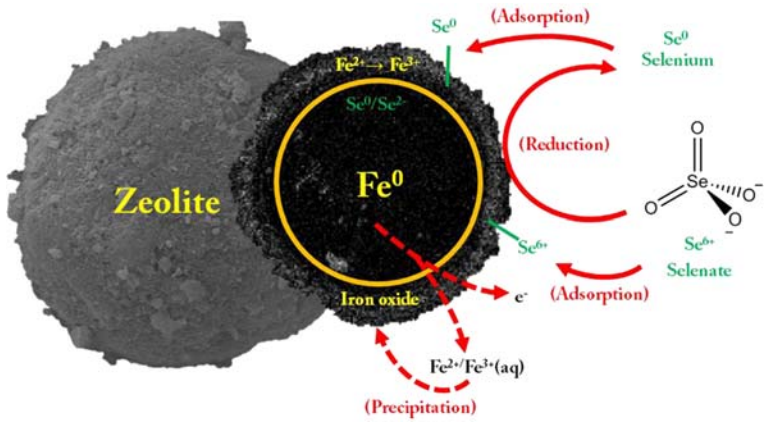

Fig. 11 Proposed mechanism of selenium reduction and adsorption by Z-NZVI

Se^{6+} was sequentially reduced by Z-NZVI to Se^{4+} and Se^{0}, following Eqs. (7) and (8). However, Se^{6+} can be adsorbed onto the surface and then be reduced by electrons that are donated by Z-NZVI for these reductive reactions to occur. For this reason, it can be inferred that the reductive transformation of Se^{6+} to Se^{0} was the driving force for the subsequent adsorption of Se^{6+} onto the corroded Z-NZVI surface. Additionally, zeolite-supported nanoscale zero-valent iron has been considered as a good adsorbent for selenium removal. Therefore, the reductive transformation of Se^{6+} to Se^{0} removed by Z-NZVI involves both reduction and adsorption mechanisms. For future work, we are inclined to conclude the classification of inner- and outer-sphere coordination by extended X-ray absorption fine structure (EXAFS) analysis.

4 Conclusion

This study demonstrated that Se^{6+} could be effectively removed by Z-NZVI. The morphology analysis represented the distribution of the NZVI particles on the Z surfaces. The batch experiments indicated that Z-NZVI had more active sites available for Se^{6+} rapid reduction and sorption, resulting in higher removal kinetic rate. Se K-edge and Fe K-edge XANES spectra indicated that Se^{6+} was sequestered by adsorption to the corroded NZVI surface, followed by fast reduction to Se^{0} with FeOOH as the final corrosion product of Z-NZVI. The results of this study suggest that enhanced Se^{6+} removal by Z-NZVI is highly effective as a perceived mechanism.

Funding Information This work was financially supported by the Electricity Generating Authority of Thailand (EGAT), Faculty of Engineering, Khon Kaen University, Research and Technology transfer affairs of Khon Kaen University, The Thailand Research Fund (MRG6180196), and Office of the Higher Education Commission. The authors also would like to acknowledge Synchrotron Light Research Institute (Public Organization).

References

Akiho, H., Yamamoto, T., Tochihara, Y., Noda, N., Noguchi, S., & Ito, S. (2012). Speciation and oxidation reaction analysis of selenium in aqueous solution using X-ray absorption spectroscopy for management of trace element in FGD liquor. *Fuel, 102*, 156–161.

Bajaj, M., Eiche, E., Neumann, T., Winter, J., & Gallert, C. (2011). Hazardous concentrations of selenium in soil and groundwater in north-West India. *Journal of Hazardous Materials, 189*(3), 640–646.

Blissett, R. S., & Rowson, N. A. (2012). Review article A review of the multi-component utilisation of coal fly ash. *Fuel, 97*, 1–23.

Canafoglia, M. E., Lick, I. D., Ponzi, E. N., & Botto, I. L. (2009). Natural materials modified with transition metals of the cobalt group: feasibility in catalysis. *The Journal of the Argentine Chemical Society, 97*, 58–68.

Chansiriwat, W., Tanangteerapong, D., & Wantala, K. (2016). Synthesis of zeolite from coal fly ash by hydrothermal method without adding alumina and silica sources: effect of aging temperature and time. *Sains Malaysiana, 45*(11), 1723–1731.

Chen, H., Cao, Y., Wei, E., Gong, T., & Xian, Q. (2016). Facile synthesis of graphene nano zero-valent iron composites and their efficient removal of trichloronitromethane from drinking water. *Chemosphere, 146*, 32–39.

Dong, H., Chen, Y., Sheng, G., Li, J., Cao, J., Li, Z., & Li, Y. (2016). The roles of a pillared bentonite on enhancing se(VI) removal by ZVI and the influence of co-existing solutes in groundwater. *Journal of Hazardous Materials, 304*, 306–312.

Dong, T., Luo, H., Wang, Y., Hu, B., & Chen, H. (2011). Stabilization of Fe-Pd bimetallic nanoparticles with sodium

carboxymethyl cellulose for catalytic reduction of para-nitrochlorobenzene in water. *Desalination, 271*, 11–19.

Fu, F., Lu, J., Cheng, Z., & Tang, B. (2016). Removal of selenite by zero-valent iron combined with ultrasound: Se(IV) concentration changes, Se(VI) generation, and reaction mechanism. *Ultrasonics Sonochemistry, 29*, 328–336.

Fu, R., Yang, Y., Xu, Z., Zhang, X., Guo, X., & Bi, D. (2015). The removal of chromium (VI) and lead (II) from groundwater using sepiolite-supported nanoscale zero-valent iron (S-NZVI). *Chemosphere, 138*, 726–734.

Fu, Y., Wang, J., Liu, Q., & Zeng, H. (2014). Water-dispersible magnetic nanoparticle-graphene oxide composites for selenium removal. *Carbon, 77*, 710–721.

Geng, B., Jin, Z., Li, T., & Qi, X. (2009). Kinetics of hexavalent chromium removal from water by chitosan-Fe0 nanoparticles. *Chemosphere, 75*(6), 825–830.

Gibson, B. D., Blowes, D. W., Lindsay, M. B. J., & Ptacek, C. J. (2012). Mechanistic investigations of se(VI) treatment in anoxic groundwater using granular iron and organic carbon: an EXAFS study. *Journal of Hazardous Materials, 241–242*, 92–100.

Gonzalez, C. M., Hernandez, J., Parsons, J. G., & Gardea-Torresdey, J. L. (2010). A study of the removal of selenite and selenate from aqueous solutions using a magnetic iron/manganese oxide nanomaterial and ICP-MS. *Microchemical Journal, 96*(2), 324–329.

Hansen, H. K., Peña, S. F., Gutiérrez, C., Lazo, A., Lazo, P., & Ottosen, L. M. (2019). Selenium removal from petroleum refinery wastewater using an electrocoagulation technique. *Journal of Hazardous Materials, 364*, 78–81.

Hu, C., Chen, Q., Chen, G., Liu, H., & Qu, J. (2015). Removal of se(IV) and se(VI) from drinking water by coagulation. *Separation and Purification Technology, 142*, 65–70.

Izidoro, J. D. C., Fungaro, D. A., Dos Santos, F. S., & Wang, S. (2012). Characteristics of Brazilian coal fly ashes and their synthesized zeolites. *Fuel Processing Technology, 97*, 38–44.

Jegadeesan, G. B., Mondal, K., & Lalvani, S. B. (2015). Adsorption of se (IV) and se (VI) using copper-impregnated activated carbon and Fly ashextracted char carbon. *Water, Air, and Soil Pollution, 226*(8), 226–234

Jiemvarangkul, P., Zhang, W. X., & Lien, H. L. (2011). Enhanced transport of polyelectrolyte stabilized nanoscale zero-valent iron (nZVI) in porous media. *Chemical Engineering Journal, 170*, 482–491.

Khamdahsag, P., Khemthong, P., Sitthisuwannakul, K., Grisdanurak, N., Wutikhun, T., Rungnim, C., et al. (2018). Insights into binding mechanism of silver/titanium dioxide composites for enhanced elemental mercury capture. *Materials Chemistry and Physics, 215*, 1–10.

Kim, H., Hong, H., Jung, J., Kim, S., & Yang, J. (2010). Degradation of trichloroethylene (TCE) by nanoscale zero-valent iron (nZVI) immobilized in alginate bead. *Journal of Hazardous Materials journal, 176*, 1038–1043.

Kim, S. A., Kamala-Kannan, S., Lee, K. J., Park, Y. J., Shea, P. J., Lee, W. H., et al. (2013). Removal of Pb(II) from aqueous solution by a zeolite-nanoscale zero-valent iron composite. *Chemical Engineering Journal, 217*, 54–60.

Kong, X., Han, Z., Zhang, W., Song, L., & Li, H. (2016). Synthesis of zeolite-supported microscale zero-valent iron for the removal of Cr^{6+} and Cd^{2+} from aqueous solution. *Journal of Environmental Management, 169*, 84–90.

Kunecki, P., Panek, R., Koteja, A., & Franus, W. (2018). Influence of the reaction time on the crystal structure of Na-P1 zeolite obtained from coal fly ash microspheres. *Microporous and Mesoporous Materials, 266*, 102–108.

Lee, Y. R., Kim, J., & Ahn, W. S. (2013). Synthesis of metal-organic frameworks: a mini review. *Korean Journal of Chemical Engineering, 30*(9), 1667–1680.

Li, Y., Peng, T., Man, W., Ju, L., Zheng, F., Zhang, M., & Guo, M. (2016). Hydrothermal synthesis of mixtures of NaA zeolite and sodalite from Ti-bearing electric arc furnace slag. *RSC Advances, 6*, 8358–8366.

Li, Y., Li, J., & Zhang, Y. (2012). Mechanism insights into enhanced Cr(VI) removal using nanoscale zerovalent iron supported on the pillared bentonite by macroscopic and spectroscopic studies. *Journal of Hazardous Materials, 227–228*, 211–218.

Li, Z., Wang, L., Meng, J., Liu, X., Xu, J., Wang, F., & Brookes, P. (2018). Zeolite-supported nanoscale zero-valent iron: new findings on simultaneous adsorption of cd(II), Pb(II), and as(III) in aqueous solution and soil. *Journal of Hazardous Materials, 344*, 1–11.

Liang, L., Guan, X., Huang, Y., Ma, J., Sun, X., Qiao, J., & Zhou, G. (2015). Efficient selenate removal by zero-valent iron in the presence of weak magnetic field. *Separation and Purification Technology, 156*, 1064–1072.

Liang, L., Yang, W., Guan, X., Li, J., Xu, Z., Wu, J., Huang, Y., & Zhang, X. (2013). Kinetics and mechanisms of pH-dependent selenite removal by zero valent iron. *Water Research, 47*(15), 5846–5855.

Ling, L., Pan, B., & Zhang, W. X. (2015). Removal of selenium from water with nanoscale zero-valent iron: mechanisms of intraparticle reduction of se(IV). *Water Research, 71*(34), 274–281.

Liu, A., Liu, J., Pan, B., & Zhang, W. X. (2014a). Formation of lepidocrocite (γ-FeOOH) from oxidation of nanoscale zero-valent iron (nZVI) in oxygenated water. *RSC Advances, 4*, 57377–57382.

Liu, A., Liu, J., & Zhang, W. X. (2015). Transformation and composition evolution of nanoscale zero valent iron (nZVI) synthesized by borohydride reduction in static water. *Chemosphere, 119*, 1068–1074.

Liu, F., Yang, J. H., Zuo, J., Ma, D., Gan, L., Xie, B., et al. (2014b). Graphene-supported nanoscale zero-valent iron: removal of phosphorus from aqueous solution and mechanistic study. *Journal of Environmental Sciences (China), 26*(8), 1751–1762.

Ma, X., Zhang, Z., & Wang, A. (2016). The transition of fly ash-based geopolymer gels into ordered structures and the effect on the compressive strength. *Construction and Building Materials, 104*, 25–33.

Minelli, M., Papa, E., Medri, V., Miccio, F., Benito, P., Doghieri, F., & Landi, E. (2018). Characterization of novel geopolymer – zeolite composites as solid adsorbents for CO_2 capture. *Chemical Engineering Journal, 341*, 505–515.

Mondal, M. K. (2009). Removal of Pb(II) ions from aqueous solution using activated tea waste: adsorption on a fixed-bed column. *Journal of Environmental Management, 90*(11), 3266–3271.

Oleksenko, L. P., Yatsimirsky, V. K., Telbiz, G. M., & Lutsenko, L. V. (2004). Adsorption and catalytic properties of co/ZSM-5

zeolite catalysts for CO oxidation. *Adsorption Science and Technology, 22*(7), 535–541.

Ravel, B., & Newville, M. (2005). ATHENA , ARTEMIS , HEPHAESTUS : data analysis for X-ray absorption spectroscopy using IFEFFIT. *Synchrotron Radiation, 12*, 537–541.

Sarret, G., Avoscan, L., Carrière, M., Collins, R., Geoffroy, N., Carrot, F., et al. (2005). Chemical forms of selenium in the metal-resistant bacterium. *Applied and Environmental Microbiology, 71*(5), 2331–2337.

Sheng, G., Hu, J., Li, H., Li, J., & Huang, Y. (2016). Enhanced sequestration of Cr(VI) by nanoscale zero-valent iron supported on layered double hydroxide by batch and XAFS study. *Chemosphere, 148*, 227–232.

Shirazi, E., Torabian, A., & Nabi-Bidhendi, G. (2013). Carbamazepine removal from groundwater: effectiveness of the TiO_2/UV, nanoparticulate zero-valent iron, and Fenton (NZVI/H_2O_2) processes. *Clean - Soil, Air, Water, 41*(11), 1062–1072.

Staicu, L. C., Morin-Crini, N., & Crini, G. (2017). Desulfurization: critical step towards enhanced selenium removal from industrial effluents. *Chemosphere, 172*, 111–119.

Suazo-Hernández, J., Sepúlveda, P., Manquián-Cerda, K., Ramírez-Tagle, R., Rubio, M. A., Bolan, N., et al. (2019). Synthesis and characterization of zeolite-based composites functionalized with nanoscale zero-valent iron for removing arsenic in the presence of selenium from water. *Journal of Hazardous Materials, 373*, 810–819.

Subramani, A., Cryer, E., Liu, L., Lehman, S., Ning, R. Y., & Jacangelo, J. G. (2012). Impact of intermediate concentrate softening on feed water recovery of reverse osmosis process during treatment of mining contaminated groundwater. *Separation and Purification Technology, 88*, 138–145.

Sun, Y. P., Li, X. Q., Zhang, W. X., & Wang, H. P. (2007). A method for the preparation of stable dispersion of zero-valent iron nanoparticles. *Colloids and Surfaces A: Physicochemical and Engineering Aspects, 308*, 60–66.

Tan, L. C., Nancharaiah, Y. V., Hullebusch, E. D. V., & Lens, P. N. L. (2016). Selenium: environmental significance, pollution, and biological treatment technologies. *Biotechnology Advances, 34*(5), 886–907.

Thuadaij, P., & Nuntiya, A. (2012). Effect of the SiO_2/Al_2O_3 ratio on the synthesis of Na-x zeolite from Mae Moh fly ash. *ScienceAsia, 38*(3), 295–300.

Tian, N., Zhou, Z., Tian, X., Yang, C., & Li, Y. (2017). Superior capability of $MgAl_2O_4$ for selenite removal from contaminated groundwater during its reconstruction of layered double hydroxides. *Separation and Purification Technology, 176*, 66–72.

Wan Ngah, W. S., Teong, L. C., Toh, R. H., & Hanafiah, M. A. K. M. (2013). Comparative study on adsorption and desorption of Cu(II) ions by three types of chitosan-zeolite composites. *Chemical Engineering Journal, 223*, 231–238.

Wang, P., Menzies, N. W., Lombi, E., McKenna, B. A., de Jonge, M. D., Paterson, D. J., et al. (2013). In situ speciation and distribution of toxic selenium in hydrated roots of cowpea. *Plant Physiology, 163*(1), 407–418.

Wdowin, M., Franus, W., & Panek, R. (2012). Preliminary results of usage possibilities of carbonate and zeolitic sorbents in CO_2 capture. *Fresenius Environmental Bulletin, 21*(12), 3726–3734.

Xi, Y., Sun, Z., Hreid, T., Ayoko, G. A., & Frost, R. L. (2014). Bisphenol A degradation enhanced by air bubbles via advanced oxidation using in situ generated ferrous ions from nano zero-valent iron/palygorskite composite materials. *Chemical Engineering Journal, 247*, 66–74.

Yamani, J. S., Lounsbury, A. W., & Zimmerman, J. B. (2014). Adsorption of selenite and selenate by nanocrystalline aluminum oxide, neat and impregnated in chitosan beads. *Water Research, 50*, 373–381.

Yao, G., Lei, J., Zhang, X., Sun, Z., Zheng, S., & Komarneni, S. (2018). Mechanism of zeolite X crystallization from diatomite. *Materials Research Bulletin, 107*, 132–138.

Zhang, G., Song, A., Duan, Y., & Zheng, S. (2018). Enhanced photocatalytic activity of TiO_2/zeolite composite for abatement of pollutants. *Microporous and Mesoporous Materials, 255*, 61–68.

Zhang, X., Lin, S., Chen, Z., Megharaj, M., & Naidu, R. (2011). Kaolinite-supported nanoscale zero-valent iron for removal of Pb^{2+} from aqueous solution: Reactivity, characterization and mechanism. *Water Research, 45*(11), 3481–3488.

Oxidation-adsorption of arsenite contaminated water over ceria nanorods

Journal:	*Desalination and Water Treatment*
Manuscript ID	TDWT-2019-1886.R1
Manuscript Type:	Original Paper
Date Submitted by the Author:	n/a
Complete List of Authors:	Suwannatrai, Suttikorn ; Khon Kaen University Yan, Dickson Y.S. ; Technological and Higher Education Institute of Hong Kong Phanthasri, Jakkapop ; Khon Kaen University, Environmental Engineering Khamdahsag, Pummarin ; Chulalongkorn University Wannapaiboon, Suttipong ; Synchrotron Light Research Institute Tanboonchuy, Visanu; Khon Kaen University, Environmental Engineering ; Khon Kaen University, Research Center for Environmental and Hazardous Substance Management (EHSM)
Keywords:	Adsorption, Arsenite, Ceria, Cerium oxide, Oxidation, Arsenic complexes

Response to Reviewers' Comments

Ms. Ref. No.: TDWT-2019-1886

Title: Oxidation-adsorption of arsenate contaminated water over ceria nanorods

Authors: Suttikorn Suwannatrai, Dickson Y.S. Yan, Jakkapop Phanthasri, Pummarin Khamdahsag, Suttipong Wannapaiboon, Visanu Tanboonchuy

---

The authors would like to appreciate all the valuable suggestions and comments from the reviewers. The revised version of the manuscript has been completed, according to the reviewers' comments. The revision is marked in the green highlight.

Review Comments to the Authors

In spite of the considerable interest for treatment of arsenic-rich water, this paper has some inaccuaracies that have to be revised before be accepted for publication. Here is given a listing of the main points to be considered:

1. First of all: as soon as in the Title, authors mencioned Oxidation-adsorption of arsenate. But in fact they only used Arsenite in the experiments.
   Response: As suggested, we have edited the title to be "Oxidation-adsorption of arsenite contaminated water over ceria nanorods", in line 1.

2. But I have noted that the 1st keyword is "adsorption", that is the useful information requested also in the title and the text. However, the 2nd and 3rd keyword are not necessary; to my opinion,'arsenic or arsenite complexes' should also be included within this listing.
   Response: As suggested, the 2nd and 3rd keyword (Arsenate, Arsenic) was replaced by "arsenic complexes", in line 32.

3. LINE 26: How is the As(III) oxidization to As(V) during the sorption process suggested that CeO2 had high potential to remove As(III) from contaminate water?
   Response: We have discussed it as presented in lines 298-302.

the As(III) on the surface of CeO_2 was partially oxidized to As(V), and then adsorbed onto CeO_2 at the experimental condition through two mechanisms [37] of surface complexation and redox reaction of CeO_2 to Ce_2O_3. As(III) was oxidized to As(V) by receiving electrons from the CeO_2 redox reaction and CeO_2 was reduced to Ce_2O_3 as a Ce^{4+} intermediate reaction product. This generated Ce_2O_3 which also oxidized As(III) to As(V) as shown in **Fig. 10.**

4. LINE 79: Mentions that As(V) stock solution was prepared, how ever in the section "Batch Experiments" Lines 108-109 indicate that only As (III) was used.
   Response: The sentence "and As(V) stock solution was prepared to form $Na_2HAsO_4.7H_2O$ (J.T. Baker)" was removed, as suggested, in lines 81-82.

5. LINES 108-109. mentions that Experiments were conducted to examine the kinetics and isotherms, as well as the effect of solution pH on As(III) removal, however the results show that only one pH was considerated to the arsenic removal process, while in line 172 indicate that in this experiments, pH of the solution did not affect arsenite removal.
   Response: The effect of pH was not done in this study. The words "as well as the effect of solution pH on As(III) removal." were removed, as suggested, in line 110.

6. LINE 117; Wich type of anionic resin was used to separated As(V) ?
   Response: The type of anionic resin for As(V) removal, anion-exchange cartridge (A502P, Purolite) as reference Phanthasri et al., (2018) [29], was added in the manuscript, in lines 118-120 and 398-400.
   As(V) was separated from the solution using an anionic resin-exchange cartridge (A502P, Purolite) as in our previous study [29].

7. LINES 167-168: Authors say that The pHpzc of CeO_2 is about 5.8, while the pH value during the adsorption experiment was 6-7; therefore, CeO_2 was uncharged BECAUSE the solution had a pH ≈ 6.0-6.1, BUT Figures 7 and 8 show pH = 6.14 and 6.46. Explain that...
   Response: More discussion was added, and "pH ≈ 6.0-6.1" was corrected to "6.0-6.50", in lines 170-174.

The pH value during the adsorption experiment was 6.0-6.50; therefore, a negative charge of the CeO_2 surface was presented. However, under different pH conditions, arsenic species may change to various forms. As(III) exists mainly as H_3AsO_3, a neutral species, when pH is less than 9.2 ($pKa_1 = 9.2$) [26]. Thus, in this experiment, the pH range of the solution used in this study is probably not playing a role with arsenite removal.

8. It is not clear how you calculated Arsenite Oxidation, because the Figure 6 Shows that the Arsenite Oxidation begin at 60 minutes, and the Figure 9 shows the XANES spectra before and after the arsenic removal, but in this Figure not indicate if the time is considering in the analyzed samples.

Response: We have added more details on how to measure and calculate the arsenite remained, in lines 118-123.

As(V) was separated from the solution using an anionic resin-exchange cartridge (A502P, Purolite) as in our previous study [29]. As(V) was retained in the cartridge while As(III) was allowed to pass through. The As(III) concentration was then analyzed by an inductively coupled plasma optical emission spectrometer (ICP-OES, PerkinElmer Optima 8000). As(V) concentration was obtained by subtracting the measured As(III) concentration from total arsenic concentration.

Besides, in part of XANES, the material was sampled and analyzed at 120 min of reaction, at which this condition was added, in line 264.

Notes from the Editorial office:

1. Please add detailed contact information (incl. emails) of ALL authors to the first page of your paper.

Response: Emails of all authors were added, as suggested.

2. English needs to be carefully checked and polished

Response: English of the whole manuscript was carefully checked and polished, as suggested.

3. Carefully check that all references are accurate and correctly numbered (one by one, please, in text and in the list, also in Table 2).

Response: All references in the text and the list were carefully checked, as suggested.

4. Consult our Instructions to Authors (on the website) for exact journal style of the references and correct accordingly. Also, do not use "et al" in the list of refs but write all author names.

Response: The references in the list were corrected to be in the journal style format, as suggested.

Oxidation-adsorption of arsenite contaminated water over ceria nanorods

Suttikorn Suwannatrai[a], Dickson Y.S. Yan[b], Jakkapop Phanthasri[a], Pummarin Khamdahsag[c], Suttipong Wannapaiboon[d], Visanu Tanboonchuy[a,e]*

[a] Department of Environmental Engineering, Faculty of Engineering, Khon Kaen University, Khon Kaen, 40002, Thailand, email: suttigon7@hotmail.com (S. Suwannatrai); email: jakkapop@kkumail.com (J. Phanthasri)

[b] Faculty of Science & Technology, The Technological and Higher Education Institute of Hong Kong, New Territories, Hong Kong, email: dicksonyan@vtc.edu.hk (D.S. Yan)

[c] Environmental Research Institute, Chulalongkorn University, Bangkok 10330, Thailand, email: pummarin.k@chula.ac.th (P. Khamdahsag)

[d] Synchrotron Light Research Institute (Public Organization), Nakhon Ratchasima 30000, Thailand, email: suttipong@slri.or.th (S. Wannapaiboon)

[e] Research Center for Environmental and Hazardous Substance Management (EHSM), Khon Kaen University, Khon Kaen 40002, Thailand, e-mail address: visanu@kku.ac.th (V. Tanboonchy)

*Corresponding author, e-mail address: visanu@kku.ac.th, Tel. +664-336-2140

Abstract

The dominant arsenic oxidation state in groundwater as As(III) is more difficult to remove than As(V). To achieve higher As(III) removal, ceria (CeO_2) nanorods characterized by BET, XRD, SEM, FTIR, and XAS were successfully used to combine oxidation and adsorption processes. Results showed

that when calcination temperature increased surface area decreased, whereas crystallite size increased. Batch experiments indicated that the arsenic removal process was accurately described by a pseudo-second-order kinetic model with maximum removal capacities of 21.27 mg/g. X-ray Absorption Near-Edge Structure (XANES) of the solid-phase confirmed that CeO_2 adsorbed As(III) with partial As(III) oxidization to As(V) on the surface. Further evidence of the mechanisms for As(III) removal was demonstrated by the hydroxyl group in the sorption and As(III) forming inner-sphere monodentate and bidentate complexes on the interface of the CeO_2 solid phase. As(III) oxidization to As(V) during the sorption process suggested that CeO_2 had high potential to remove As(III) from contaminated water.

Keywords: Adsorption; Arsenic complexes; Arsenite; Ceria; Cerium oxide; Oxidation

1. Introduction

Arsenic (As) contamination in groundwater is an issue of high concern because As is both toxic and carcinogenic. Long-term consumption of high arsenic-contaminated water may lead to cancer of the skin, lungs, liver, and black foot disease [1–4]. Countries affected by high arsenic contamination include Bangladesh, Cambodia, China, India, Nepal, Taiwan, and Thailand [5, 6]. Considering the health risks, the World Health Organization has set maximum concentration for arsenic in drinking water at 10 µg/L [7]. Arsenite (As(III)) and arsenate (As(V)) are the two major arsenic species in aqueous systems depending on redox and pH conditions [8]. As(III) exists in anaerobic underground water mainly as $HAsO_3^{2-}$, $H_2AsO_3^-$, and H_3AsO_3, while As(V) in the surface water is predominantly presented as H_2AsO^{4-}, $HAsO_3^{2-}$, and H_3AsO_4) [9, 10]. Ratios of As(III)/As(total) at depth of 30-40 m have been reported in aquifers in the range of 0.6-0.9 [11, 12]. This is a matter of great concern since As(III) is 60 times more toxic than As(V) [13].

As(III) exists in an uncharged form as H_3AsO_3 at the typical pH of water and removal of As(III) is more difficult than As(V). To achieve greater As(III) removal efficiency, treatment processes require pre-oxidation of As(III) to As(V). This leads to increased operational costs and also produces some secondary pollution problems.

Many technologies including injection of oxygen or ozone [14], the Fenton process [15, 16], biological oxidation [17, 18], photocatalytic oxidation [19, 20], and electro-oxidation [21], have been widely studied for the oxidation of As(III). However, each faces one or more limitations such as the addition of oxidants or catalysts, extra energy input, and separation of the added catalyst, while some oxidants may lead to the formation of toxic disinfection byproducts. Furthermore, the oxidized As(V) may be reduced to As(III) and become more mobile under certain conditions [12]. Therefore, new economical and cost-effective materials are required that can combine the oxidation and adsorption remediation processes as an efficient and effective method to remove As(III) without the need for pretreatment. Previous studies have shown that Fe(oxyhydr)oxides [22], Fe-sulfide [23], nano-iron/oyster shell composites [24], and zero-valent iron [25] are effective for As(III) removal.

Ceria (CeO_2), showed efficient arsenic removal over a pH range from 3 to 11 [26], particularly toward As(III) with a high content of hydroxyl groups suggested as responsible for its excellent performance. Moreover, despite the rare earth terminology, ceria and other cerium salts are cheap and show potential as cost-competitive materials. Ceria has a fluorite structure and is an important material with good mechanical, chemical, and thermal stability [27]. Ceria synthesized through a combined oxidation and adsorption process was successfully used to remove As(III) [28]; however, high calcination temperature was required which increased synthesis cost and impacted CeO_2 crystal characteristics such as pore size and surface hydroxy groups. Ceria synthesis at low calcination temperature for the uptake of

As(III), adsorption performance during high concentration As(III) uptake, and the mechanism of adsorption have yet to be studied and reported using advanced analytical tools.

Here, CeO_2 was prepared by a simple precipitation process with calcination in a furnace at different temperatures. The kinetic and isotherm of adsorbent with high sorption capacity for As(III) was prepared and used to remove As(III) from synthetic water. Sorption behaviors, especially sorption capacity, were investigated, and CeO_2 was characterized by X-ray powder diffraction (XRD), Brunauer, Emmett, and Teller (BET) technique, and point of zero charge (pH_{pzc}). The mode of As(III) sorption onto CeO_2 before and after processing is poorly documented. Our main goal was to better understand the cause of any changes in apparent surface reactivity by determining the nature of As surface complexes using X-ray Absorption Near-Edge Structure (XANES). Proposed mechanisms on the surface of CeO_2 were discussed.

2. Materials and methods

2.1. Materials

Chemical reagents used for CeO_2 synthesis included $Ce(NO_3)_3.6H_2O$ (99%) (Merck) and NaOH (Merck). The As(III) stock solution was prepared by dissolving $NaAsO_2$ (Merck). NaCl was also used in the ionic strength experiment. All chemical solutions were prepared with deionized water (18.2 MΩ Mill-Q).

2.2. Preparation of CeO_2

Ceria was synthesized by the hydrothermal method under autogenous pressure and used as the Ce^{3+} ion and OH^- ion precursors in all reactions performed toward the synthesis of pure CeO_2. In this study, 1:4 mole of Ce^{3+} and OH^- was rapidly dissolved in 100 mL deionized water. When the NaOH solution was added, the reaction started, and a white Ce(OH) precipitate was formed. The solution was

kept in an ambient environment with stirring for 30 min before heating at 110 °C for 6 h in a Teflon-lined stainless-steel autoclave. After cooling to room temperature, the precipitate was collected by centrifugation (5 min at 5,000 rpm) and washed with DI water several times to remove excess ionic remnants. Finally, aliquots of the precipitate were calcined in a furnace at different temperatures (105-550 °C) overnight.

2.3. Characterization of CeO_2

The crystal structure of CeO_2 was characterized by an X-ray Powder Diffractometer (XRD) (D8 Discover, Bruker AXS) using Bragg-Brentano geometry, equipped with a theta-theta goniometer system with a rotating sample holder. The XRD patterns were collected using Cu Kα radiation (λ = 0.1514 nm) at 40 kV and 40 mA with a scan range of 20-80°. Brunauer-Emmett-Teller (BET) specific surface area was measured by nitrogen adsorption-desorption isotherms (TriStar ll 3020, Micromeritics) to analyze the specific surface area of the CeO_2. A scanning electron microscope (SEM) (Hitachi, S-3000N) was used to analyze the surface structure and morphology of CeO_2. Prepared samples were analyzed by SEM at an acceleration of 15 kV. Functional group analysis was performed by a Fourier transform infrared spectrometer (FTIR) at a wave-number range of 400-4000 cm^{-1} (Tensor 27, Bruker). Surface chemical states of As on the CeO_2 surface and nature of Ce surface complexes were determined using As and Ce K-edge XANES with analysis at Beamline BL1.1 at the Synchrotron Light Research Institute (SLRI), Thailand. Reference compounds included Au^0 and V^0 foil, As(III) 5.0 mM, and As(V) 5.0 mM. All spectra were recorded in fluorescence and transmission mode using a 19-element Ge detector due to the low concentration of As.

2.4. Batch experiments

Experiments were conducted to examine the kinetics and isotherms. Experiments to determine the kinetics of the As(III) removal reaction with CeO_2 at room temperature were carried out by batch method. Here, 500 mL of As(III) solution of C_0 from 50 mg/L was mixed with 0.5 g of CeO_2 into a 600 mL beaker and agitated at 200 rpm using a speed adjustable agitator, with monitoring of pH and oxidation-reduction potential (ORP). The CeO_2 particles were separated by a syringe filter 0.45 μm and analyzed for residual arsenic concentration. To investigate isotherms, 50 mL of As(III) solution of C_0 (mg/L) ranging from 1.0 to 80.0 was mixed with 0.05 g of CeO_2 in a centrifugal tube, and then subjected to 50 rpm for 30 min before separating the CeO_2 particles using a syringe filter 0.45 μm.

After processing, the material was filtrated from solution using a 0.45 μm syringe filter, and As(V) was separated from the solution using an anionic resin-exchange cartridge (A502P, Purolite) as in our previous study [29]. As(V) was retained in the cartridge while As(III) was allowed to pass through. The As(III) concentration was then analyzed by an inductively coupled plasma optical emission spectrometer (ICP-OES, PerkinElmer Optima 8000). As(V) concentration was obtained by subtracting the measured As(III) concentration from total arsenic concentration.

3. Results and discussion

3.1. Characterization of CeO_2

The XRD analysis identified a single crystalline phase in the calcination products at the temperature range of 105-550 °C with CeO_2 presenting as a cubic fluorite-type structure. With increasing calcination temperature, the diffraction peaks narrowed as the crystallites grew and acquired a more ordered structure [30]. Fig. 1 shows X-ray diffractogram patterns of synthesized CeO_2. Five samples showed typical CeO_2 XRD patterns at around 2θ = 28.5, 33.0, 47.4, 56.3, 59.3, 69.6, 76.7, and 79.1

corresponding to the (111), (200), (220), (311), (222), (400), (331), and (240) crystalline planes, respectively of the pure cubic phase. All diffraction peaks indicated a ceria fluorite structure (JCPDS 00-034-0394). Pure phase CeO_2 was formed at a high calcination temperature of 550 °C, confirming the synthesis as similar to pure CeO_2.

The broadening of X-ray diffraction peaks provided a convenient method for measuring particle sizes. As crystallite size decreased, the width of the diffraction peaks increased. The average crystallite size was estimated using the Debye-Scherrer equation (Eq. (1)):

$$D = \frac{C\lambda}{\beta_{cos}\theta} \quad (1)$$

where *D* is the crystallite size, C is a numerical constant (0.9), λ is the wavelength of X-rays (CuKα radiation, λ = 1.514 Å), β is the effective peak broadening taken as the full width at half maximum (FWHM) (in radians), and *θ* is the diffraction angle for the peak. The Crystallite size of the particles was determined using the Debye-Scherrer formula. The XRD data revealed average sizes of CeO_2 as 9.96, 10.20, 10.71, 13.38, and 14.28 nm for products prepared at 105, 250, 350, 450, and 550 °C, respectively (**Fig. 1**). A previous report determined average crystallite size of CeO_2 prepared by thermal decomposition of cerous nitrate as 6.45 nm [31], while the increase of hydrothermal temperature led to the formation of nanocubes with narrower XRD diffraction peaks, indicating an incremental increase of mean crystallite size by up to 30-40 nm at 180 °C [32]. Moreover, particle size increase with elevating reaction temperature inferred that particle growth rate was predominant over the nucleation rate [33].

Specific surface area is an important parameter in the adsorption process. **Fig. 2**. shows that the BET surface area of CeO_2 decreased as calcination temperature increased [34]. Surface area reduced from 74.2 m^2/g to 41.1 m^2/g with the increase in calcination temperature from 105 to 550 °C, signaling an acceleration of crystallite growth in CeO_2-550 °C. Images of SEM surface morphology micrographs for

three different calcination temperatures are shown in **Fig. 3(a)** At a temperature of 150 °C, ceria nanorods are mainly formed with a very rough and uneven surface containing numerous pits and pores [32]. However, the surface of CeO_2 dried at 105 °C showed highly crystalline nanorods evenly distributed over the surface. When the temperature increased, the appearance of crystalline rods on the surface of CeO_2 decreased as presented in **Fig. 3(b), (c),** and **(d)**. This occurred because of rising calcination temperature in the range 300-550 °C caused increased particle size growth. Moreover, CeO_2 calcined above 1,070 °C had the same density (=99.8%) and particle size increased rapidly to 48 nm [35].

Relative reductions of surface area and morphology for CeO_2 material at higher calcination temperatures resulting from the rapid growth of crystals were attributed to shrinkage and agglomeration to larger clusters of metallic oxide particles [34]. Decrease of surface area and larger pores resulted in sintering, leading to reduced activity of the adsorbent due to pore elimination and formation of dense solid. Hence, a large surface area is important for high adsorption performance.

The point of zero charge (pH_{pzc}) of CeO_2 can be evaluated by determining the pH value at which the zeta potential is zero. The pH_{pzc} is used to qualitatively assess the polarity of the adsorbent surface charge[36]. At pH < pH_{pzc}, the adsorbent has a positive surface charge and can act as an anion exchanger, while at pH > pH_{pzc} the surface charge of the adsorbent is negative and beneficial for adsorbing cations. The pH_{pzc} of CeO_2 is presented in **Fig. 4** at about 5.8. The pH value during the adsorption experiment was 6.0-6.50; therefore, a negative charge of the CeO_2 surface was presented. However, under different pH conditions, arsenic species may change to various forms. As(III) exists mainly as H_3AsO_3, a neutral species, when pH is less than 9.2 (pKa_1 = 9.2) [26]. Thus, in this experiment, the pH range of the solution used in this study is probably not playing a role in arsenite removal.

The FTIR spectra of CeO_2 prepared by the simple precipitation process with synthesis at low calcination temperature are shown in **Fig. 5**. Bands at 545 and 750 cm^{-1} are due to Ce-O stretching vibration, while bands at 1379 and 1539 cm^{-1} result from C-O stretching vibration. The band at 1065 cm^{-1} is due to -NH stretching vibration, and the band at 3412 cm^{-1} is caused by O-H bond vibrations of water absorbed from moisture. These variable peaks revealed that functional groups such as -OH and C-OH were involved in the adsorption reaction of As(III) ions on CeO_2 [37, 38]. Similar results were also deduced for possible adsorption mechanisms for As(III) removal by CeO_2 and these are discussed later.

3.2. Arsenite removal capacity testing

3.2.1. Effect of calcination temperature on As(III) removal

The effect of initial calcination temperature on the rate of As(III) removal is shown in **Fig. 6** as a plot of dimensionless concentration versus time for calcination temperature ranging from 105 to 550 °C. Removal capacity between different calcined products varied from 8.75, 8.94, 7.88, 8.38, and 7.59 mg/g for 105, 250, 350, 450, and 550 °C, respectively. The CeO_2 material calcined at 250 °C showed maximum removal capacity, confirming that the release of residual chemisorbed water and organic residues as NO_3 [39] inhibited arsenic removal. Reaction by-products occurring during the CeO_2 synthesis process are shown as Eqs. (2)-(6).

$$4NaOH_{(s)} \longrightarrow 4Na^{+}_{(aq)} + 4OH^{-}_{(aq)} \quad (2)$$

$$Ce(NO_3)_3 \cdot 6H_2O_{(s)} \longrightarrow Ce^{3+}_{(aq)} + 3NO_3^{-}{}_{(aq)} + 6H_2O_{(aq)} \quad (3)$$

$$Ce^{3+}_{(aq)} + 4OH^{-}_{(aq)} + xH_2O_{(aq)} \longrightarrow Ce(OH)_4 \cdot xH_2O_{(s)} \quad (4)$$

$$Ce(OH)_4 \cdot xH_2O_{(s)} \longrightarrow Ce(OH)_{4(s)} + xH_2O_{(g)} \quad (5)$$

$$Ce(OH)_{4(g)} \xrightarrow{\text{Heating}} CeO_{2(s)} + 2H_2O_{(g)} \quad (6)$$

These reactions are consistent with the crystal size and surface area of CeO_2. The removal capacity of CeO_2 depends on various factors such as surface area, porosity, and surface morphology. However, the chemical characteristics of CeO_2 change on heating. The O/Ce ratio decreased with increasing calcination temperature, while the abundance of O-Ce^{3+} and hydroxyl groups also decreased at higher calcination temperatures [30].

The calcination temperature of CeO_2 at 250 °C gave the highest removal capacity. As(III) uptake capacities were determined as a function of time to deduce an optimal contact time for adsorption of As(III) on CeO_2. The amount of As(III) on each CeO_2 sample was calculated by the difference between As(III) content in influent solution and effluent solution expressed as a percentage (C/C_0).

Variation of C/C_0 as a function of time is shown in **Fig. 6**. The significantly higher arsenic removal efficiency was obtained in the first 10 min. The concentration of As(III) in aqueous solution reduced from 42.29 mg/L to 14.68 mg/L in 10 min, revealing that As(III) was quickly removed by CeO_2, and then decreased steadily with increasing reaction time. The optimal time required for CeO_2 to achieve maximum removal efficiency (77%) was 30 min. However, As(III) began to change to As(V) at about 60 min, and this continuously increased to 120 min, indicating that CeO_2 oxidized As(III) to As(V). Additionally, As(III) in aqueous solution was partially oxidized because As(V) was detected in the As(III)-CeO_2 system as shown in **Fig. 7**.

Ceria is often considered an active catalytic support material due to its excellent reducibility, oxygen transport properties [40], and as a catalyst for oxidation processes[41], resulting in a transfer of electrons to As(III) on the surface of CeO_2. When As(III) receives oxygen electrons it oxidizes to As(V)

according to the CeO_2 redox equation. The analysis demonstrated that As(III) in aqueous solution was partially oxidized to As(V), while As(V) did not reduce to As(III). Similar results were also deduced from arsenic speciation on the solid-phase interface by XANES, and these are discussed as follows.

3.2.2. Kinetic model and isotherm analysis of As(III) removal

A pseudo-second-order kinetic model was fitted to the experimental data of arsenic removal by CeO_2 to better understand the reaction kinetics. The expression of this model is presented as Eq. (7):

$$\frac{t}{q_t} = \frac{1}{k2q_e^2} + \frac{t}{q_e} \quad (7)$$

where q_t (mg/g) is the CeO_2 amount at time t (min), q_e (mg/g) is the maximum adsorption capacity, and k_2 (g/mg.min) is the rate constant. Applicability of the pseudo-second-order kinetic model is quantified by the squared correlation coefficient (R^2). **Table 1** shows the kinetic parameters obtained from the data fitted in **Fig. 8(a)**. The high value of R^2 (0.9989) indicated that a pseudo-second-order kinetic model fitted the kinetics data accurately. Thus, it can be concluded that arsenic adsorption onto CeO_2 is driven by chemisorption involving valence forces through the sharing or exchange of electrons between CeO_2 and As(III) [26, 42].

Two important adsorption isotherms, namely Langmuir and Freundlich, were fitted to the experimental data. Adsorption capacities of CeO_2 on As(III) were investigated by an equilibrium adsorption isotherm study as demonstrated in **Fig. 8(b)**. Adsorption data were fitted with Langmuir and Freundlich isotherms as Eqs. (8)-(9), respectively:

$$q_e = K_F C_e^{1/n} \quad (8)$$

$$q_e = \frac{q_{max} K_L C_e}{1 + K_L C_e} \quad (9)$$

where q_e (mg/g) is the amount of the adsorbate adsorbed at the adsorbent, C_e (mg/L) is the equilibrium concentration of the adsorbate in solution, q_{max} (mg/g) is the maximum amount of the adsorbate adsorbed at the adsorbent at equilibrium time, K_L (L/mg) is a constant related to the heat of adsorption, K_F (mg/g)(L/mg)$^{1/n}$ is related to the adsorption capacity of the adsorbent of the adsorbent, and $1/n$ is a constant known as the heterogeneity factor that is related to the surface heterogeneity.

Compared to the Langmuir isotherm, the Freundlich isotherm plot resulted in a good fit with experimental data as evidenced in **Fig. 8(b)**. The Freundlich isotherm constants are shown in **Table 1**, and the linear correlation coefficients for As(III) of the plot were good. **Fig. 8(b)** shows the sorption isotherm in terms of As(III) in the solid phase as a function of equilibrium As(III) concentration in the leachate. The Freundlich isotherm fitted well for adsorption of As(III) on CeO_2. The 'n' values of As(III) were observed to be more than the value 1, indicating that adsorption was favorable for As(III). However, the main assumption of the Freundlich model describes sorption on heterogeneous surfaces with sorption sites and heterogeneous energy distribution [43]. It also describes reversible adsorption which is not restricted to the formation of a monolayer [44].

Table 2 presents a comparison between our prepared CeO_2 and previously reported sorbents for As(III) sorption. Results demonstrated that CeO_2 outperformed many other sorbents. The high capacity indicated that our prepared CeO_2 was very effective for As(III) removal and achieved the aim of finding new materials that can combine oxidation and adsorption processes as an efficient method since As(III) is more toxic and more difficult to remove from water than As(V).

3.3. Adsorption mechanism and As(III) interaction on CeO_2

The XANES spectra are very sensitive to the oxidation state of the adsorbed atom; therefore, the As and Ce K-edge XANES spectra can indicate the oxidation state of elements that occur on the interface of materials between, before, and after arsenic removal at 120 min. Fig. 9(a) presents the normalized As K-edge XANES spectra of samples before and after the adsorption processes at different calcination temperatures (250 and 550 °C). The XANES features of the starting material were typical of As(III) and As(V) standard as 11870.3 and 11873.3 eV, respectively. The As K-edge of both CeO_2 samples (250 and 550 °C) showed that spectrum properties matched with the As(III) standard, while characteristics of the spectrum represented As(V) on the CeO_2 surface were similar to the As(V) standards. The As K-edge XANES data identified a combination of As(III) and traces of As(V) on the surface of CeO_2 since As(III) can be oxidized to As(V) on the surface of CeO_2 to a certain extent through the redox reaction of Ce^{4+}. Dahle et al. noted that CeO_2 had a particularly high oxygen storage capacity; when coupled with its ease of transition between trivalent and tetravalent states and its high natural abundance, this makes CeO_2 an excellent choice as a catalyst [45].

The Ce L_{III}-edge was also examined by XANES after the adsorption processes. The results are shown in **Fig. 9(b)**, along with spectra for $Ce(NO_3)_36H_2O$ (reference for Ce^{3+}) at 5726.19 eV and CeO_2 powder (reference for Ce^{4+}) with double peaks at 5730.59 eV and 5737.40 eV, respectively. Before and after adsorption processes identified combinations of Ce^{4+} and slight Ce^{3+} due to the transmission of electrons between Ce^{4+} and As(III), resulting in the change of As(III) on the surface of CeO_2 as shown in Eq. (9).

$$2CeO_2 + 3H_3AsO_3 \longrightarrow H_3AsO_4 + 2CeAsO_3 + H_2O \quad (9)$$

As(III) was oxidized to As(V) by receiving electrons from the CeO_2 redox reaction, and CeO_2 was reduced to Ce_2O_3 as a Ce^{4+} intermediate reaction product. This generated Ce_2O_3 which also oxidized

As(III) to As(V). Results of Ce L_3-edge XANES spectra analysis inferred that CeO_2 played the role of an arsenic species adsorbent and acted as an oxidant.

The XANES analysis suggested possible adsorption mechanisms for As(III) removal by CeO_2 as shown in **Fig. 10**. Our results and existing reports concurred with As(III) adsorption on the hydroxyl group bond on the surface (Ce-OH) after the reaction. This was consistent with FTIR analysis revealing that functional groups such as -OH and C-OH were involved in the adsorption of As(III) ions on CeO_2 [37, 41, 46] due to the formation of highly hydroxylated As(III) complexes via the reaction between Ce-OH and As-OH. The fast adsorption kinetics in this study indicated a chemisorption mechanism [26]. Thus, we suggest that As(III) adsorption occurs by forming inner-sphere complexes at the hydroxy group on the CeO_2 surface. Adsorption behavior that is unaffected by pH provides evidence for inner-sphere complexation, whereby the As(III) species exchanges with -OH groups that are directly coordinated to the CeO_2 surface. Possible monodentate and bidentate surface complexes allow CeO_2 to adsorb As(III) through a rapid and efficient process [26].

Based on an analysis using relationships between contact time and the XANES method, the As(III) on the surface of CeO_2 was partially oxidized to As(V), and then adsorbed onto CeO_2 at the experimental condition through two mechanisms [37] of surface complexation and redox reaction of CeO_2 to Ce_2O_3. As(III) was oxidized to As(V) by receiving electrons from the CeO_2 redox reaction and CeO_2 was reduced to Ce_2O_3 as a Ce^{4+} intermediate reaction product. This generated Ce_2O_3 which also oxidized As(III) to As(V) as shown in **Fig. 10**. Thus, the main mechanism of As(III) adsorption was as follows: (i) complexation was conducted between hydroxyl groups on CeO_2 to form monodentate and bidentate complexes, and (ii) As(III) was oxidized to As(V) by redox reaction [37].

4. Conclusions

Our results indicated that CeO_2 was successfully synthesized following a simple precipitation process, with low-temperature calcination to adsorb As(III) in aqueous solution. Ceria being calcined at 250 °C showed maximum adsorption capacities of As(III) reaching 21.27 mg/g. The adsorption behavior of As(III) was well fitted to the Freundlich isotherm and a pseudo-second-order model. Analysis of XANES spectra demonstrated that oxidation states of Ce and As occurred on the interface of materials between, before, and after arsenic removal. The As(III) adsorption mechanisms as complexation were conducted between hydroxyl groups and redox transformation between As(III) and CeO_2. Our results suggested that economical synthesis of CeO_2 offers potential as an efficient method for removal of As(III) from polluted water by adsorption.

Acknowledgments

This work was financially supported by the Research and Technology transfer affairs of Khon Kaen University, The Thailand Research Fund (MRG6180196), and Office of the Higher Education Commission. The authors also would like to acknowledge the Synchrotron Light Research Institute (Public Organization).

References

[1] D. Liu, S. Deng, A. Maimaiti, B. Wang, J. Huang, Y. Wang and G. Yu, As(III) and As(V) adsorption on nanocomposite of hydrated zirconium oxide coated carbon nanotubes, J. Colloid and Interface Science., 511 (2018) 277-284.

[2] E. Şık, E. Demirbas, A.Y. Goren, M.S. Oncel and M. Kobya, Arsenite and arsenate removals from groundwater by electrocoagulation using iron ball anodes: Influence of operating parameters, J.

Water Process Eng., 18 (2017) 83-91.

[3] L. Al-Eryani, S. Waigel, V. Jala, S.F. Jenkins and J.C. States, Cell cycle pathway dysregulation in human keratinocytes during chronic exposure to low arsenite, Toxicol. Appl. Pharmacol., 331 (2017) 130-134.

[4] Z. Cheng, F. Fu, D.D. Dionysiou and B. Tang, Adsorption , oxidation , and reduction behavior of arsenic in the removal of aqueous As(III) by mesoporous Fe/Al bimetallic particles, Water Res., 96 (2016) 22-31.

[5] B.R.C. Vieira, A.M.A. Pintor, R.A.R. Boaventura, C.M.S. Botelho and S.C.R. Santos, Arsenic removal from water using iron-coated seaweeds, J. Environ Manage., 192 (2017) 224-233.

[6] A. Sarkar and B. Paul, The global menace of arsenic and its conventional remediation-A critical review, Chemosphere., 158 (2016) 37-49.

[7] L. Lin, W. Qiu, D. Wang, Q. Huang, Z. Song and H.W. Chau, Arsenic removal in aqueous solution by a novel Fe-Mn modified biochar composite : Characterization and mechanism, Ecotoxic Environ Safety., 144 (2017) 514-521.

[8] A. Adra, G. Morin, G. Ona-Nguema and J. Brest, Arsenate and arsenite adsorption onto Al-containing ferrihydrites. Implications for arsenic immobilization after neutralization of acid mine drainage, Appl. Geochem., 64 (2015) 2-9.

[9] S. Martinez-Vargas, A.I. Martínez, E.E. Hernandez-Beteta, O.F. Mijangos-Ricardez, V. Vazquez-Hipolito, C. Patino-Carachure and J. Lopez-Luna, As(III) and As(V) adsorption on manganese ferrite nanoparticles, J. Mol Struct., 1154 (2018) 524-534.

[10] Y. Xiong, Q. Tong, W. Shan, Z. Xing, Y. Wang, S. Wen and Z. Lou, Arsenic transformation and adsorption by iron hydroxide/manganese dioxide doped straw activated carbon, Appl. Surf. Sci.,

416 (2017) 618-627.

[11] K. Gupta, S. Bhattacharya, D. Nandi, A. Maity, A. Mukhopadhyay, D.J. Chattopadhyay, N.R. Ray, P. Sen and U.C. Ghosh, Arsenic(III) sorption on nanostructured cerium incorporated manganese oxide (NCMO): A physical insight into the mechanistic pathway, J. Colloid Interface Sci., 377 (2012) 269-276.

[12] Y.M. Zheng, L. Yu, D.Wu and J.P.Chen, Removal of arsenite from aqueous solution by a zirconia nanoparticle, Chem. Eng. J., 188 (2012) 15-22.

[13] K. Shehzad, C. Xie, J. He, X. Cai, W. Xu and J. Liu, Facile synthesis of novel calcined magnetic orange peel composites for efficient removal of arsenite through simultaneous oxidation and adsorption, J. Colloid Interface Sci., 511 (2018) 155-164.

[14] S. Khuntia, S.K. Majumder and P. Ghosh, Oxidation of As(III) to As (V) using ozone microbubbles, Chemosphere., 97 (2014) 120–124.

[15] J. Qin, H. Li and C. Lin, Fenton process-affected transformation of roxarsone in paddy rice soils: Effects on plant growth and arsenic accumulation in rice grain, Ecotoxicol. Environ. Saf., 130 (2016) 4-10.

[16] J. Qin, Y. Li, M. Feng, H. Li and C. Lin, Fenton reagent reduces the level of arsenic in paddy rice grain, Geoderma., 307 (2017) 73-80.

[17] S. Crognale, B. Casentini, S. Amalfitano, S. Fazi, M. Petruccioli and S. Rossetti, As(III) oxidation in biofilters by using native groundwater microorganisms, Sci. Total Environ Biol., 651 (2019) 93-102.

[18] Y. Sun, G. Liu and Y. Cai, Thiolated arsenicals in arsenic metabolism: Occurrence, formation, and biological implications, J. Environ., Sci. 49 (2016) 59-73.

[19] A. Samad, M. Furukawa, H. Katsumata, T. Suzuki and S. Kaneco, Photocatalytic oxidation and simultaneous removal of arsenite with CuO/ZnO photocatalyst, J. Photochem. Photobiol. A Chem., 325 (2016) 97-103.

[20] K.B. Fontana, G.G. Lenzi, E.C.R. Seára and E. S. Chaves, Comparision of photocatalysis and photolysis processes for arsenic oxidation in water, Ecotoxicol. Environ. Saf., 151 (2018) 127-131.

[21] X. Zhao, B. Zhang, H. Liu and J. Qu, Removal of arsenite by simultaneous electro-oxidation and electro-coagulation process, J. Hazard. Mater., 184 (2010) 472-476.

[22] X. Han, J. Song, Y.L. Li, S.Y. Jia, W.H. Wang, F.G. Huang and S.H. Wu, As(III) removal and speciation of Fe(Oxyhydr)oxides during simultaneous oxidation of As(III) and Fe(II), Chemosphere., 147 (2016) 337-344.

[23] X. Xie, Y. Liu, K. Pi, C. Liu, J. Li, M. Duan and Y. Wang, In situ Fe-sulfide coating for arsenic removal under reducing conditions, J. Hydrol., 534 (2016) 42-49.

[24] L. Fan, S. Zhang, X. Zhang, H. Zhou, Z. Lu and S. Wang, Removal of arsenic from simulation wastewater using nano-iron/oyster shell composites, J. Environ. Manage., 156 (2015) 109-114.

[25] O. Eljamal, K. Sasaki, S. Tsuruyama and T. Hirajima, Kinetic Model of Arsenic Sorption onto Zero-Valent Iron (ZVI), Water Qual Expo Health., 2 (2011) 125-132.

[26] R. Li, Q. Li, S. Gao and J. Ku, Exceptional arsenic adsorption performance of hydrous cerium oxide nanoparticles : Part A. Adsorption capacity and mechanism, Chem. Eng. J., 186 (2012) 127–135.

[27] T. Arii, T. Taguchi, A. Kishi, M. Ogawa and Y. Sawada, Thermal decomposition of cerium (III) acetate studied with sample-controlled thermogravimetric-mass spectrometry (SCTG-MS), J. Eur. Ceram. Soc., 22 (2002) 2283-2289.

[28] Y. Yu, C. Zhang, L. Yang and J.P. Chen, Cerium oxide modified activated carbon as an efficient and effective adsorbent for the rapid uptake of arsenate and arsenite: material development and study of performance and mechanisms, Chem. Eng. J., 315 (2016) 630-638.

[29] J. Phanthasri, P. Khamdahasag, P. Jutaporn, K. Sorachoti, K. Wantala and V. Tanboonchuy, Enhancement of arsenite removal using manganese oxide coupled with iron (III) trimesic, appl. Surf. sci., 427 (2018) 545-552.

[30] P. Janos, P. Kuran, M. Kormunda, V. Stengl, T.M. Grygar, M. Dosek, M. Stastny, J. Ederer, V. Pilarova and L. Vrtoch, Cerium dioxide as a new reactive sorbent for fast degradation of parathion methyl and some other organophosphates, J. Rare Earths., 32 (2014) 360-370.

[31] E.K. Goharshadi, S. Samiee and P. Nancarrow, Fabrication of cerium oxide nanoparticles : Characterization and optical properties, J. Colloid Interface Sci., 356 (2011) 473-480.

[32] L.T. Murciano, A. Gilbank, B, Puertolas, T. Garcia, B. Solsona and D. Chadwick, Shape-dependency activity of nanostructured CeO_2 in the total oxidation of polycyclic aromatic hydrocarbons, Appl. Catal. B Environ., 133 (2013) 116-122.

[33] H.L. Chen and H.Y. Chang, Synthesis of nanocrystalline cerium oxide particles by the precipitation method, Ceram. Int., 31 (2005) 795-802.

[34] S.J.M. Rosid, W.A.W.A. Bakar and R. Ali, Characterization and modelling optimization on methanation activity using Box-Behnken design through cerium doped catalysts, J. Clean. Prod., 170 (2018) 278-287.

[35] W.E. Mahmoud and A. Faidah, Microwave assisted hydrothermal synthesis of engineered cerium oxide nanopowders, J. Eur. Ceram. Soc., 32 (2012) 3537-3541.

[36] S. Cheng, L. Zhang, A. Ma, H. Xia, J. Peng, C. Li and J. Shu, Comparison of activated carbon and

iron/cerium modified activated carbon to remove methylene blue from wastewater, J. Environ. Sci., 5 (2017) 1-11.

[37] L. Zhang, T. Zhu, X. Liu and W. Zhang, Simultaneous oxidation and adsorption of As(III) from water by cerium modified chitosan ultrafine nanobiosorbent, J. Hazard. Mater., 308 (2016) 1-10.

[38] J. Chen, J. Wang, G. Zhang, Q. Wu and D. Wang, Facile fabrication of nanostructured cerium-manganese binary oxide for enhanced arsenite removal from water, Chem. Eng. J., 334 (2018) 1518-1526.

[39] J.J. Ketzial and A.S. Nesaraj, Synthesis of CeO_2 nanoparticles by chemical precipitation and the effect of a surfactant on the distribution of particle sizes, J. Ceram. Process. Res., 12 (2011) 74-79.

[40] D. Vovchok, C.J. Guild, S. Dissanayake, J. Llorca, E. Stavitski, Z. Liu, R.M. Palomino, Y. Li, A.I. Frenkel, J.A. Rodriquez, S.L. Suib and S.D. Senanayake, In Situ Characterization of Mesoporous Co/CeO_2 Catalysts for the High-Temperature Water-Gas Shift, J. Phys. Chem. C., 122 (2018) 8998-9008.

[41] D.R. Mullins, The surface chemistry of cerium oxide, Surf. Sci. Rep., 70 (2015) 42-85.

[42] C. Feng, C. Aldrich, J.J. Eksteen and D.W. M. Arrigan, Removal of arsenic from gold cyanidation process waters by use of cerium- based magnetic adsorbents, Miner. Eng., 122 (2018) 84-90.

[43] J. Chen, J. Wang, G. Zhang, Q. Wu and D. Wang, Facile fabrication of nanostructured cerium-manganese binary oxide for enhanced arsenite removal from water, Chem. Eng. J., 334 (2018) 1518-1526.

[44] M. Attari, S.S. Bukhari, H. Kazemian and S. Rohani, A low-cost adsorbent from coal fly ash for mercury removal from industrial wastewater, J. Environ. Chem. Eng., 5 (2017) 391–399.

[45] Y.H. Huang, Y.J. Shih and F.J. Cheng, Novel $KMnO_4$-modified iron oxide for effective arsenite

removal, J. Hazard. mater., 198 (2011):1-6.

[46] D. Dickson, G. Liu and Y. Cai, Adsorption kinetics and isotherms of arsenite and arsenate on hematite nanoparticles and aggregates, J. Environ Manage., 186 (2017) 261-267.

[47] D.A. Almasri, T. Rhadfi, M.A. Atieh, G. McKay and S. Ahzi, High performance hydroxyiron modified montmorillonite nanoclay adsorbent for arsenite removal, Chem Eng J., 335 (2018) 1-12.

[48] H. Zongliang, T. Senlin and N. Ping, Adsorption of arsenate and arsenite from aqueous solutions by cerium-loaded cation exchange resin, J. Rare Earths., 30 (2012) 563-572.

[49] C. Zeng,C. Nguyen, S. Boitano, J.A. Field, F. Shadman and R. Sierra-Alvarez,. Cerium dioxide (CeO_2) nanoparticles decrease arsenite (As(III)) cytotoxicity to 16HBE14o- human bronchial epithelial cells, Environ Res., 164 (2018) :452-458.

[50] J.T. Dahle and Y. Arai, Environmental Geochemistry of Cerium : Applications and Toxicology of Cerium Oxide Nanoparticles, Int. J. Environ. Res. Public Health., 12 (2015) 1253-1278.

[51] B.M. Harish, M.P. Rajeeva, V.S. Chaturmukha, S. Suresha, H.S. Jayanna, S. Yallappa and A.R. Lammani, Influence of zinc on the structural and electrical properties of cerium oxide nanoparticles, Mater. Today Proc., 5 (2018) 3070-3077.

Fig. 1. XRD patterns of CeO_2 synthesized at different calcination temperatures of 105 to 550 °C.

Fig. 2. Characteristics of CeO_2 from XRD patterns and BET analysis.

Fig. 3. SEM images of CeO_2 at difference calcination temperatures: (a) 105 °C, (b) 250 °C, (c) 350 °C, and (d) 550 °C.

Fig. 4. Zeta potential of CeO_2 samples under various pH values.

Fig. 5. FTIR spectra of CeO_2 at 250 °C calcination temperature.

Fig. 6. Adsorption of As(III) onto various calcined CeO_2 samples as a function of calcination temperature (°C) (experiment conditions: CeO_2 = 0.1g and As(III) = 50 mg/L).

Fig. 7. Relationship between contact time and residual arsenic under CeO_2 at room temperature (experimental conditions: CeO_2 = 0.5 g, As(III) = 50 mg/L, and pH = 6.14).

Fig. 8. Adsorption kinetic (a), and equilibrium adsorption isotherm of As(III) (b) on CeO_2 with high equilibrium concentration (experimental conditions: CeO_2 = 0.5 g, As(III) = 50 mg/L, and pH = 6.46).

Fig. 9. Normalized XANES spectra for (a) As K-edge XANES spectra, and (b) Ce L_3-edge XANES spectra.

Fig. 10. Schematic diagram for the proposed mechanism of As(III) adsorption and As(III) oxidation to As(V) on the surface of CeO_2.

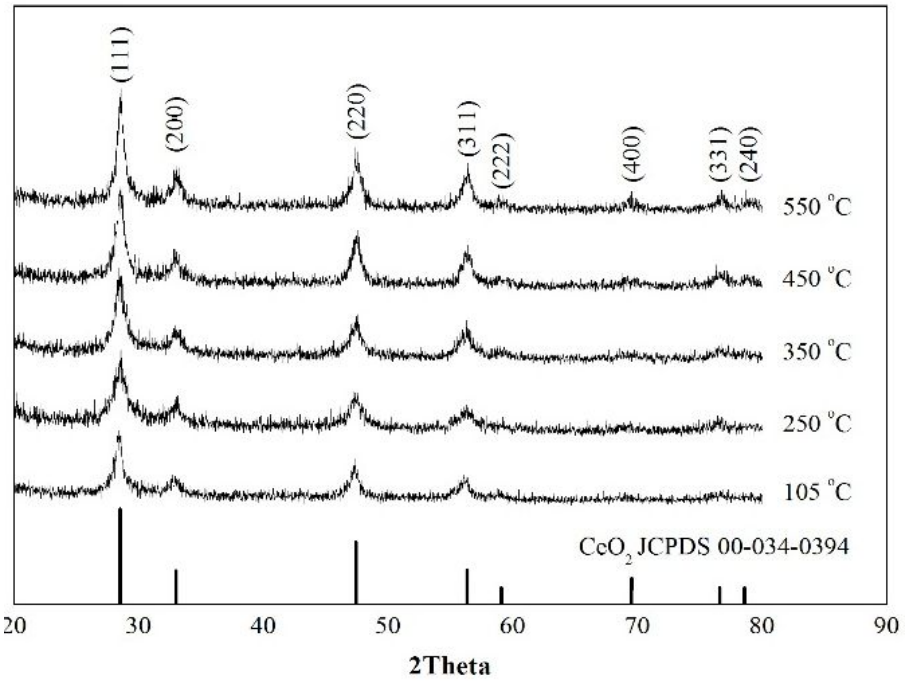

Fig. 1. XRD patterns of CeO_2 synthesized at different calcination temperatures of 105 to 550 °C.

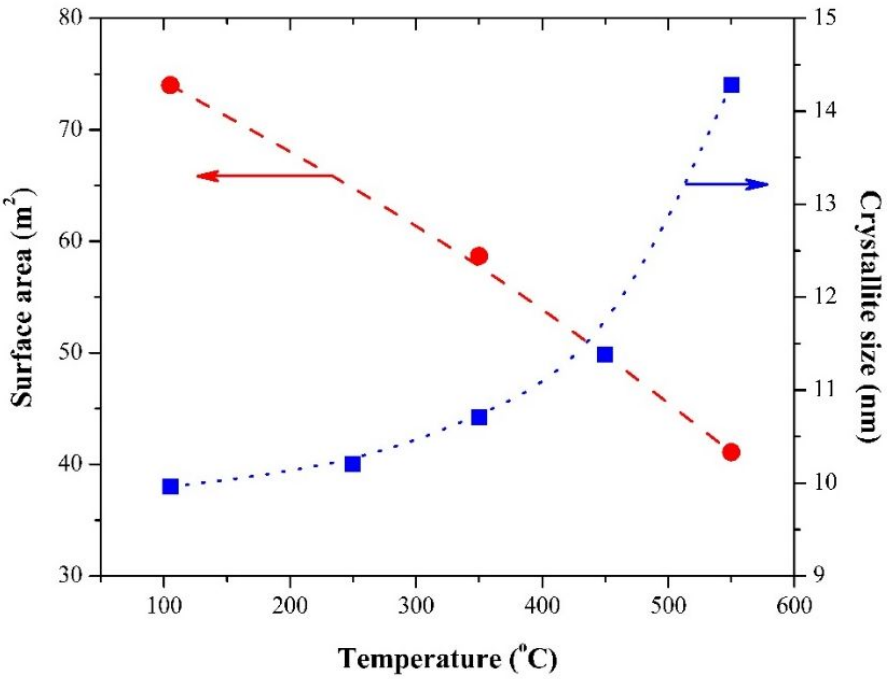

Fig. 2. Characteristics of CeO_2 from XRD patterns and BET analysis.

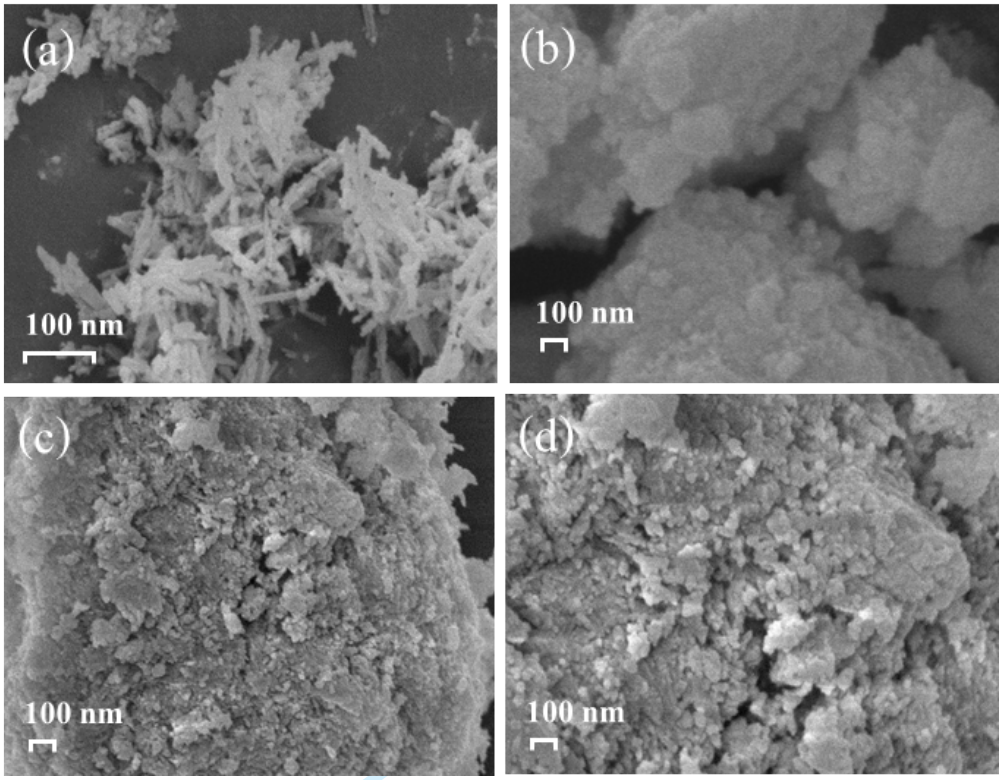

Fig. 3. SEM images of CeO_2 at difference calcination temperatures: (a) 105 °C, (b) 250 °C, (c) 350 °C, and (d) 550 °C.

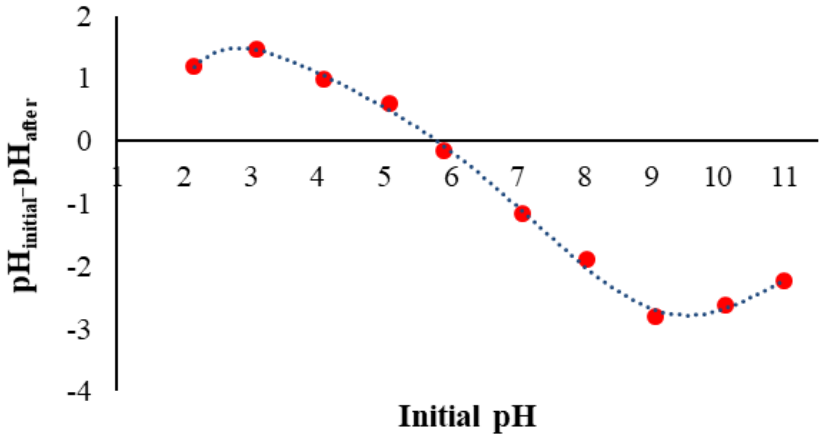

Fig. 4. Zeta potential of CeO_2 samples under various pH values.

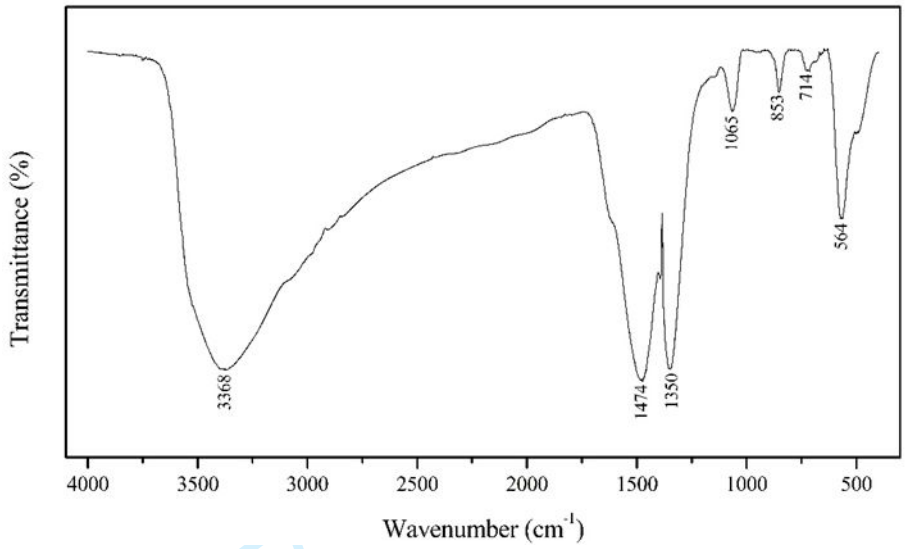

Fig. 5. FTIR spectra of CeO_2 at 250 °C calcination temperature.

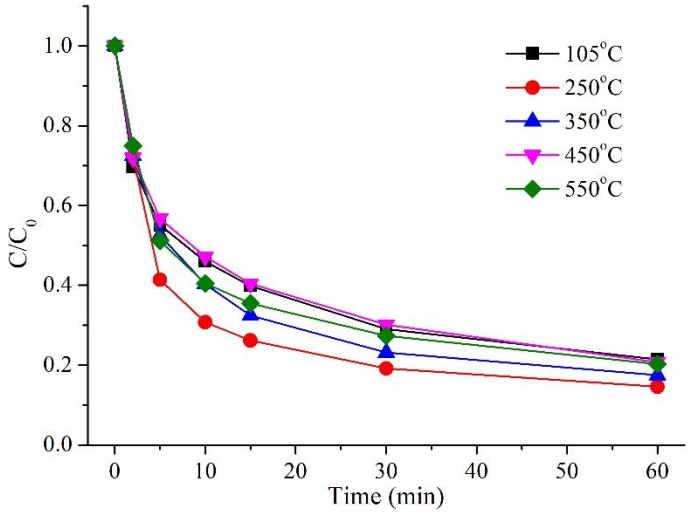

Fig. 6. Adsorption of As(III) onto various calcined CeO_2 samples as a function of calcination temperature (°C) (experiment conditions: CeO_2 = 0.1g and As(III) = 50 mg/L).

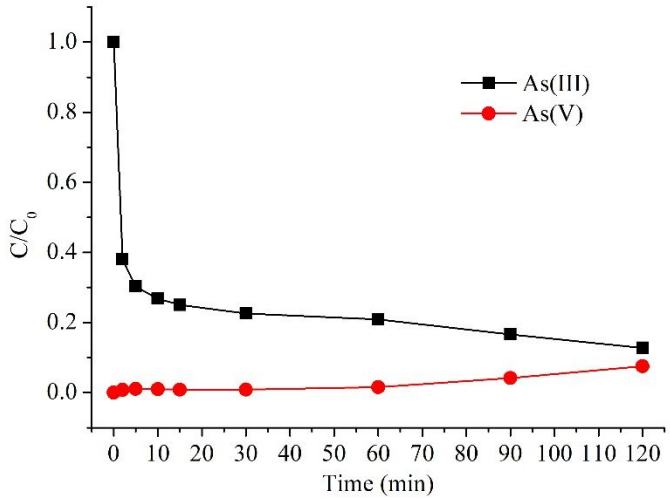

Fig. 7. Relationship between contact time and residual arsenic under CeO_2 at room temperature (experimental conditions: CeO_2 = 0.5 g, As(III) = 50 mg/L, and pH = 6.14).

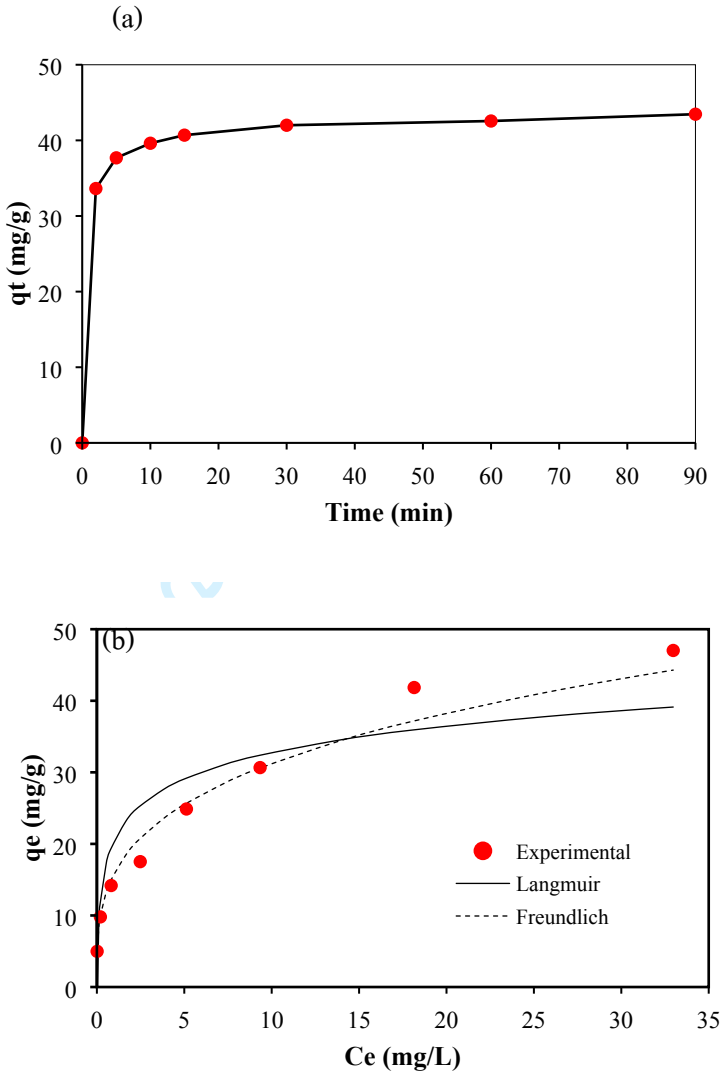

Fig. 8. Adsorption kinetic (a), and equilibrium adsorption isotherm of As(III) (b) on CeO_2 with high equilibrium concentration (experimental conditions: CeO_2 = 0.5 g, As(III) = 50 mg/L, and pH = 6.46).

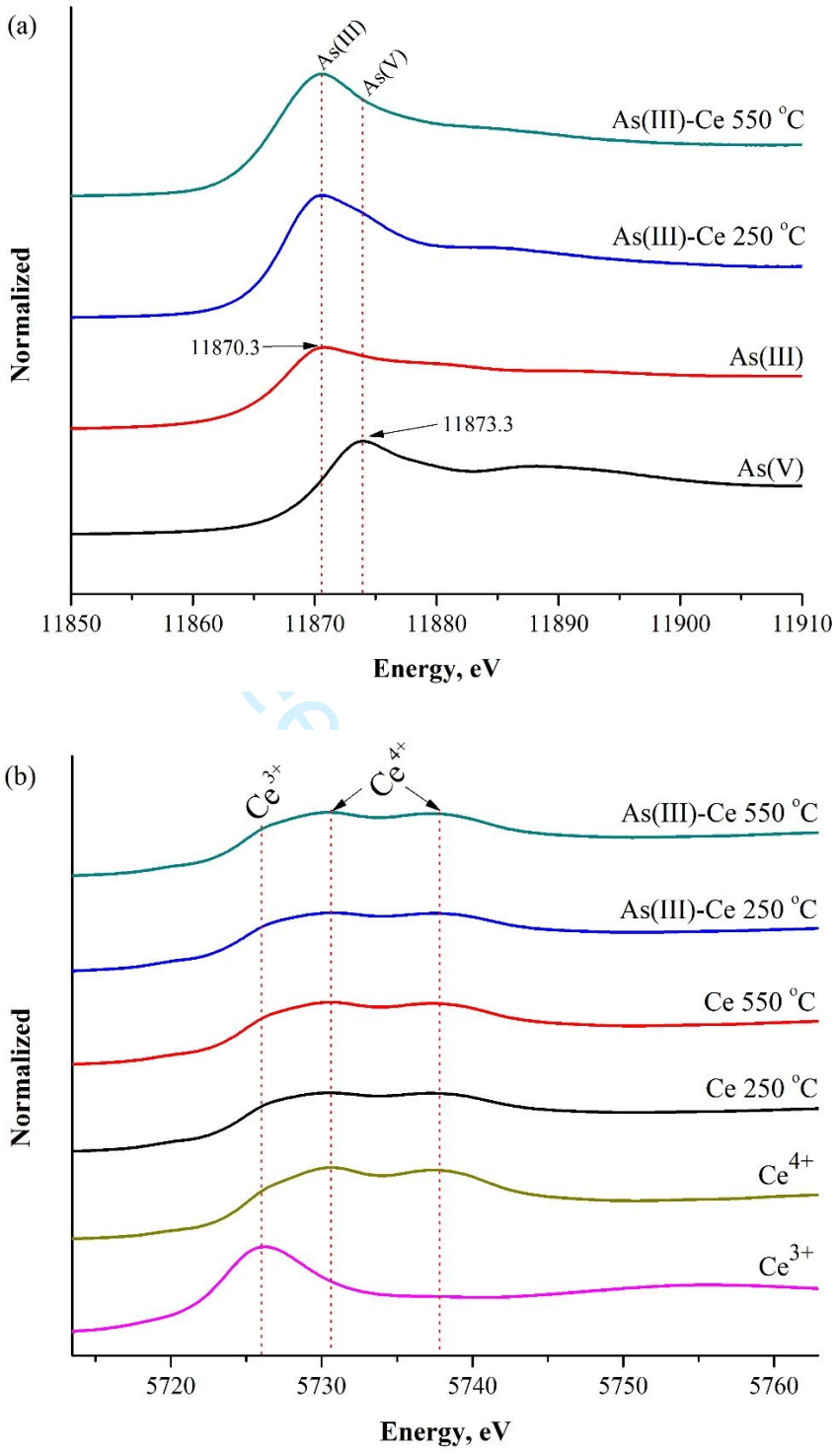

Fig. 9. Normalized XANES spectra for (a) As K-edge XANES spectra, and (b) Ce L_3-edge XANES spectra

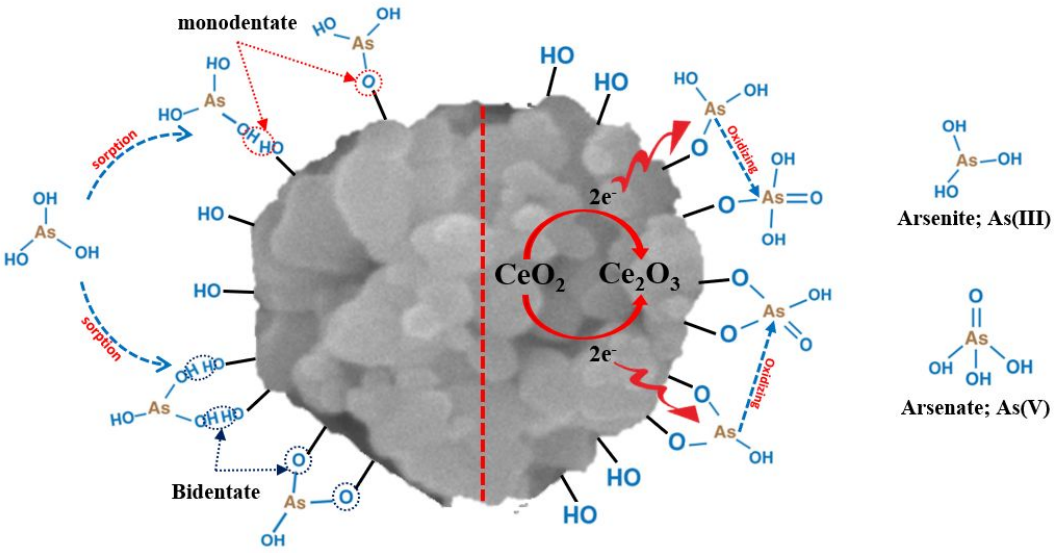

Fig. 10. Schematic diagram for the proposed mechanism of As(III) adsorption and As(III) oxidation to As(V) on the surface of CeO_2.

Table 1 Adsorption kinetics and equilibrium adsorption isotherm fitting parameters for As(III) onto CeO_2.

Table 2 Comparison of adsorption capacity of arsenite by various adsorbents.

Table 1 Adsorption kinetics and equilibrium adsorption isotherm fitting parameters for As(III) onto CeO_2.

Adsorption kinetic (Pseudo-second-order rate kinetic)			
Initial time (min)	15	30	60
q_e (mg/g)	0.086	0.081	0.079
k_2 (g/(mg.min))	41.152	42.373	42.918
$h = k_2 q_e^2$ (mg/(g.min)	0.304	0.278	0.267
R^2	0.9989	0.9994	0.9998
Equilibrium adsorption isotherm			
Freundlich	K_F (mg/g)(L/mg)$^{1/n}$		15.909
	n		3.414
	R^2		0.9856
Langmuir	q_{max} (mg/g)		21.277
	K_L (L/mg)		21.364
	R^2		0.8424

Table 2 Comparison of adsorption capacity of arsenite by various adsorbents.

Adsorbent	Surface area (m^2/g)	Solution pH	Sorbate	Sorption capacity (mg/g)	Reference no.
MnBT-4	229	3	As(III)	27.4	[45]
Hematite NPS	-	7-8	As(III)	4.122	[46]
HyFe-MMT	277-355	9-7	As(III)	3.854	[47]
Ce-Loaded cationic resin	-	5-6	As(III), As(V)	2.25, 1.02	[48]
Ce-CNB	-	8	As(III)	57.5	[37]
NCMO	116.96	6-8	As(III)	34.89	[11]
CeO_2 NPS	-	7.0	As(III)	20.21	[49]
CeO_2 LCT	≈ 67.5	5.8-6.3	As(III)	21.27	This study

Chemical Engineering Journal

Continuous fixed-bed column studies of arsenite removal via oxidation and adsorption co-processes

--Manuscript Draft--

Manuscript Number:	
Article Type:	Research Paper
Section/Category:	Environmental Chemical Engineering
Keywords:	arsenic; K-OMS2; Fe-BTC; Adsorption; oxidation; fixed-bed column
Corresponding Author:	Visanu Tanboonchuy, Ph.D. Khon Kaen University Khon Kaen, Ampor Mueang THAILAND
First Author:	Pongnapa Poompang
Order of Authors:	Pongnapa Poompang
	Nichapa Supannafai
	Jakkapop Phanthasri
	Pummarin Khamdahsag
	Dickson Y.S. Yan
	Visanu Tanboonchuy, Ph.D.
Abstract:	This study aimed to remove arsenite (As(III)) via co-processes of oxidation and adsorption in a continuous flow system using fixed-bed columns. Manganese oxide octahedral molecular sieve (K-OMS2) and iron-based metal-organic framework (Fe-BTC) were applied as an oxidizer and an adsorbent, respectively. Before use in the column, K-OMS2 and Fe-BTC powders were coated on the ceramic ball through the mechanical orbital shaking technique with each of K-OMS2 and Fe-BTC to ceramic ball ratios of 1 to 50. Then, they were characterized by X-ray diffraction (XRD) and X-ray absorption near-edge structure (XANES) techniques. Finally, the As(III) and arsenate (As(V)) removal efficiency in every single fixed-bed column of K-OMS2 (coated) and Fe-BTC (coated), respectively, and the two columns combined were conducted. From the results, in the single-column test, K-OMS2 (coated) maintained good efficiency to oxidize As(III) for a three-round-use cycle with lower than groundwater standard of Mn and K leaching. In the Fe-BTC (coated) column test, adsorption kinetics fit well with the Yoon-Nelson model having the maximum adsorption capacity of 52.60 mg/g and Fe leaching of 0.23 mg/L. With two columns combined, the system enabled to remove total As for 60% within 2,200 min.
Suggested Reviewers:	Chih-Hsiang Liao, Ph.D Prof., Chia-Nan University of Pharmacy and Science chliao.taiwan@gmail.com His researches relate with arsenic treatment
	Irene M.C. Lo, Ph.D. Prof., Hong Kong University of Science and Technology cemclo@ust.hk Her researches relate wastewater treatment.
	David L. Sedlak, Ph.D. Prof., University of California Berkeley Art Museum and Pacific Film Archive sedlak@ce.berkeley.edu His research relate with groundwater treatment and arsenic treatment.
	Haoran Dong, Ph.D. Prof., Hunan University dhrrhd@163.com His study about pollutant treatment, wastewater treatment.
Opposed Reviewers:	

May 5th, 2020

Visanu Tanboonchuy, Ph.D.
Department of Environmental Engineering
Khon Kaen University
Email: visanu@kku.ac.th
Telephone no +66 4336 2140

Dear Editor-in-chief,

Attached please find the manuscript submitted to your journal, Chemical Engineering Journal, for possible publication. The manuscript title is *"Continuous fixed-bed column studies of arsenite removal via oxidation and adsorption co-processes"*. We submitted our manuscript to your journal due to the fact that Chemical Engineering Journal is a prestigious international journal of original research that can improve our understanding of materials that pose to public health and the environment. It will help us to spread our research and knowledge to the world easily.

Our research proposed a new technic for arsenite (As(III)) removal by oxidation and adsorption co-processes. In addition, this study also characterizes the materials by advance technic such as X-ray Diffraction (XRD) and X-ray Absorption Near-Edge Structure (XANES) technique to reveal the mechanism of the arsenic removal process.

Thank you in advance for your reviewing work. We are looking forward to your reply.

Best regards,
Visanu Tanboonchuy

Suggested Reviewers

1. Chih-Hsiang Liao Ph.D.

Professor, Environmental Resources Management, Chia-Nan University of Pharmacy and Science,Taiwan

Email: chliao.taiwan@gmail.com

2 Irene M.C. Lo Ph.D.

Professor, Civil and Environmental Engineering, Hong Kong University of Science and Technology

Email: cemclo@ust.hk

3. David L. Sedlak Ph.D.

Professor, Civil and Environmental Engineering, University of California Berkeley

Email: sedlak@ce.berkeley.edu

4. Haoran Dong

College of Environmental Science and Engineering, Hunan University, Changsha, 410082, China

Email: dhrrhd@163.com

Graphic Abstract

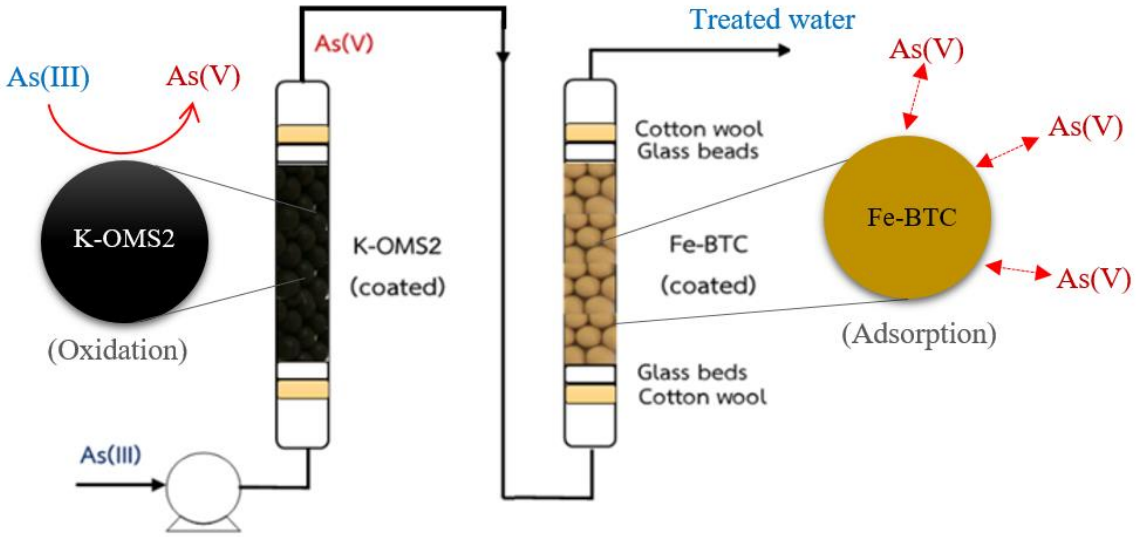

Highlights

- A simultaneous oxidation for As(III) by K-OMS2 and adsorption of As(V) by Fe-BTC were proposed as a new technic to enhance the performance of arsenic removal.
- The K-OMS2 was mainly considered as the oxidizing agent which be able to reuse several times.
- The coating technique of K-OMS2 and Fe-BTC in this study was concluded to have the potential to practically apply in an up scaled arsenic treatment approach

Continuous fixed-bed column studies of arsenite removal via oxidation and adsorption co-processes

Pongnapa Poompang[a], Nichapa Supannafai[b], Jakkapop Phanthasri[a], Pummarin Khamdahsag[c,d], Dickson Y.S. Yan[e], Visanu Tanboonchuy[a,d,f*]

[a]Department of Environmental Engineering, Faculty of Engineering, Khon Kaen University, Khon Kaen 40002, Thailand

[b]Interdisciplinary Program of Environmental Science, Graduate School, Chulalongkorn University, Thaialnd

[c]Environmental Research Institute, Chulalongkorn University, Bangkok 10330, Thailand

[d]Center of Excellence on Hazardous Substance Management (HSM), Chulalongkorn University, Bangkok 10330, Thailand

[e]Faculty of Science & Technology, The Technological and Higher Education Institute of Hong Kong, New Territories, Hong Kong

[f]Research Center for Environmental and Hazardous Substance Management (EHSM), Khon Kaen University, Khon Kaen 40002, Thailand

Corresponding author: visanu@kku.ac.th

Abstract

This study aimed to remove arsenite (As(III)) via co-processes of oxidation and adsorption in a continuous flow system using fixed-bed columns. Manganese oxide octahedral molecular sieve (K-OMS2) and iron-based metal-organic framework (Fe-BTC) were applied as an oxidizer and an adsorbent, respectively. Before use in the column, K-OMS2 and Fe-BTC powders were coated on the ceramic ball through the mechanical orbital shaking technique with each of K-OMS2 and Fe-BTC to ceramic ball ratios of 1 to 50. Then, they were characterized by X-ray diffraction (XRD) and X-ray absorption near-edge structure (XANES) techniques. Finally, the As(III) and arsenate (As(V)) removal efficiency in every single fixed-bed column of K-OMS2 (coated) and Fe-BTC (coated), respectively, and the two columns combined were conducted. From the results, in the single-column test, K-OMS2 (coated) maintained good efficiency to oxidize As(III) for a three-round-use cycle with lower than groundwater standard of Mn and K leaching. In the Fe-BTC (coated) column test, adsorption kinetics fit well with the Yoon-Nelson model having the maximum adsorption capacity of 52.60 mg/g and Fe leaching of 0.23 mg/L. With two columns combined, the system enabled to remove total As for 60% within 2,200 min.

Keywords: arsenic; arsenite; K-OMS2; Fe-BTC; adsorption; oxidation; fixed-bed column

1. Introduction

Contamination of water with arsenic (As) poses a major health risk to people such as two types of toxicity, acute and subacute. Acute arsenic poisoning requiring rapid medical attention usually occurs through the ingestion of contaminated food or water. Subacute arsenic toxic mainly involve the respiratory, gastrointestinal, cardiovascular, nervous, and hematopoietic system [1]. It also causes kidney disease, diabetes, skin cancer, etc. [2, 3]. The degree of As mobility in water is under the control of the oxidation state of As and pH of water [4]. In the environment, As is found in several oxidation states (-3, 0, +3, and +5), but it is approximately found in form of trivalent arsenite (As(III)) and pentavalent arsenate (As(V)) in natural waters [5 ,6]. Besides, the occurred species of As(III): H_3AsO_3, $H_2AsO_3^{1-}$, and $HAsO_3^{2-}$, and As(V): H_3AsO_4, $H_2AsO_4^{1-}$ and, $HAsO_4^{2-}$, is dependent on the pH of water [7] leading the neutral charge H_3AsO_3, which is the species of As(III), present in the common pH groundwater. This is the reason why removal of As(III) in water is quite difficult with conventional methods undergoing electrostatic force when compared to removal of As(V) which is also less toxic than As(III). The current recommended limit of As in drinking water standards by the World Health Organization (WHO) is 10 µg/L [8]. In Southeast Asia, there are still many countries faced with problems of arsenic-contamination in water such as Vietnam, Laos, Cambodia, Myanmar, and Thailand [9]. The problem concerning arsenic is As(III) in groundwater because As(III) causes arduous precipitation with other minerals [10] as well as difficult ion-exchange and adsorption over materials [11].

Remediation of arsenic contamination can be performed by many methods, for instance, oxidation, coagulation-flocculation, adsorption, ion exchange, etc. [12, 13]. However, most of the As(III) removal treatment initially relies on oxidation by converting As(III) to As(V) using an oxidizing agent followed by precipitation, ion-exchange, or adsorption of As(V) [6, 14-16]

According to our previous study in a batch system, As(III) was successfully treated by using the manganese oxide octahedral molecular sieve (K-OMS2) and iron-based metal-organic framework (Fe-BTC) in powder form [16]. The K-OMS2 could oxidize As(III) well in a temperature range of 30–60°C. The Fe-BTC gave a maximum adsorption capacity of As(V) at 76.34 mg/g described by the Langmuir isotherm model. The whole removal process of As(III) with an initial concentration of 5 mg/L was completed within 60 min after the K-OMS2 and Fe-BTC powders were simultaneously introduced into the same batch solution indicating excellent co-working of the two materials. The K-OMS2 plays an important role in the field of catalytic oxidation for As(III) transformation. It is a type of manganese oxide with 2×2 tunnels and MnO_6 octahedral chains in one dimensional 4.6 Å × 4.6 Å structure. K-OMS2 has a mixed oxidation state of Mn^{2+}, Mn^{3+}, and Mn^{4+} ions in the octahedral framework. This material is highly porous, various pore structures, non-toxic, and environmentally friendly [16, 17-19]. At the same time, the Fe-BTC is one of the metal-organic frameworks (MOFs) in which metal ions act as coordination centers and link together with a variety of organic bridging ligands. With the characteristics of Fe-BTC having high surface areas and porosity, it was paid attention to applying to remove As(V) from aqueous solutions [20-22]

Although the K-OMS2 and Fe-BTC powders showed the desirable performance, they were practically inconvenient in a continuous flow system for water treatment. In this work, we, therefore, investigate the continuous fixed-bed column studies of As(III) removal via oxidation and adsorption co-processes of the K-OMS2 and Fe-BTC coated on ceramic balls. Some characteristics such as crystallinity and oxidation states of the materials coated on ceramic balls were reported in this study. Besides, the dynamic behavior of the continuous fixed-bed columns was described in terms of a breakthrough curve. The reuse of the oxidation column was tested. Thomas and Yoon-Nelson models were applied to predict the performance in the adsorption column. A combination of oxidation column and adsorption column for total

As removal was also conducted as well as leaching of manganese (Mn), potassium (K), and iron (Fe).

2. Materials and Methods

2.1 Materials

As(V) source in this study was from disodium hydrogen arsenate heptahydrate ($Na_2HAsO_4 \cdot 7H_2O$, 98%, Sigma-Aldrich), and As(III) was from sodium arsenite ($NaAsO_2$, 98%, Sigma-Aldrich). Manganese(II) acetate tetrahydrate ($Mn(CH_3COO)_2 \cdot 4H_2O$, 99%, ACROS Organics) potassium permanganate ($KMnO_4$, 99%, CARLO ERBA), and acetic acid (CH_3COOH, 99.8%, Merck) were used as starting materials of K-OMS2 powder synthesis. Iron(III) chloride hexahydrate ($FeCl_3 \cdot 6H_2O$, 99%, QRëC), 1,3,5-benzene tricarboxylic acid ($C_9H_6O_6$, 95%, Sigma-Aldrich) were used as starting materials of Fe-BTC powder synthesis. A ceramic ball with a diameter size of 4 mm (Al_2O_3 68.50%, SiO_2 28%, and others 3.5%, BPF 05) was used as a support material in the coating process. Other chemicals used in this study were laboratory grade.

2.2 Preparation and Characterization of K-OMS2 (coated) and Fe-BTC (coated)

The K-OMS2 and Fe-BTC powders were synthesized followed by methods described in our previous report [16]. For K-OMS2 powder synthesis, a potassium permanganate solution (0.25M, 40 mL) was mixed with manganese acetate tetrahydrate solution (0.33M, 40 mL). The pH of the solution was adjusted to an acidic condition (pH ≥ 3.5) by using acetic acid and stirred well for 1 h. The mixture was transferred to an autoclave for hydrothermal processing at 100°C for 3 h. Then, a black slurry was obtained and washed with deionized (DI) water to retain pH = 7. The black precursor was dried at 100°C for 3 h. Finally, the black powder of K-OMS2 was obtained. For Fe-BTC powder synthesis, iron(III) chloride hexahydrate solution

(1 M, 75 mL) mixed with a 1,3,5-benzene tricarboxylic acid solution (1M in ethanol, 75 mL). The mixture was transferred to an autoclave for hydrothermal processing at 100°C for 24 h. Then, an orange jelly-like substance was obtained and washed with DI water to retain pH = 7. The orange precursor was dried at 120°C for 4 h. Finally, the orange powder of Fe-BTC was obtained.

To prepare the K-OMS2 and Fe-BTC coated on ceramic balls, so-called K-OMS2 (coated) and Fe-BTC (coated), respectively, the preparation procedure was restricted by optimal conditions of coating from our previous work [23 – 25]. Firstly, the starting materials in the weight ratio of the K-OMS2 powder or the Fe-BTC powders to the ceramic balls of 1 to 50 were introduced to a 2,000-mL-beaker. It was then transferred and set on an orbital shaker to perform the coating via the mechanical orbital shaking technique at 160 rpm for 24 h. Then, the coated materials were dried at 120°C for 24 h. Finally, the K-OMS2 (coated) and Fe-BTC (coated) were ready for characterization and packing in the continuous fixed-bed columns.

The K-OMS2 powder, Fe-BTC powder, K-OMS2 (coated), and Fe-BTC (coated) were characterized to determine crystallinity using an X-ray Diffractometer (XRD) (D8 Discover, Bruker AXS) with a Cu Kα radiation (= 0.1514 nm) at 40 mA, an increment of 0.02°/step, a scan speed of 0.1 s/step, and 40 kV. The scan range was 10–80° for K-OMS2 and 1–40° for Fe-BTC at 25°C. Besides, the x-ray absorption near edge structure (XANES) spectroscopy technique was conducted over the spent K-OMS2 powder, and the standards of As(III) from sodium arsenite, and As(V) from disodium hydrogen arsenate heptahydrate. The XANES was performed at Beamline 1.1: Multiple X-ray techniques, the Synchrotron Light Research Institute (public organization) located in Nakhon Ratchasima, Thailand. The Athena software was used to analyze the XANES spectra of the spent K-OMS2 powder and the standards.

2.3 Continuous Fixed-Bed Column Experiment

The continuous fixed-bed column experiment was divided into three parts including 1) arsenite oxidation over K-OMS2 (coated) in a single continuous fixed-bed column, 2) arsenate adsorption over Fe-BTC (coated) in a single continuous fixed-bed column, and 3) total arsenic removal over K-OMS2 (coated) and Fe-BTC (coated) in combined continuous fixed-bed columns. Firstly, the continuous fixed-bed columns for K-OMS2 (coated) and Fe-BTC (coated) were vertically set using a 35 cm long borosilicate glass tube with an inner diameter of 2 cm and connected both ends with the silicone tubes. The inlet at the bottom of the column was driven by a peristaltic pump to control flowrate at 5 and 10 mL/min, and the outlet was the top of the column. Their configurations were supposed to retain water leveling neatly contacted with the cross-section's material in the column and avoid the flowrate with gravity force. Then, the K-OMS2 (coated) and Fe-BTC (coated) were separately loaded into the individual columns at a bed-length of 10, 15, and 20 cm by closing the top and bottom os the packed ones with 2-cm-bed-lengths of cotton wool and glass beads as shown in Figure 1(a) and 1(b). At the same time, 1 mg/L of disodium hydrogen arsenate heptahydrate solution and 1 mg/L of sodium arsenite solution was prepared. Next, the working efficiency test in each column was performed at room temperature of approximately 27±1°C under the experimental conditions in Table 1.

As(III) and As(V) concentration as well as leaching elements; manganese (Mn), potassium (K), and iron (Fe) were measured using an inductively coupled plasma optical emission spectrometer (ICP-OES) (PlasmaQuant PQ 9000 Elite, Analyticjena). A strong base anion exchange resin (Amberjet 4200 chloride form, Sigma-Aldrich) was used to separate the As(III) and As(V) before measuring the As(III) remained after passing through the K-OMS2 (coated) column. Besides, the three-round use cycle of the K-OMS2 (coated) column was

examined. The breakthrough capacity was calculated for only Fe-BTC (coated) single column using Equation (1).

Breakthrough capacity (mg/g) = [initial concentration (mg/L) × breakthrough time (min) × flow rate (mL/min) × 10^{-3}] / adsorbent weight (g) (1)

2.4 Sorption Kinetic Calculation using Thomas Model and Yoon-Nelson Model

Thomas model and Yoon-Nelson model have been proposed in the literature for calculating adsorption efficiency, modeling adsorption breakthrough curves, and describing the adsorption behavior in columns [26]. Based on experimental conditions I, II, and III, breakthrough curves data of As(V) adsorption over Fe-BTC (coated) in the single continuous fixed-bed column were fit with the linear equations of Thomas model and Yoon-Nelson model as given in Equations (2) and (3), respectively.

$$\ln\left(\frac{C}{C_0}-1\right)=\frac{K_T q_0 M}{Q}-\frac{K_T C_0 V}{Q} \quad (2)$$

Where C_0 = As(V) initial or inlet concentration (mg/L); C = As(V) final or effluent concentration (mg/L); K_T = the Thomas rate constant (mL/min/mg); Q = the flow rate (mL/min); q_0 = the maximum adsorption capacity (mg/g); V = the effluent volume (mL); M = adsorbent weight (g). The constants K_T and q_0 can be obtained from the intercepts and the slopes of linear plots of $\ln(C_0/C)$-1 versus V.

$$\ln\left(\frac{C}{C_0-C}\right)=K_{YN}t-K_{YN}\tau \quad (3)$$

Where K_{YN} = Yoon-Nelson rate constant (L/min); t = sampling time (min); τ = the time required for 50 % adsorbate breakthrough (min); q_0 = adsorption capacity (mg/g). The linearized equation plots were ln(C/C_0-C)) versus t.

3. Results and Discussion

3.1 K-OMS2 (coated) and Fe-BTC (coated) Characteristics

The XRD technique was applied in this study to check the crystalline structure and phases of the coated material compared to the bare powders since they were probably changed after the coating via mechanical orbital shaking. The XRD patterns of the K-OMS2 powder and K-OMS2 (coated) are shown in Figure 2(a), which revealed the identical XRD peaks of the powder's one with cryptomelane, KMn_8O_{16} (JCPDS 29-1020) and manganese dioxide, ∂-Mn_2O (JCPDS 44-0141) as similar as in our earlier report and the other reports [16, 27-30]. The peaks insisted at 12.6, 18.1, 28.7, 37.5, 41.8, 49.7, 56.0, 60.2, 65.4, and 69.5° corresponding to (110), (200), (310), (211), (301), (411), (600), (521), (002), and (741) reflection planes [16, 17, 30]. This crystallinity was formed during the hydrothermal process [31]. Besides, the K-OMS2 presented the broad XRD peak which meant to the lower crystallinity and larger crystalline size [32]. For the K-OMS2 (coated), their identical XRD peaks were quite unclear with very low intensity at planes (200), (211), (411), and (521) but remaining together with the identical peak of the corundum phase, ∂-Al_2O_3 (JCPDS 83-2080) from the ceramic ball using as the supporter. This disclosure might due to the thin layer as well as ununiform distribution coating of the K-OMS2 on the ceramic ball resulting in the low peak intensity and the corundum phase appearance from the X-ray penetration.

The XRD patterns of Fe-BTC and Fe-BTC (coated) are shown in Figure 1(b). It revealed the crystalline structure of Fe-BTC powder at 10.7, 23.5, and 27.4° related to other studies [16, 22, 33, 34] while the XRD peaks of Fe-BTC (coated) were difficult to identify but expected being still enabled to adsorb As(V) in case of amorphous structure. However, the

phases of akaganeite, Fe+3O(OH) (JCPDS 34-1266), hematite, Fe_2O_3 (JCPDS 85-0987), and corundum, ∂-Al_2O_3 (JCPDS 83-2080) XRD peak of Fe-BTC (coated) was found in the XRD peaks of Fe-BTC (coated).

The XANES spectra of the spent K-OMS2 powder, and the standards of As(III), and As(V) are presented in Figure 3. This investigation was aimed at the mechanisms related to As(III) removal over the K-OMS2 (coated). Noted that the spent K-OMS2 powder was used instead of the spent K-OMS2 (coated) since the limitation of sample preparation for the XANES measurement. The edge shape varied between both the spent K-OMS2 powder, as an experimental sample, and As(III), and As(V), as reference compounds showing various oxidation states of As. The XANES spectrum of As(III) had an absorption edge at 11,869.0 eV [35] while that of As(V) was at 11,872.8 eV [6] which was similar to the absorption edge of the spent K-OMS powder. It, therefore, suggested that partial As(V) was possibly adsorbed on the spent K-OMS2 surface after As(III) oxidation leading to a loss in some active sites of K-OMS2 surface, consequently, the decrease of oxidation efficiency in the working column and the reuse cycle number.

3.2 Arsenite Oxidation over K-OMS2 (coated) in Single Continuous Fixed-Bed Column

Breakthrough curves of As(III) oxidation by K-OMS2 (coated) in single continuous fixed-bed column under different experimental conditions: I (bed length = 10 cm, flow rate = 10 mL/min), II (bed length = 15 cm, flow rate = 5 mL/min), and III (bed length = 20 cm, flow rate = 5 mL/min) are shown in Figure 4. They also present the breakthrough curves of total As and calculated As(V) using the equation $[As_{total}] = [As(III)] + [As(V)]$. It was found that As(III) concentration in the effluent for all three experimental conditions had slightly released during the first 120 min with fluctuation, and then been quite stable until 600 min. Moreover, the As(III) concentration of the experimental condition I was higher than that of the experimental

conditions II and III. The almost similar breakthrough of As(III) in the experimental conditions II and III meant to the undifferentiated oxidizing ability to transform As(III) to As(V) for 600 min. However, the calculated highest oxidation percentage of the experimental conditions I, II, and III were 88.51, 130.40, and 114.91% at 60, 120, and 200 min, respectively. The percentages of more than 100% may be caused by adsorption of the oxidized As(III) on the K-OMS2 (coated) as described in the former report [16] and found in the XANES results in this study. After that, the oxidized As(III) was released during 120 and 200 min of experimental conditions II and III, respectively. Therefore, the mechanism that happens on the K-OMS2 (coated) surface would be oxidation-adsorption. The experimental condition II was also chosen as the most optimal condition for further study as it required the shorter bed-length concerning the amount of the K-OMS2.

Although the oxidation-adsorption process was occurring in the K-OMS2 (coated) surface, the oxidation route was still the major mechanism of K-OMS2. Thus, the K-OMS2 (coated) was mainly considered as the oxidizing agent which be able to reuse several times. As(III) oxidation by the three-round-use cycle of K-OMS2 (coated) in the continuous fixed-bed column under experimental condition II is presented in Figure 5. The appearance of the fresh and spent columns is shown in Figure 5(a) along with their C/C_0 versus time plots in Figure 5(b). After the 600 min of three-round-use, the partial surface of the K-OMS2 (coated) in the column was uncovered the white surface of the ceramic balls due to the peel-off K-OMS2, but the three-round As(III) oxidation efficiency slightly decreased according to the number of cycles but could be much undifferentiated. Therefore, it leads to conclude that the K-OMS2 (coated) column can be used repeatedly while maintaining the good and stable oxidizing efficiency of As (III) throughout the test runs.

The Mn and K leaching during the three-round As(III) oxidation over K-OMS2 (coated) in the continuous fixed-bed column under experimental condition II were also

investigated. The results are presented in Figure 5(c)-(d). The Mn concentrations were in a range of 0.01-0.07 mg/L for the 1st round, 0.00-0.02 mg/L for the 2nd round, and 0.00-0.03 mg/L for the 3rd round. The Mn leaching concentration from the 2nd and the 3rd round was likely consistent and lower than the one from the 1st round. The Mn leaching concentration was also lower than the WHO drinking water standard which is set at below 0.1 mg/L [36]. For the K leaching, its concentration was quite high for the 1st round especially during the first 110 min with a range of 0.55-5.42 mg/L. The K leaching concentration was then low and stable even if in the 2nd and the 3rd round of use the K-OMS2 (coated) column. The high concentration of K leaching was probably due to the position of K in the K-OMS2 chemical structure. K is in the cavity with a weak bond compared to the Mn exists by the covalent bond between Mn and O which is stronger [37]. However, K is not considered necessary to establish a health-based guideline value for potassium in drinking water recommended by WHO [36].

3.3 Arsenate Adsorption over Fe-BTC (coated) in Single Continuous Fixed-Bed Column

The breakthrough curves of As(V) adsorption by Fe-BTC (coated) in the continuous fixed-bed column under experimental conditions: I (bed length = 10 cm, flow rate = 10 mL/min), II (bed length = 15 cm, flow rate = 5 mL/min), and III (bed length = 20 cm, flow rate = 5 mL/min) are shown in Figure 6. The experimental condition I gave the breakthrough curve with a steeper slope than the experimental conditions II and III. In Figure 6(b)-(d), the Fe-BTC (coated) column was able to adsorb As(V) and control the effluent concentration to lower than 0.01 mg/L which is the As concentration limit in drinking water standards by WHO [8]. The breakthrough capacity was found at 1.16, 0.31, and 0.28 mg/g within the first 40, 30, and 40 min for the experimental conditions I, II, and III, respectively.

The Thomas model and Yoon-Nelson model were used to explicate the kinetic adsorption and estimate breakthrough curves in the column. The obtained equation from the

suitable model can be used further for illustrating the fixed-bed column behavior and scaling up the treatment system for industrial applications [26]. The calculation results obtained from applying the linear equation of the Thomas model and the Yoon-Nelson model present in Table 2. It was found that the standard deviation (S.D.) obtained from the Yoon-Nelson model was lower than the ones from the Thomas model for all experimental conditions. The Yoon-Nelson model was thus appropriately used for adsorption behavior explanation as well as a simulation in the case of the Fe-BTC (coated) column in this study, which determined that the rate of adsorption decreases relies on the proportional of adsorbate breakthrough on the adsorbents [26, 38]. Moreover, for both models, the experimental condition I gave the highest square of the correlation (R^2) of 0.9206, but the highest maximum adsorption capacity (q_0) was under the experimental condition II. Therefore, the As(V) adsorption over the Fe-BTC (coated) under experimental condition II relying on the Yoon-Nelson model was used further for Fe leaching study and the combined continuous fixed-bed columns study.

In Figure 7, Fe leaching study from one-round-use of Fe-BTC (coated) column was in the range of 0.0.7–0.20 mg/L although there is no guideline value from WHO for iron in drinking water as the Fe is one of the most abundant metals in Earth's crust and found in natural freshwaters at a range of 0.5-50 mg/L [36].

3.4 Total Arsenic Removal over K-OMS2 (coated) and Fe-BTC (coated) in Combined Continuous Fixed-Bed Columns

The breakthrough curves of total As removal over K-OMS2 (coated) and Fe-BTC (coated) in combined continuous fixed-bed columns under the experimental conditions II are presented in Figure 8(a). It was found in the first column of K-OMS2 (coated) enabled to decrease the concentration of As(III) and was relatively stable after 120 min. The oxidizing ability of the K-OMS2 (coated) to transform As(III) to As(V) corresponded in the first 600 min

corresponded to the results from the single continuous fixed-bed column a single column study of K-OMS2 (coated) under experimental condition II reported in the previous section in this study. After 120 min of the K-OMS2 (coated) test run with more than 95% of As(III) being oxidized, the second column of Fe-BTC (coated) was immediately connected with the K-OMS2 (coated) column. Then, the Fe-BTC (coated) column served the As(V) released from the first column and treat the As(V) via the adsorption process. The total As in the effluent from the second column was monitored as a representation of the entire As treatment working system. The total As slowly broke through from the second column and maintained higher than 60% of As treatment throughout 2,200 min of the test run. As a result, here is a high possibility to combine K-OMS2 (coated) and Fe-BTC (coated) continuous fixed-bed columns for As(III) removal and can investigate further in a future study.

The Mn and K leaching from the first K-OMS2 (coated) column and the Mn, K, and Fe leaching from the second Fe-BTC (coated) column existed in the effluent were repeatedly monitored, as shown in Figure 8(b)-(c). The Mn was slightly leached from the first column, while the K leaching was unfound. Besides, The K was leached from the second column in the only first 40 min for 0.06–1.76 mg/L before undetected while the Mn concentration was undifferentiated from the effluent in the first K-OMS2(coated) column. Also, the Fe was slightly dissolved and leached since Fe binds to BTC with a strong covalent bond in the structure [39].

4. Conclusions

To enhance the performance of total arsenic removal, a combination of oxidation and adsorption processes were proposed. The K-OMS2 (coated) was used for oxidation of As(III) to As(V), while the transformed As(V) was adsorbed on the Fe-BTC (coated). In the part of the continuous fixed-bed column study, the K-OMS2 (coated) column showed that the

operating maintained stable after 120 min and highly oxidize As(III) to As(V) during 600 min of the test run. Moreover, the XANES results revealed that the partial As(V) can be adsorbed on the K-OMS2 surface which may cause the loss of its active sites. Also, the K-OMS2 (coated) column can be used at least for three rounds, in which oxidizing capacity is slightly decreased according to the number of cycles with very low Mn and K leaching. In the instance of the Fe-BTC column, As(V) was highly adsorbed by Fe-BTC (coated), and Fe leaching was quite low. The experimental data fitted well with Yoon-Nelson Model with a maximum adsorption capacity of 52.60 mg/g (R^2 = 0.8704 and S.D. = 6.22). With the K-OMS2 (coated) and Fe-BTC (coated) continuous fixed-bed columns combined under the optimal experimental conditions, the total As(III) was removed for more than 60% throughout 2,200 min of the test run. The coating technique of K-OMS2 and Fe-BTC in this study was concluded to have the potential to practically apply in an upscaled As treatment approach.

Acknowledgments

This work was financially supported by The Thailand Research Fund (MRG6180196), Office of the Higher Education Commission, the Research and Technology transfer affairs of Khon Kaen University, Center of Excellence on Hazardous Substance Management (HSM), Chulal ongkorn University, and Chronic Kidney Disease Prevention in The Northeast of Thailand (C KDNET), Faculty of Medicine, Khon Kaen University, Thailand.

References

[1] S. Kong, Y. Wang, H. Zhan, S. Yuan, M. Yu, M. Liu, Adsorption/Oxidation of Arsenic in Groundwater by Nanoscale Fe-Mn Binary Oxides Loaded on Zeolite, Water Environ Res. 86 (2014) 147–55.

[2] K.S. Mohammed Abdul, S.S. Jayasinghe, E.P.S. Chandana, C. Jayasumana , P.M.C.S. De

Silva, Arsenic and human health effects: A review, Environ Toxicol Pharmacol. 40 (2015) 828–46.

[3] L. Zheng, C.C. Kuo, J. Fadrowski , J. Agnew, V.M. Weaver, A. Navas-Acien, Arsenic and Chronic Kidney Disease: A Systematic Review, Curr Environ Heal Reports. 1 (2014) 192–207.

[4] C. Jain , I. Ali, Arsenic: occurrence, toxicity and speciation techniques, Water Res. 34 (2000) 4304–4312.

[5] J.Y. Chung, S.D. Yu, Y.S. Hong, Environmental source of arsenic exposure, J. Prev. Med. Public Heal. 47 (2014) 253–257.

[6] S.C. Ying, B.D. Kocar, S. Fendorf, Oxidation and competitive retention of arsenic between iron- and manganese oxides, Geochim. Cosmochim. Acta. 96 (2012) 294–303.

[7] V.K. Sharma, M. Sohn, Aquatic arsenic: Toxicity, speciation, transformations, and remediation, Environ. Int. 35 (2009) 743–759.

[8] K. Mar Wai, M. Umezaki , O. Mar, M. Umemura , C. Watanabe, Arsenic exposure through drinking Water and oxidative stress Status: A cross-sectional study in the Ayeyarwady region, Myanmar, J. Trace Elem. Med. Biol. 54 (2019) 103–109.

[9] S. Ghosh (Nath), A. Debsarkar, A. Dutta, Technology alternatives for decontamination of arsenic-rich groundwater—A critical review, Environ. Technol. Innov. 13 (2019) 277–303.

[10] Y. Wei, H. Liu, C. Liu, S. Luo, Y. Liu, X. Yu, J. Ma, K. Yin, H. Feng, Fast and efficient removal of As(III) from water by $CuFe_2O_4$ with peroxymonosulfate: Effects of oxidation and adsorption, Water Res. 150 (2019) 182–90.

[11] N. Nicomel, K. Leus, K. Folens, P. Van Der Voort, G. Du Laing, Technologies for Arsenic Removal from Water: Current Status and Future Perspectives, Int. J. Environ. Res. Public Health. 13 (2015) 1–24.

[12] R. Singh, S. Singh, P. Parihar, V.P. Singh, S.M. Prasad, Arsenic contamination, consequences and remediation techniques: A review, Ecotoxicol. Environ. Saf. 112 (2015) 247–270.

[13] Y. Xi, J. Zou, Y. Luo, J. Li, X. Li, T. Liao, L. Zhang, C. Wang, G. Lin, Performance and mechanism of arsenic removal in waste acid by combination of $CuSO_4$ and zero-valent iron, Chem. Eng. J. 375 (2019) 121928.

[14] Y. Li, X. Zhu, X. Qi, B. Shu, X. Zhang, K. Li, Y. Wei, H. Wang, Removal and immobilization of arsenic from copper smelting wastewater using copper slag by in situ encapsulation with silica gel, Chem. Eng. J. 394 (2020) 124833.

[15] S. Lata, S.R. Samadder, Removal of arsenic from water using nano adsorbents and challenges: A review. J. Environ. Manage. 166 (2016) 387–406.

[16] J. Phanthasri, P. Khamdahsag, P. Jutaporn, K. Sorachoti, K. Wantala, V. Tanboonchuy, Enhancement of arsenite removal using manganese oxide coupled with iron (III) trimesic, Appl. Surf. Sci. 427(2018) 545–552.

[17] S. Dharmarathna, C.K. King'ondu, L. Pahalagedara, C.H. Kuo, Y. Zhang, S.L. Suib, Manganese octahedral molecular sieve (OMS-2) catalysts for selective aerobic oxidation of thiols to disulfides, Appl. Catal. B. 147 (2014) 124–131.

[18] Y.F. Shen, R.P. Zerger, R.N. DeGuzman, S.L. Suib, L. McCurdy, D.I. Potter, C. L. O'Young, Manganese Oxide Octahedral Molecular Sieves: Preparation , Characterization , and Applications, Science. 260 (1993) 511–515.

[19] A. Yodsa-nga, J.M. Millanar, A. Neramittagapong, P. Khemthong, K. Wantala, Effect of manganese oxidative species in as-synthesized K-OMS 2 on the oxidation of benzene, Surf. Coat. Technol. 271 (2015) 217–224.

[20] Y. Lv, X. Tan, F. Svec, Preparation and applications of monolithic structures containing metal–organic frameworks, J. Sep. Sci. 40 (2017) 272–87.

[21] T.A. Vu, G.H. Le, C.D. Dao, L.Q. Dang, K.T. Nguyen, Q.K. Nguyen, P.T. Dang, H.T.K. Tran, Q.T. Duong, T.V. Nguyen, G.D. Lee, Arsenic removal from aqueous solutions by adsorption using novel MIL-53(Fe) as a highly efficient adsorbent, RSC Adv. 5 (2015) 5261–5268.

[22] J. Zhu, X.Y. Yu , Y. Jia, F.M. Peng, B. Sun, M.Y. Zhang , T. Luo, J.H. Liu, X.J. Huang, Iron and 1,3,5-Benzenetricarboxylic Metal−Organic Coordination Polymers Prepared by Solvothermal Method and Their Application in Efficient As(V) Removal from Aqueous Solutions, J. Phys. Chem. C. 116 (2012) 8601–8607.

[23] N. Supannafai, J. Phanthasri, P. Tanboonchuy, V. Assawadithalerd, M. Khamdahsag, Surface study of manganese oxides and iron-based metal-organic frameworks coated on ceramic balls., in: 56th Kasetsart Univ. Annu. Conf. Bangkok, Thail., 2 (2018) 17-24.

[24] N. Supannafai, J. Phanthasri, P. Tanboonchuy, V. Assawadithalerd, M. Khamdahsag, Surface charge effects of manganese oxide octahedral molecular sieve-coated ceramic balls on arsenite oxidation, in: 2nd Int. Conf. Bioresour. Energy, Environ. Mater. Technol. Gangwon Prov. Korea, Gangwon, Korea, PP01 (2018) 128.

[25] N. Supannafai, J. Phanthasri, P. Tanboonchuy, V. Assawadithalerd, M. Khamdahsag, Elemental distribution analysis of manganese oxide and iron-based metal organic framework using micro-XRF technique, in: 11th Srinakharinwirot Univ. Res. Conf. Bangkok, Thail., Bangkok, (2018) 957–964.

[26] M.T. Yagub, T.K. Sen, S. Afroze, H.M. Ang, Fixed-bed dynamic column adsorption study of methylene blue (MB) onto pine cone, Desalin. Water Treat. 55 (2015) 1026–1039.

[27] L. Feng, Z. Xuan, H. Zhao, Y. Bai, J. Guo, C.W. Su, X. Chen, MnO_2 prepared by hydrothermal method and electrochemical performance as anode for lithium-ion battery, Nanoscale Res. Lett. 9 (2014) 1–8.

[28] H.F. Garces, J. Roller, C.K. King'ondu, S. Dharmarathna, R.A. Ristau, R. Jain, R. Maric, S.L. Suib, Formation of Platinum (Pt) Nanocluster Coatings on K-OMS-2 Manganese Oxide Membranes by Reactive Spray Deposition Technique (RSDT) for Extended Stability during CO Oxidation, Adv. Chem. Eng. Sci. 4 (2014) 23–35.

[29] M. Wei, Y. Ruan, S. Luo, X. Li, A. Xu, P. Zhang, The facile synthesis of a magnetic OMS-2 catalyst for decomposition of organic dyes in aqueous solution with peroxymonosulfate, New J. Chem. 39 (2015) 6395–6403.

[30] M.H. Wu, J. Shi, H.P. Deng, Metal doped manganese oxide octahedral molecular sieve catalysts for degradation of diclofenac in the presence of peroxymonosulfate. Arab. J. Chem. 11 (2018) 924-934.

[31] J.M. Millanar, A. Yodsa-Nga, M.D.D. Luna, K.Wantala, Thermal catalytic oxidation of toluene by K-OMS 2 synthesized via novel uncalcined route., in: Int. Conf. Biol. Civ. Environ. Eng., (2014) 29–31.

[32] X. Chen, Y.F. Shen, S.L. Suib, C.L. O'Young, Characterization of manganese oxide octahedral molecular sieve (M-OMS-2) materials with different metal cation dopants, Chem Mater. 14 (2002) 940–948.

[33] T. Araya, C.C. Chen, M.K. Jia, D. Johnson, R. Li, Y.P. Huang, Selective degradation of organic dyes by a resin modified Fe-based metal-organic framework under visible light irradiation, Opt. Mater. (Amst). 64 (2017) 512–523.

[34] E.R. García, R.L. Medina , M.M. Lozano, I.V. Pérez, Valero MJ, Maubert Franco AM. Adsorption of azo-dye Orange II from aqueous solutions using a metal-organic framework material: Iron- benzenetricarboxylate. Materials (Basel). 7 (2014) 8037–8057.

[35] M. Chen, Y. Yang, W. Liu, C. Wang, B. Johannessen, An in-situ synchrotron XAS study on the evolution of aqueous arsenic species in acid pressure leaching, Hydrometallurgy.

175 (2018) 11–19.

[36] World Health Organization. Guidelines for drinking-water quality: fourth edition incorporating the first addendum. 4th ed. 2017.

[37] T. Sriskandakumar, N. Opembe, C.H. Chen, A. Morey, C. King'Ondu, S.L. Suib, Green decomposition of organic dyes using octahedral molecular sieve manganese oxide catalysts, J. Phys. Chem. A. 113 (2009) 1523–1530.

[38] P. Luekittisup, V.Tanboonchauy, J. Chumee, S. Predapitakkun, R.W. Kiatkomol, N. Grisdanurak, Removal of chlorinated chemicals in H_2 feedstock using modified activated carbon, J. Chem. (2015) 1-9.

[39] S. Shahid, K. Nijmeijer, High pressure gas separation performance of mixed-matrix polymer membranes containing mesoporous Fe(BTC), J. Memb. Sci. 459 (2014) 33–44.

List of Tables

Table 1.

Experimental conditions of arsenite oxidation over K-OMS2 (coated) in a single continuous fixed-bed column and arsenate adsorption over Fe-BTC (coated) in a single continuous fixed-bed column

Condition	K-OMS2 (coated) column			Fe-BTC (coated) column		
	I	II	III	I	II	III
Flow rate (mL/min)	10	5	5	10	5	5
Bed length (cm)	10	15	20	10	15	20
Coated ball weight (g)	45.50	72.32	94.95	46.96	72.84	97.21
% coating	1.29	0.98	0.97	0.86	0.79	0.86
Powder weight (g)	0.59	0.71	0.92	0.40	0.57	0.84
Residence time-calculated (min)	3.14	9.43	12.57	3.14	9.43	12.57
Residence time-measured (min)	1.90	4.50	5.75	2.93	4.33	5.43
Initial pH	7.0	7.0	7.0	6.0	6.0	6.0

Table 2

Rate constants and As(V) adsorbed by Fe-BTC (coated) obtained from Thomas model and Yoon-Nelson model

Experimental condition	Thomas model				Yoon-Nelson model				
	K_T (mL/min /mg)	q_0 (mg/g)	S.D. (%)	R^2	K_{YN} (1/min)	τ (min)	q_0 (mg/g)	S.D. (%)	R^2
I	0.0051	11.97	13.66	0.92	0.0063	393.46	11.40	1.61	0.92
II	0.0003	60.12	30.67	0.87	0.0004	5,081.25	52.60	6.22	0.87
III	0.0003	49.01	13.66	0.80	0.0004	6,185.75	42.89	1.60	0.80

List of Figure

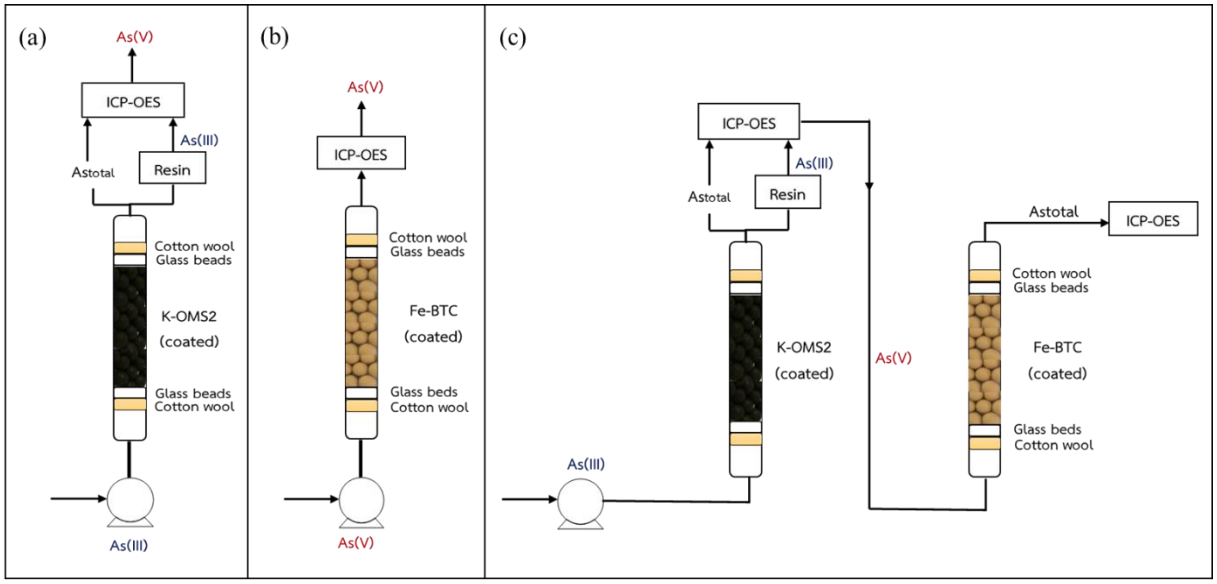

Fig .1. Continuous fixed-bed columns configuration**: (**a**)** K-OMS2 **(**coated**)** packed in a single column for As**(**III**)** oxidation, **(**b**)** Fe-BTC **(**coated**)** packed in a single column for As**(**V**)** adsorption, and **(**c**)** combined columns of K-OMS2 **(**coated**)** and Fe-BTC **(**coated**)**

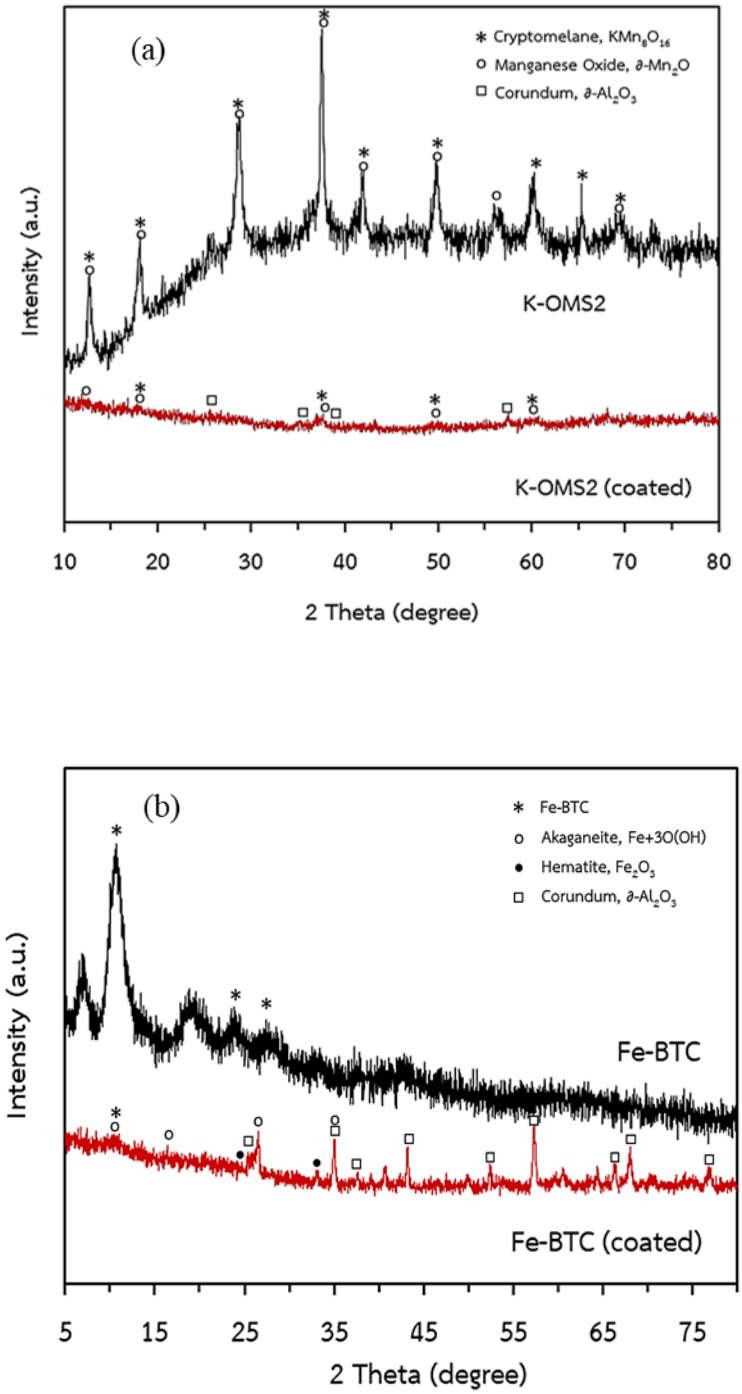

Fig. 2. XRD patterns of (a) K-OMS2 powder compared to K-OMS2 (coated) and (b) Fe-BTC powder compared to Fe-BTC (coated)

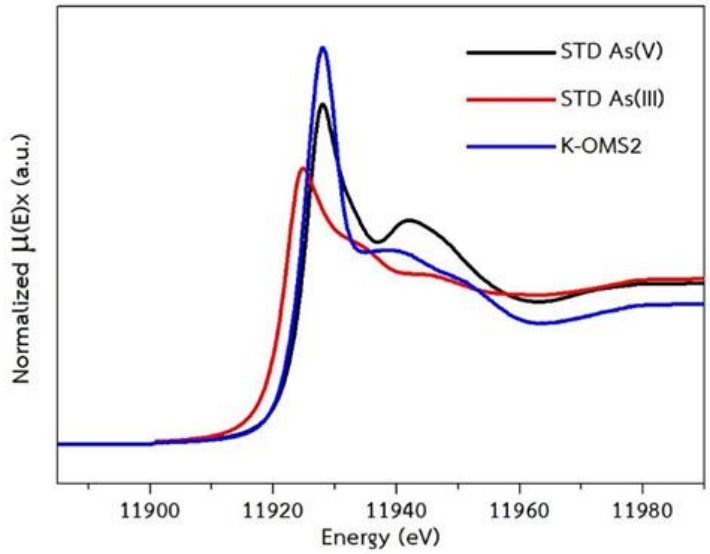

Fig. 3. K-edge XANES spectra of spent K-OMS2 compare to As(III) and As(V) standards

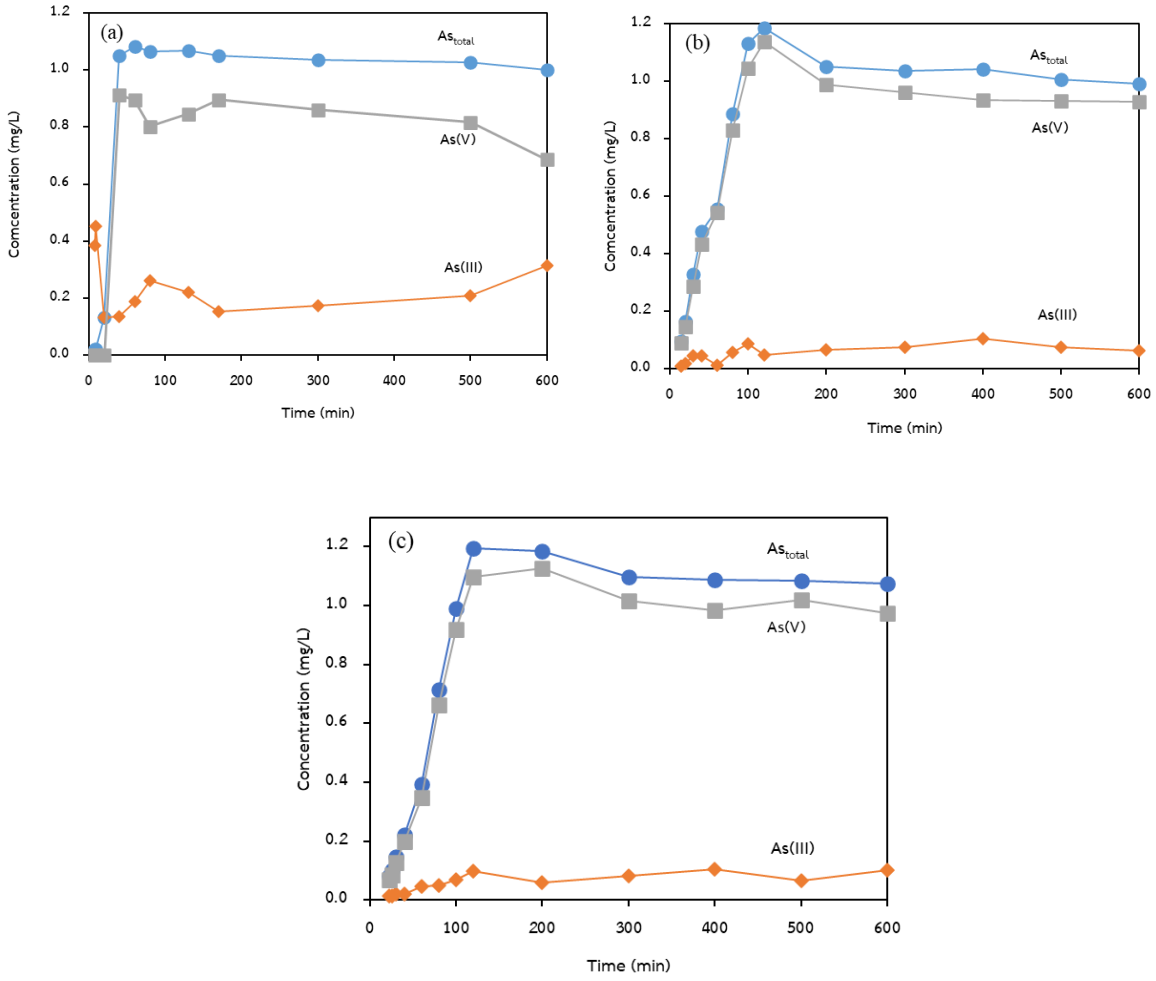

Fig. 4. Breakthrough curve of As(III) oxidation by K-OMS2 (coated) in different experimental conditions: (a) I (bed length = 10 cm, flow rate = 10 mL/min), (b) II (bed length = 15 cm, flow rate = 5 mL/min), and (c) III (bed length = 20 cm, flow rate = 5 mL/min)

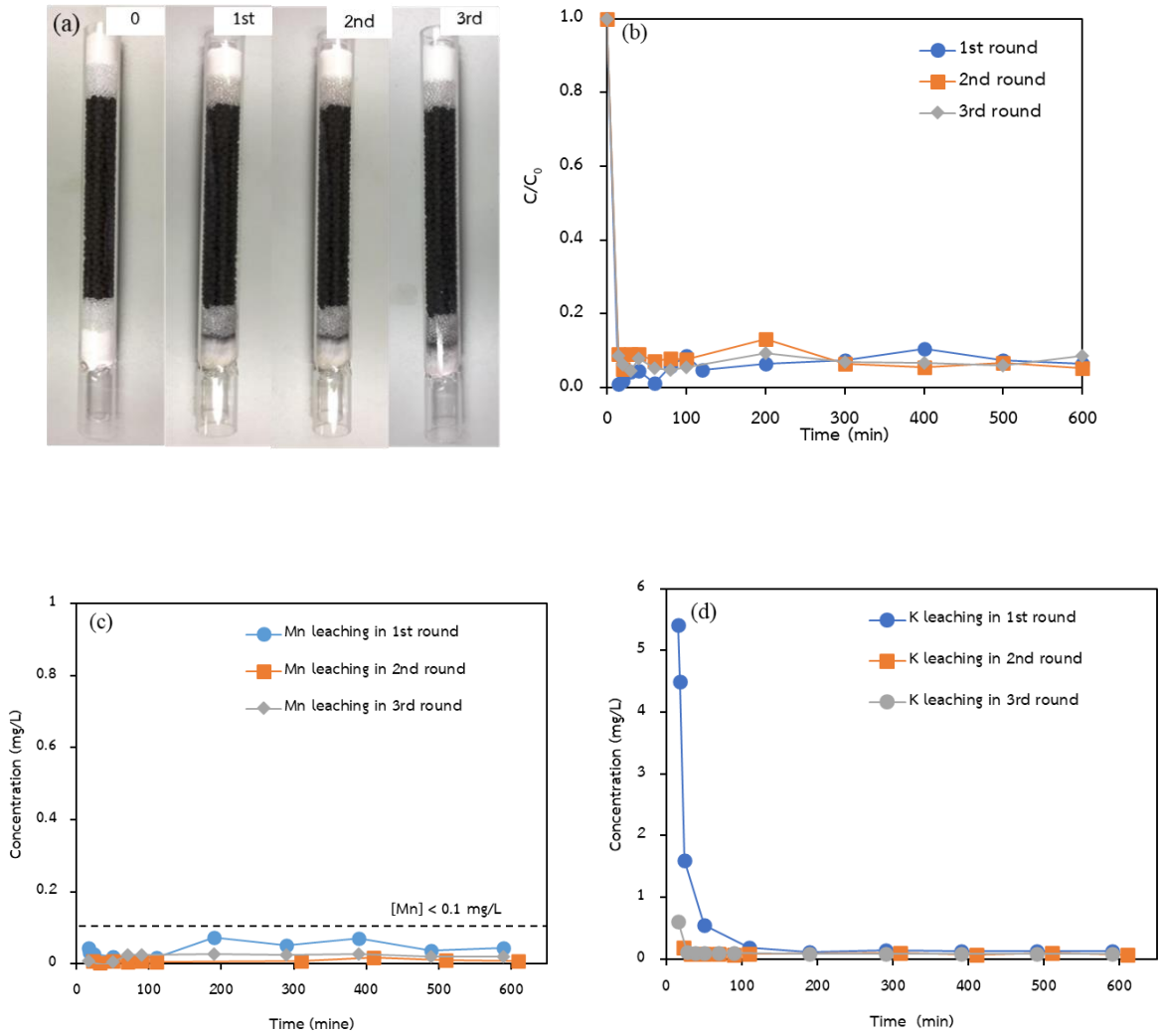

Fig. 5. As(III) oxidation by 3-round-use of K-OMS2 (coated) in the continuous fixed-bed column under experimental condition II: (a) appearance of the fresh and spent columns, (b) their C/C_0 curves, (c) Mn leaching, and (d) K leaching

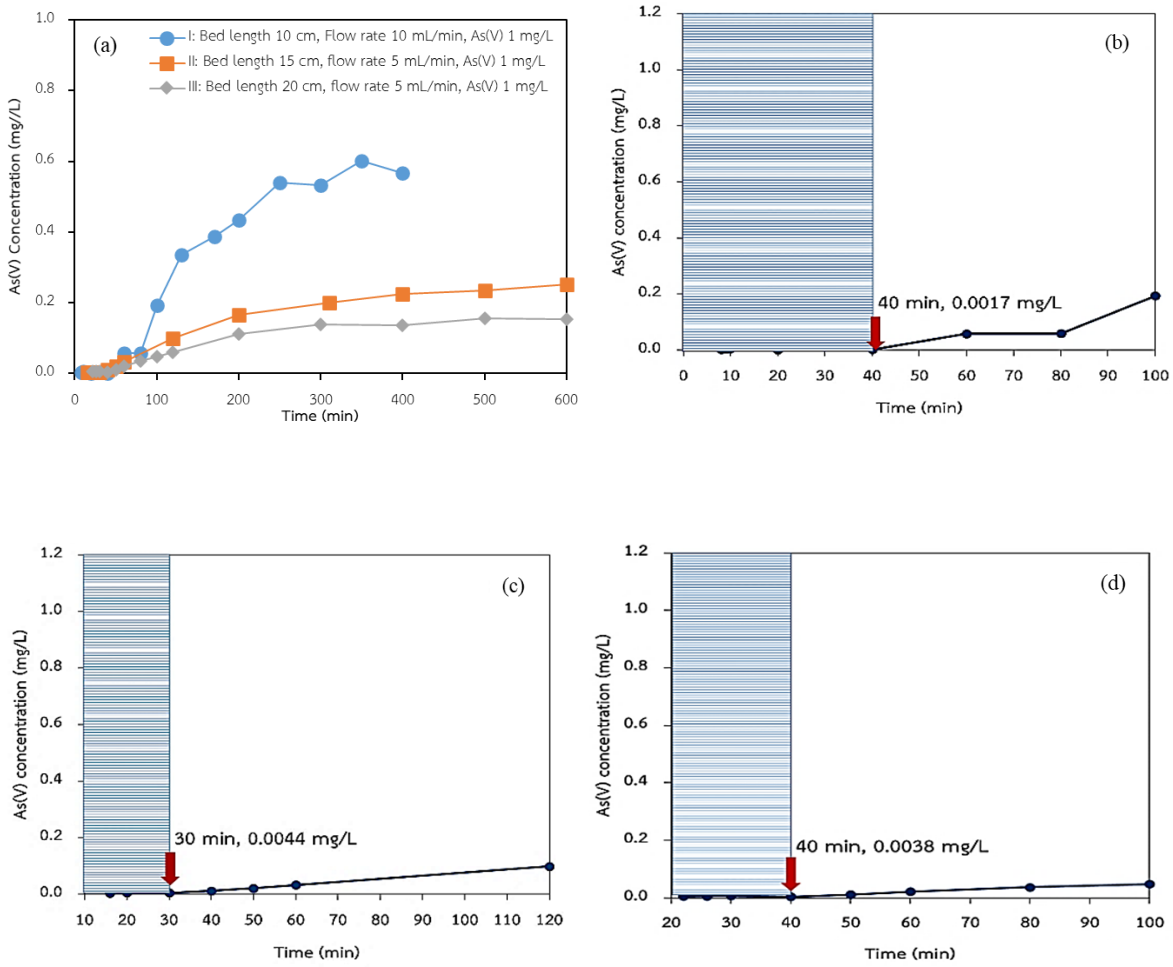

Fig. 6. As(V) adsorption by Fe-BTC (coated) in the continuous fixed-bed column (a) breakthrough curve, and breakthrough capacity under experimental conditions: (b) I (bed length = 10 cm, flow rate = 10 mL/min), (c) II (bed length = 15 cm, flow rate = 5 mL/min), and (d) III (bed length = 20 cm, flow rate = 5 mL/min)

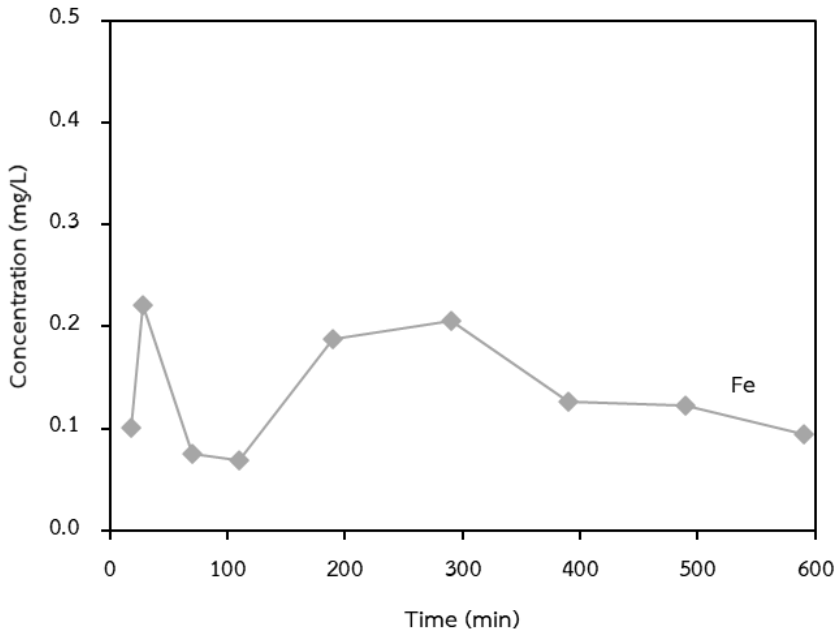

Fig 7. Fe leaching over As(V) adsorption by Fe-BTC (coated) in the continuous fixed-bed column under experimental condition II

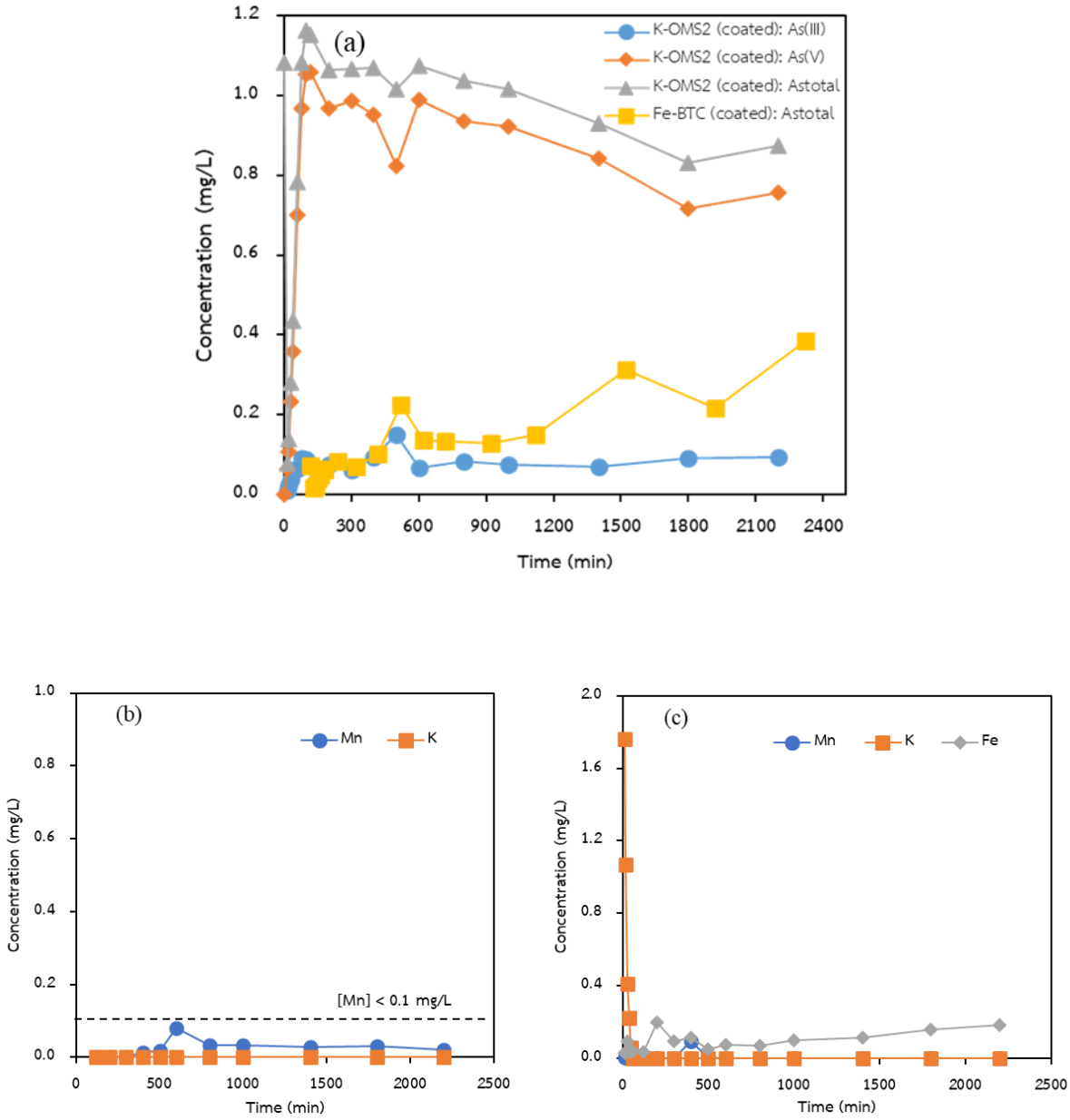

Fig. 8. Total As removal over K-OMS2 (coated) and Fe-BTC (coated) in combined continuous fixed-bed columns: (a) breakthrough curve, (b) Mn and K leaching from K-OMS2 (coated) column, and (c) Mn, K, and Fe leaching from Fe-BTC (coated) column

Declaration of interests

☒ The authors declare that they have no known competing financial interests or personal relationships that could have appeared to influence the work reported in this paper.

☐The authors declare the following financial interests/personal relationships which may be considered as potential competing interests:

嘉南藥理大學
Chia Nan University of Pharmacy & Science

17 August 2018

Prof. Visanu Tanboonchuy
Department of Environmental Engineering
Khon Kaen University

2018 International Conference on Information Technology and Applied Sciences
22 October 2018, The Chia Nan University of Pharmacy and Science

Dear Prof. Tanboonchuy,

Further to the pervious emails between Dr. Hsiaoting Chiu, I would like to express our heartfelt gratitude to you for being our keynote speaker of the 2018 International Conference on Information Technology and Applied Sciences to be held on 22 October 2018 in Tainan, Taiwan. The conference is hosted by College of Humanities and Applied Information, The Chia Nan University.

As our keynote speaker, the passage, accommodation and honorarium for the conference will be provided for you as a token of appreciation. We are confident that the conference will be successful with your support and participation. We look forward to seeing you in Taiwan.

Should you need further information or arrangement, please feel free to contact Dr. Chiu.(Tel: 886-62664911 ext.5002, e-mail: htchiu@mail.cnu.edu.tw)

Yours sincerely,

Zhi-Yuan Su

Prof. Zhi-Yuan Su
Professor and Dean
College of Humanities and Applied Information
Chia Nan University of Pharmacy and Science